Amutha Ramachandran

Surface studies of palladium based membranes and model systems

Thesis for the degree of Philosophiae Doctor

Trondheim, April 2009

Norwegian University of Science and Technology
Faculty of Natural Sciences and Technology
Department of Physics

NTNU
Norwegian University of
Science and Technology

NTNU
Norwegian University of Science and Technology

Thesis for the degree of Philosophiae Doctor

Faculty of Natural Sciences and Technology
Department of Physics

ISBN 978-82-471-1504-6 (printed ver.)
ISBN 978-82-471-1505-3 (electronic ver.)
ISSN 1503-8181

Doctoral theses at NTNU, 2009:64

Printed by NTNU-trykk

Abstract

The work of this thesis can be divided in to parts, one is based on the Pd/Ag alloy membranes and the other is about the model systems. It is well known that, Pd is a potential candidate membrane material, due to both its high solubility and permeability to hydrogen. Alloying of Pd with 23wt% Ag has been found to be an optimum composition for high hydrogen permeability.

Thin Pd/Ag 23wt% free standing films of thicknesses in the range 1.3 -10 µm were prepared by magnetron sputtering. The influence of thermal treatments in different gases on the hydrogen permeation behaviour of the selected membranes and the surface properties were investigated through a combination of hydrogen flow measurements and surface characterization. After thermal treatment in air at 300˚C, we observed enhanced hydrogen permeation for ~1.3 to 5 µm membranes. Topography studies by atomic force microscopy showed that the increase in permeance correlated with increase in surface roughness and surface area. A similar behaviour in improvement of hydrogen flux was observed for an alternative treatment namely heat treatment in N_2/Ar at 400˚C for 1.5 µm membranes. The topography investigations showed increase in surface roughness and area also after this treatment.

To shed more light on the effect of the N_2/Ar thermal treatments, we performed thermal treatments in this presumed inert atmosphere at three different temperatures (300˚C, 400˚C and 450˚C) for three different film thicknesses, 2 µm, 5µm and 10 µm. For comparison we performed thermal treatment in air at 300˚C for all selected films. After all treatments the hydrogen flux was found to be increase compared to before treatment for the 2 µm membranes, more strongly for the higher temperatures. In contrast for the thicker films the flux was decreasing after the treatments except for the 5 µm membranes thermally treated in N_2/Ar at 450˚C. On the other hand improvement in flux was obtained for all samples after air treatment at 300˚C. Increase in surface roughness and surface area were accompanying the increased flux for the 2 µm membranes. No significant changes in surface roughness, at the initially rougher membrane surface, were observed for the membranes with decreasing flux. Summarizing all results from our group indicates bulk limited hydrogen permeation for the membranes of thickness down to 1.5-2 µm thermally treated in air at 300˚C. Chemical composition analysis revealed Ag segregation to the surface for all N_2/Ar thermal treated membranes and reverse segregation behaviour for air-treated on 1.5 µm and 5 µm membranes.

Long term stability of a 2.6 µm Pd-23%Ag/stainless steel composite membrane was examined in H_2/N_2 mixture as a function of both temperature and feed pressure. During continuous operation, the membrane showed good stability at 400°C while the N_2 leakage increased very slowly at a temperature of 450°C (P_{feed} = 10bar). After 100 days of operation (P_{feed} = 5-20bar, T=350-450°C), the N_2 permeance was 7.0×10^{-9} mol $m^{-2}s^{-1}Pa^{-1}$, which indicates that the H_2/N_2 permselectivity still lies around 500.Surface topography observed by atomic force microscopy (AFM) showed small changes in surface area after the long term stability measurements. Possible surface defects were

also detected. In addition, segregation of Ag to the membrane surfaces was found from X-ray photoelectron spectroscopy (XPS) and Auger electron spectroscopy (AES).

To address specific issues related to Pd based membrane systems, two selected Pd based model systems were studies as part of this thesis work. Molecular adsorption of methanol and its decomposition pathway on clean Pd(110) and an alloy Ag/Pd(110) surface were investigated. Multilayer methanol molecules adsorption on the surface was found at 100K. The methanol behaviour of these two surfaces was quite similar. Upon heating to 170K, two methanol species were identified. CO was formed on the surfaces at 250K and was desorbed at 500K. These studies show that silver at the amount deposited in the present work does not influence the methanol decomposition as compared to clean Pd(110).

As a model system for addressing interactions of adsorbed organonitrogen compounds on Pd(110) we have studied the methylamine molecular adsorption behaviour on this surface. Decomposition of adsorbed CH_3NH_2 to CN occurs mainly in the temperature range from 300 K to 350 K. The intermediate species CN remained at the surface even after annealing to 800K. Density function theory shows that methylamine is found to bind to Pd(110) surface via a lone pair state on the N atom.

Preface

This thesis is submitted in partial fulfillment of the requirements for the doctoral degree at the Norwegian University of Science and Technology (NTNU). It is the result of scientific work carried out over more than four years period from September 2004 to February 2009. This work is a subproject of 'Materials for Hydrogen Technology', a FUNMAT project on the activity Hydrogen B1: Membrane surface characterization. This project has been financed by the Research council of Norway. During this time I have taken the equivalent of half a year of courses.

The experimental works presented in the thesis are mainly two parts. One of the works is based on the hydrogen permeation measurements of PdAg membranes followed by the surface characterization. The permeation results included in the thesis have been performed in Department of Chemical Engineering, NTNU, Trondheim. Also I spent couple of weeks at SINTEF Materials and Chemistry for the experimental work on hydrogen permeation measurements. The experimental investigations on surface topography analysis were conducted in the AFM lab, SINTEF, Trondheim. The experimental works for the compositional analysis were carried out in the XPS laboratory, Oslo. The other work is mainly based on the Pd(110) model systems. The photoelectron spectroscopy measurements for the model systems have been performed in the Department of Synchrotron Radiation Research at MAX-lab, Lund University, Sweden.

Over this research period, I have also participated in several FUNMAT project meetings and given a few oral presentations. In 2006 I gave an oral presentation in the 9^{th} international conference on inorganic membranes, Lillehammer, Norway. In 2007, I have participated in NANOMAT international conference and satellite meetings with two poster presentations in addition to an oral presentation in Bergen, Norway. My participation also includes in the 10^{th} international conference on inorganic membranes, Tokyo, Japan with an oral presentation. In addition, I took part in a ten days course on membrane characterization, NANOMEM 2007, Zaragoza, Spain. In addition, I have attended a student conference conducted by Statoil Hydro in 2007. The conferences and the meetings had been very useful in keeping me updated in my research field.

Trondheim, March 2009

A. Ramachandran

Acknowledgements

This is a great opportunity to express the gratitude to my supervisor Prof. Anne Borg**,** for giving me the opportunity to pursue my PhD under her supervision and introducing me to Surface Physics. I am very grateful to her, who not only led as my supervisor but also encouraged, challenged and guided me with never-ending optimism throughout the academic program. I will never forget her great help in the very beginning days of my first abroad life in Norway. I would also like to thank her family for the kind welcome during my first days. It was great help for giving me the time for the discussions when I needed it in her busy schedule.

Next I would like to convey my special thanks and respects to Prof. Ola Hunderi for his kind encouragements during initial days. Also I express my thanks to Dr. Rune Bredesen, my co-supervisor for his valuable suggestions in the project. My special thanks go to Associate Professor Hilde J.Venvik, who always had a vital role in educating and alerting me with her valuable and constructive comments in the paper work.

I have to say many thanks to Dr. Trine Andersen for helping me in all aspects to learn the laboratory equipments and the analysis softwares. I can not forget the time that I spent in MAX-lab with Trine, Ingeborg, Lars Erik and Anne. Especially the experiments in September 2007 were so exciting and we had even celebration cakes with hope to get good results and that really worked out. Apart from being colleagues, Lund was the right place to find their friendliness. I am pleased to thank A.L. Mejdell being a friend in my work as well as in life. I have to thank W.M. Tucho and Yun Liu for several coffee meetings. I thank J. Walmsley, SINTEF, Trondheim for his help in doing the AES measurements. Also I thank S. Diplas for finding me the time always to do the XPS experiments. I would also like to express my gratitude for M. Stange, SINTEF, Oslo for preparing PdAg thin films. Also I thank Ø. Borck for performing DFT calculations.

I am also very grateful to the members of MAX Lab at LUND University, Sweden for their support to perform the experimental works during my stay. I also would like to thank all my colleagues at NTNU and SINTEF for making my work environment pleasant with a special thanks to all people who have helped and inspired me during my doctoral study. The financial support from the Research Council of Norway and the Department of Physics is greatly acknowledged.

I have to thank Dr. Ganapathy Subramaniam and family who motivated me highly and gave me confidence that I can do my PhD in abroad and lead my life. I would like to seize this opportunity for thanking my friends in Trondheim and Oslo for their caring and kindness during the past years and especially in my medical treatment period.

I am highly obliged to my father, Mr.D.Ramachandran for his care and love. Being a teacher, he committed himself to provide me with a best possible environment for my

studies. I also indebted to my beloved mother Mrs.R. Mallika for her friendly nature with me, her attentiveness to my thoughts and understanding in all aspects. This dissertation is simply impossible without their incessant love and support throughout my life. I also thank my beloved brothers Balakrishnan and Sureshbabu for their strong and continuous support during this period.

This part will not be completed if I do not thank my beloved husband Mr. A. Krishnasamy for encouraging me every day since the first day of our talks. I thank him for his understandings, patience, and kindness. He came in my life to support and motivate me at the right time. I would like to thank my in-law family also for supporting me. Last but not least, thanks to god, who made all things possible by giving me strength to overcome the challenges in my life in the last four years and to make the rest of the life become more meaningful and beautiful.

List of abbreviations

Å	Ångstrom (1Å = 10^{-10} m = 10 nm)
AES	Auger electron spectroscopy
Ag	Silver
Ar	Argon
AFM	Atomic force microscopy
CO	Carbon monoxide
CO_2	Carbon dioxide
˚C	Degree centigrade
DFT	Density functional theory
FWHM	Full width at half maximum
L	Langmuir (1 L = 1.33×10^{-6} mbar.s)
MFC	Mass flow controller
PES	Photoelectron spectroscopy
Pd	Palladium
RMS	Root mean square
RT	Room temperature
SCLS	Surface core-level shift
SPM	Scanning probe microscopy
STM	Scanning tunnelling microscopy
UHV	Ultra high vacuum
XPS	X-ray photoelectron spectroscopy

List of Papers

Paper I *Hydrogen permeation of thin, free-standing Pd/Ag23% membranes before and after heat treatment in air.*
A. L. Mejdell, H. Klette, A. Ramachandran, A. Borg, and R. Bredesen, Journal of Membrane Science, 2008. **307**(1): p. 96-104.

Paper II Surface *characterization of thin Pd/Ag 23 wt% membranes after different thermal treatments*.
A. Ramachandran, W. M. Tucho, A. L. Mejdell, M. Stange, H. Venvik, J. Walmsley, R. Holmestad, R. Bredesen and A. Borg. To be submitted to Appl. Surf. Sci.

Paper III *Thin Pd-23%Ag/stainless steel composite membranes: Long-term stability, life-time estimation and post-process characterisation.*
T.A. Peters, W.M. Tucho, A. Ramachandran, M. Stange, J.C. Walmsley, R. Holmestad, A. Borg, and R. Bredesen, Journal of Membrane Science, 2009. **326**(2): p. 572-581.

Paper IV *Methanol Adsorption on Pd(110) and Ag/Pd(110) studied by High Resolution Photoelectron Spectroscopy.*
A. Ramachandran, Ø. Borck, T.H. Andersen, I.-H. Svenum, L. E. Walle and A. Borg. To be submitted to Surf. Sci.

Paper V *Adsorption and decomposition of methylamine on Pd(110) studied by high resolution photoelectron spectroscopy and DFT calculations.*
T.H. Andersen, A. Ramachandran, Ø. Borck, I.-H. Svenum, L.E. Walle and A. Borg. Manuscript in preparation.

Specifications of my contribution to the included papers

Paper I Part of the experiments was performed by me. The paper was written primarily by A. L. Mejdell.

Paper II All experimental works were performed by me except the permeation results on 5 µm and 10 µm membranes. The paper was written by me.

Paper III Surface characterization experiments and analysis using AFM, XPS and AES in addition to optical microscopy were performed by me. The paper was written jointly.

Paper IV Experimental works were performed jointly. Spectral analysis was performed by me. The paper was written by me.

Paper V Experimental works were performed jointly. Spectral analysis was performed jointly. DFT calculations were performed by Ø. Borck. The paper was written jointly.

In addition to these papers, I have also made contributions to the following work:

W. M. Tucho, J. C. Walmsley, M. Stange , A. Ramachandran, H. J. Venvik, R.H. Mathiesen, A. Borg, R. Bredesen and R. Holmestad. *Microstructural studies of self-supported (1.5-10µm) Pd/23wt.% Ag membranes tested for hydrogen separation.*

Table of contents

1 Introduction

In our every day life, energy plays a predominant role in one form or the other. The law of conservation of energy [1] states that 'energy can never be created or destroyed' but it can be transformed into other forms of energy. A widely used form of energy is electricity and it can be generated from fossil fuels such as coal, oil and natural gas which are non-renewable resources. The production and use of such fuels has detrimental environmental impacts. Burning any fossil fuel produces carbon dioxide, which contributes to the "greenhouse effect". In 2004, CO_2 was responsible for 75% of the global greenhouse gas emissions [2]. The fast depletion of existing reserves of fossil fuels [3] demand alternative fuels with less environmental impact. A shift toward fuels from renewable sources like biomass [4], hydropower [5], wind power [6], solar power and hydrogen is taking place all around the world.

The attractiveness of hydrogen as an energy carrier is that it can be produced from various sources including water, other renewable sources and fossil fuels. Industrially hydrogen can be produced from methanol, ethanol, and other hydrocarbon fuels by several methods which includes partial oxidation (reaction of hydrocarbons with oxygen) [7-10], methane reforming (reaction of natural gas with steam in the presence of catalysts) [11-15], methanol reforming (reaction of methanol with steam in the presence of catalyst) [16, 17] , water gas shift [17] and electrolysis of water [18]. All the above process produces hydrogen with impurities, except electrolysis which is expensive compared to the other methods [19, 20].

Hydrogen can be used to produce electricity using fuel cells. A fuel cell is an electrochemical energy conversion device that converts the energy of a chemical reaction directly into electricity [21]. As an example, proton exchange membrane (PEM) fuel cells convert the chemical energy of hydrogen and oxygen into electricity. Their high efficiency and zero emission have made them a prime candidate for powering the next generation of electric vehicles.

Presently, methanol is the preferred fuel as direct methanol fuel cells (DMFCs), easily can be incorporated in cars and since the storage of pure hydrogen is difficult due to its low energy density [22]. Furthermore fuel cells require relatively pure hydrogen to prevent catalyst poisoning [23] which makes the purification of hydrogen rich gases more important. The importance of clean hydrogen energy initiated research on production of pure hydrogen using inorganic membranes. This thesis is part of that research.

1.1 Inorganic membranes

Inorganic membrane materials provide good thermal and chemical stability which makes them suitable for many chemical reactions compared to polymer materials [24]. These membranes can be metallic [25-27], silica based [28-30], ceramic [31, 32], zeolite based [33] or carbon-based [34, 35]. They can be either dense or porous. A

comprehensive review on hydrogen production and purification of hydrogen using different kinds of membranes can be found in [36].

Due to its high hydrogen selectivity and permeability, Pd is extensively used as a membrane material. A number of other metals including tantalum (Ta), niobium (Nb), and vanadium (V) have been suggested as an alternative to Pd and Pd based alloys for hydrogen permeating membranes. Compared to other metals, Pd has considerably higher solubility and it absorbs about 600 times its volume of hydrogen at room temperature [37]. However the pure Pd membranes have certain limitations in hydrogen transport due to its Pd-H phase transition [38], therefore other metals have been considered.

1.1.1 Palladium-hydrogen system

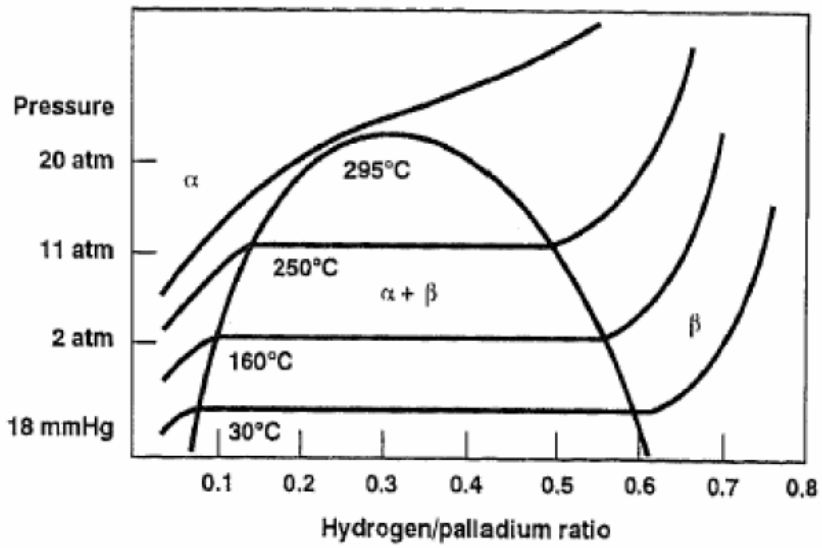

Figure 1.1. Hydrogen pressure-composition isotherms in pure palladium [39]

Hydrogen pressure-composition isotherms in pure palladium consists of three phases below a critical temperature and pressure as shown in Fig. 1.1, a low hydrogen concentration phase (α), a high hydrogen concentration phase (β) and a mixed phase in between these two (α+β), in the so-called miscibility gap. As is seen in Fig. 1.1. the miscibility gap is gradually reduced as the temperature increases and vanishes at the critical value. The critical temperature and pressure for pure palladium are given by T_c ~300˚C and p_c ~2MPa [39-41] . The phase-transitions occur because of new arrangements of the hydrogen atoms in the metal lattice [42]. The lattice in the β phase is considerably expanded compared to the lattice in the α phase, therefore the co-existing phase (α+β) can lead to severe strains, resulting in distortion and hardening of the membrane. Therefore, the membrane may get embrittled after undergoing a few cycles of hydrogen exposure. The mixed phase should be avoided during hydrogen diffusion through the Pd-membranes. This can be obtained by operating the membrane in a single phase region either α or β by maintaining the temperature above the critical

value as long as the membrane is in hydrogen atmosphere. It is important to ensure that the cooling of pure Pd membranes is taking place under dehydrogenated conditions i.e. after complete removal of hydrogen from the system.

1.1.2 Pd-alloys

The lattice parameters change considerably when palladium is alloyed with other metals and thus the miscibility gap (see chapter 1.1.1) varies for different alloying elements and also with the composition of the alloy [42]. It has been reported that increasing the Ag content in a Pd-Ag alloy decreases the critical temperature [41]. Palladium alloys with ~23 wt% silver as alloying element have been found to be an optimum composition with several advantages. This alloy decrease the critical temperature (see chapter 1.1.1) to room temperature and compared to the other metals like Cu, Ce, Au [41] the hydrogen permeability of Pd-Ag alloys is higher. Several tertiary Pd alloys, such as Pd-Ag-Au and Pd-In-Ru, are also reported to have high hydrogen permeability [43]. The high cost of Pd metal is a critical issue regarding applications of Pd based inorganic membranes [36]. In order to overcome this problem researchers focus on producing membranes with thickness of only a few micrometers [26]. The reduction in membrane thickness has a significant double effect of higher permeance and lower material cost. SINTEF has successfully developed a method for producing free standing, dense Pd/Ag 23wt % thin films (henceforth will be labelled as PdAg membranes in the thesis) of thickness down to about 1μm by a combination of magnetron sputtering and a lift-off technique [44, 45].

1.1.3 Hydrogen permeation

The hydrogen permeation process through a membrane comprises several steps including dissociative adsorption of H_2 at the surface on high pressure side of the membrane, the transition of atomic hydrogen from the surface into the bulk metal, atomic diffusion through the bulk and recombinative desorption from the surface at the low pressure side [46]. The overall hydrogen permeation rate through the membrane may be limited by any one or a combination of these steps. The hydrogen flux through the PdAg membrane is proportional to the square root of the partial pressure difference across the membrane as long as the bulk diffusion is rate limiting [46]. Deviations from this power dependency have been attributed to the fact that other processes may also dominate in the hydrogen permeation process [47-52]. Bulk diffusion is mainly expected to be the rate limiting step for the thick membranes [50, 53].

The hydrogen transport properties of Pd based membranes depend on the combined history of temperature and gaseous exposure in addition to the thickness and the as-prepared material properties. Gaseous species other than H_2 are introduced during various treatments or applied as a component of mixture gases to improve the membrane properties. N_2 present in mixture with hydrogen gave a negative effect on hydrogen permeation [54, 55]. Other species that are often present include O_2/air [56-58], H_2O [17, 59-62], CO [56, 57, 61, 63], CO_2 [61, 62, 64], methanol [17, 56, 58] and H_2S [65-67] of which e.g CO and H_2S may strongly affect permeation even if present only in low concentration. An inhibiting effect of O_2 was reported when present in

mixture with H_2, over a pure Pd membrane [57]. Several authors have reported that the hydrogen flux through Pd-based membranes was enhanced after air treatments at 400˚C and higher [67-69]. They also studied the surface morphology and chemical properties after air exposure of the membranes. [68, 69]. Changes in surface composition and operating temperature were found to limit the hydrogen permeation [70]. Reports in the literature that the surface properties are important for the understanding of the permeation behaviour was the motivation for the present work on Pd/Ag 23wt% membranes. Our focus has been to gain insight into the development of surface topography and chemical composition as a result of thermal treatment of different thickness membranes in different atmospheres/gases and to link these properties to the hydrogen permeation behaviour of the membranes.

1.2 Model systems

In real systems Pd based membranes undergo different thermal treatments and different gas exposures (see chapter 1.1.3.) at elevated temperatures and pressures. The influence of such operating conditions in terms of understanding the hydrogen flux behaviour is important. In addition, the content of Ag alloying element and its segregation behaviour is also important for the permeation. Furthermore contaminations from atmosphere may affect the surface properties. Therefore, real membranes are complex system, not easily characterized or understood. To completely understand the chemical properties, it is essential that the sample is clean. This can be achieved by using UHV systems. The investigations on model systems are required to provide quantified information of chemical properties.

In the PdAg thin membrane catalytic reactor experiments it is observed that the hydrogen flux through the membrane increases with increasing temperature. This is likely due to lower coverage of adsorbed species on the membrane surface at higher temperatures. The adsorbed species may be CO, CO_2, H_2O and/or methanol [17]. A strong deactivating effect on the as prepared membranes at temperatures below 255˚C was suggested to be due to methanol or surface adsorbed species originating from methanol [17]. In another report, methanol exposure on Pd based membranes reduced the hydrogen flux by about ~80%. Possible causes for deactivation were suggested to be caused by unconverted methanol [71]. A better understanding of adsorption and co-adsorption behaviour of intermediate species such as CO, CO_2 and methanol on Pd-membranes are thus essential.

In order to investigate the methanol adsorption and decomposition on Pd surfaces we have used high resolution photoelectron spectroscopy. Studying the molecular interactions on the single crystals or model systems and to compare this with corresponding adsorption experiment on the real membranes will lead to a better understanding of the adsorption process. In our study he adsorption and decomposition of methanol molecules Ag/Pd(110) was investigated.

Amines are found to be a promising candidate in an application of CO_2 capture. To investigate the interaction of methylamine on Pd(110) surface and the decomposition behaviour, high resolution photoelectron spectroscopy was performed.

The outline of the following chapters is as follows. In Chapter 2 the experimental techniques and theoretical methods used in this thesis are described. In chapter 3 detailed presentations of the experimental procedures is given. In chapter 4 the summary of the included scientific papers is provided. In chapter 5 a brief description of possible future investigations for the system studied in the thesis are provided. The scientific papers follow after these chapters. The results from the work on PdAg membranes are presented in paper I-III. The investigations from the model systems are presented in paper IV and V.

1.3 References

[1] Ness H.C.V., *Understanding Thermodynamics*. Published by Courier Dover Publications. 1983.

[2] http://www.mnp.nl/en/dossiers/Climatechange/TrendGHGemissions1990-2004.html.

[3] http://www.roperld.com/science/minerals/FossilFuels.htm.

[4] http://www.ace.uiuc.edu/pERE/conference/papers/long.pdf.

[5] F.R. Forsund, *Hydropower Economics*. 2007.

[6] Tony Burton, David Sharpe, Nick Jenkins, Ervin Bossanyi,2001.

[7] M.L. Cubeiro and J.L.G. Fierro,Journal of Catalysis, 1998. **179**(1): p. 150-162.

[8] I. Eswaramoorthi and A.K. Dalai,International Journal of Hydrogen Energy. In Press, Corrected Proof.

[9] L. Alejo, R. Lago, M.A. Peña and J.L.G. Fierro,Applied Catalysis A: General, 1997. **162**(1-2): p. 281-297.

[10] J. Agrell, G. Germani, S.G. Järås and M. Boutonnet,Applied Catalysis A: General, 2003. **242**(2): p. 233-245.

[11] K. Hou and R. Hughes,Chemical Engineering Journal, 2001. **82**(1-3): p. 311-328.

[12] S. Rakass, H. Oudghiri-Hassani, P. Rowntree and N. Abatzoglou,Journal of Power Sources, 2006. **158**(1): p. 485-496.

[13] J.A.C. Dias and J.M. Assaf,Journal of Power Sources, 2004. **137**(2): p. 264-268.

[14] Y. Yang, X. Du, L. Yang, Y. Huang and H. Xian,Applied Thermal Engineering, 2009. **29**(5-6): p. 1106-1113.

[15] S. Barama, C. Dupeyrat-Batiot, M. Capron, E. Bordes-Richard and O. Bakhti-Mohammedi,Catalysis Today, 2009. **141**(3-4): p. 385-392.

[16] A. Iulianelli, T. Longo and A. Basile,Journal of Membrane Science, 2008. **323**(2): p. 235-240.

[17] B. Arstad, H. Venvik, H. Klette, J.C. Walmsley, W.M. Tucho, R. Holmestad, A. Holmen and R. Bredesen,Catalysis Today, 2006. **118**(1-2): p. 63-72.

[18] http://www.hydrogenhighway.ca/code/navigate.asp?Id=225.

[19] Jamal R. Thompson, Robert D. McConnell, Mohsen Mosleh International Conference on Solar Concentrators for the Generation of Electricity or Hydrogen, Scottsdale, Arizona (NREL/CD-520-38172), 2005.

[20] W.H. Scholz,Gas Separation & Purification, 1993. **7**(3): p. 131-139.

[21] L.-j. Yu, Ren., Geng-po Qin, Ming-jun Jiang, Xiu-min,Renewable Energy, 2009. **34**(3): p. 530-543.

[22] http://fuelcellsworks.com/Justthebasics.html.

[23] J.B. Collins, P. Sacramento, P.A. Rikvold and J.D. Gunton,Surface Science, 1989. **221**(1-2): p. 277-298.

[24] N. Agoudjil, N. Benmouhoub and A. Larbot,Desalination, 2005. **184**(1-3): p. 65-69.

[25] S. Uemiya, T. Matsuda and E. Kikuchi,Journal of Membrane Science, 1991. **56**(3): p. 315-325.

[26] Uemiya. S, Yukinori Kude, Kohzoh Sugino, Noboru Sato, Takeshi Matsuda and Eiichi Kikuchi,Chemistry Letters, 1988. **17**(10): p. 1687.

[27] R. Bredesen, H. Klette,, *'Method of Manufacturing Thin Metal Membranes' US Patent No. 6086729A*. 2000.
[28] K. Kusakabe, F. Shibao, G. Zhao, K.-I. Sotowa, K. Watanabe and T. Saito,Journal of Membrane Science, 2003. **215**(1-2): p. 321-326.
[29] Y. Iwamoto, K. Sato, T. Kato, T. Inada and Y. Kubo,Journal of the European Ceramic Society, 2005. **25**(2-3): p. 257-264.
[30] J.C. Diniz da Costa, G.Q. Lu, V. Rudolph and Y.S. Lin,Journal of Membrane Science, 2002. **198**(1): p. 9-21.
[31] U. Balachandran, T.H. Lee, L. Chen, S.J. Song, J.J. Picciolo and S.E. Dorris,Fuel, 2006. **85**(2): p. 150-155.
[32] S.T.O. Y. Gu,Advanced Materials, 2007. **19**(12): p. 1636-1640.
[33] N. Nishiyama, M. Yamaguchi, T. Katayama, Y. Hirota, M. Miyamoto, Y. Egashira, K. Ueyama, K. Nakanishi, T. Ohta, A. Mizusawa and T. Satoh,Journal of Membrane Science, 2007. **306**(1-2): p. 349-354.
[34] Y. Xiao, Y. Dai, T.-S. Chung and M.D. Guiver,Macromolecules, 2005. **38**(24): p. 10042-10049.
[35] L. Shao, T.-S. Chung and K.P. Pramoda,Microporous and Mesoporous Materials, 2005. **84**(1-3): p. 59-68.
[36] G.Q. Lu, J.C. Diniz da Costa, M. Duke, S. Giessler, R. Socolow, R.H. Williams and T. Kreutz,Journal of Colloid and Interface Science, 2007. **314**(2): p. 589-603.
[37] R. Hughes,Membrane Technology, 2001. **2001**(131): p. 9-13.
[38] J. Grashoff, C.E. Pilkington, C.W. Corti,Platinum Metals Rev., 1983. **27**(4): p. 157-169.
[39] A.L. Athayde, R.W. Baker and P. Nguyen,Journal of Membrane Science, 1994. **94**(1): p. 299-311.
[40] G.J. Grashoff, C.E. Pilkington, C.W. Corti.,Plat. Met. Rev., 1983. **27**: p. 157.
[41] Knapton A.G.,Plat. Met. Rev., 1977. **21**: p. 44.
[42] A.K.M. Fazle Kibria, T. Tanaka, Y. Sakamoto.,Int. J. Hydrogen Energy., 1998. **23**(10): p. 891.
[43] G.B.P.A. Shu J, Van neste A, Kaliaguine S.,Can. J. Chem. Eng., 1991. **69**(5): p. 1036-1060.
[44] R. Bredesen, H. Klette.,,US Patent No. 6086729A, 2000.
[45] H. Klette, R. Bredesen,Membrane Technology, 2005. **5**: p. 7-9.
[46] T.L. Ward and T. Dao,Journal of Membrane Science, 1999. **153**(2): p. 211-231.
[47] A.B. Antoniazzi, A.A. Haasz and P.C. Stangeby,Journal of Nuclear Materials, 1989. **162-164**: p. 1065-1070.
[48] J.P. Collins and J.D. Way,Industrial & Engineering Chemistry Research, 1993. **32**(12): p. 3006-3013.
[49] V. Jayaraman and Y.S. Lin,Journal of Membrane Science, 1995. **104**(3): p. 251-262.
[50] R.C. Hurlbert and J.O. Konecny,The Journal of Chemical Physics, 1961. **34**(2): p. 655-658.
[51] I. Ali-Khan, K.J. Dietz, F.G. Waelbroeck and P. Wienhold,Journal of Nuclear Materials, 1978. **76-77**: p. 337-343.
[52] S. Yan, H. Maeda, K. Kusakabe and S. Morooka,Industrial & Engineering Chemistry Research, 1994. **33**(3): p. 616-622.

[53] S. Uemiya, N. Sato, H. Ando, Y. Kude, T. Matsuda and E. Kikuchi,Journal of Membrane Science, 1991. **56**(3): p. 303-313.
[54] A.L. Mejdell, M. Jøndahl, T.A. Peters, R. Bredesen and H.J. Venvik,Journal of Membrane Science, 2009. **327**(1-2): p. 6-10.
[55] F. Gallucci, A. Basile and E. Drioli,Separation & Purification Reviews, 2007. **36**(2): p. 175 - 202.
[56] H. Amandusson, L.G. Ekedahl and H. Dannetun,Surface Science, 1999. **442**(2): p. 199-205.
[57] H. Amandusson, L.G. Ekedahl and H. Dannetun,Applied Surface Science, 2000. **153**(4): p. 259-267.
[58] H. Amandusson, L.G. Ekedahl and H. Dannetun,Applied Catalysis A: General, 2001. **217**(1-2): p. 157-164.
[59] S.H.K. Jung, Katsuki Morooka, Shigeharu Kim, Sang-Done,Journal of Membrane Science, 2000. **170**(1): p. 53-60.
[60] A. Li, W. Liang and R. Hughes,Journal of Membrane Science, 2000. **165**(1): p. 135-141.
[61] F.C.K. Gielens, R. J. J. Duysinx, P. F. J. Tong, H. D. Vorstman, M. A. G. Keurentjes, J. T. F.,Journal of Membrane Science, 2006. **279**(1-2): p. 176-185.
[62] A. Unemoto, Kaimai, Atsushi Sato, Kazuhisa, Otake, Takanori, Yashiro, Keiji, Mizusaki, Junichiro,Kawada, Tatsuya, Tsuneki, Tatsuya Shirasaki, Yoshinori Yasuda,Isamu,International Journal of Hydrogen Energy, 2007. **32**(16): p. 4023-4029.
[63] T.A. Peters, M. Stange, H. Klette and R. Bredesen,Journal of Membrane Science, 2008. **316**(1-2): p. 119-127.
[64] A.L. Mejdell, Jøndahl, M. T. A. Peters, R. Bredesen, H. J. Venvik,2009.
[65] B.D.C. Morreale, M. V. Howard, B. H. Killmeyer, R. P. Cugini, A. V. Enick, R. M.,Journal of Membrane Science, 2004. **241**(2): p. 219-224.
[66] A. Kulprathipanja, Alptekin, Gökhan O. Falconer, John L. Way, J. Douglas,Journal of Membrane Science, 2005. **254**(1-2): p. 49-62.
[67] Z.Z. Li Yang, Bingjia Yao, Xuhui Gao, Hitoshi Sakai, Tomonori Takahashi,,AIChE Journal, 2006. **52**(8): p. 2783-2791.
[68] L. Yang, Z. Zhang, X. Gao, Y. Guo, B. Wang, O. Sakai, H. Sakai and T. Takahashi,Journal of Membrane Science, 2005. **252**(1-2): p. 145-154.
[69] F. Roa and J.D. Way,Applied Surface Science, 2005. **240**(1-4): p. 85-104.
[70] H. Amandusson, L.G. Ekedahl and H. Dannetun,Journal of Membrane Science, 2001. **193**(1): p. 35-47.
[71] K. Hou and R. Hughes,Journal of Membrane Science, 2002. **206**(1-2): p. 119-130.

2 Experimental Techniques

The experimental techniques used for preparing and characterizing the PdAg membranes and the single crystal systems are presented here. Thin PdAg membranes were prepared using magnetron sputtering. The principle of the magnetron sputtering technique is described in chapter 2.1. The different thermal treatment procedures and the performance of hydrogen flow measurements through the PdAg membranes are described in chapter 3. In chapter 2, we further present the surface characterization techniques used in our work. Topography analysis was performed by Atomic Force Microscopy (AFM) described in chapter 2.2. The surface composition analysis was studied by X-ray Photoelectron spectroscopy (XPS) described in chapter 2.3 and the depth profile of the composition, investigated by Auger Electron Spectroscopy (AES), is described in chapter 2.4. For the model systems investigated in this work, high resolution photoelectron spectroscopy was performed using synchrotron radiation as the light source. Density Functional Theory (DFT) was used for complementary analysis of the model system and this theoretical approach is briefly presented in chapter 2.5. Core level analysis and the fitting procedure for the high resolution photoemission spectra are presented in chapter 2.6.

2.1 Magnetron sputtering

There are several different physical vapor deposition methods for producing thin films in a vacuum environment of which sputter deposition is one. The advantages of the sputtering technique over the other methods for thin film coating are described elsewhere [1]. Magnetron sputtering applied in the present work is an ion beam sputtering technique for depositing thin film from different metal or alloy targets on a wide range of substrate materials. A schematic diagram of the principle of magnetron sputtering is shown in Fig. 2.1.

A gas discharge, the plasma is created in front of the target. A negative dc voltage applied to the target (cathode). This creates a voltage drop in the region close to the target surface, causing an acceleration of the positive ions (commonly argon) in the gas plasma towards the target. The bombardment causes sputtering of target atoms from the surface, and the emitted atoms are collected on the substrate while secondary electrons may also be released. These secondary electrons may in turn ionize argon gas atoms and thus sustaining the plasma discharge. An electric field is applied between the substrate and the target while a magnetic field is applied parallel to the cathode. The electric field is normal to the target surface thereby promoting the release of secondary electrons from the target. These electrons move in cycloidal paths away from the cathode leading to a long path length and increased probability of secondary electron collisions with the argon gas. These collisions will then create the ions necessary to sustain the plasma discharge.

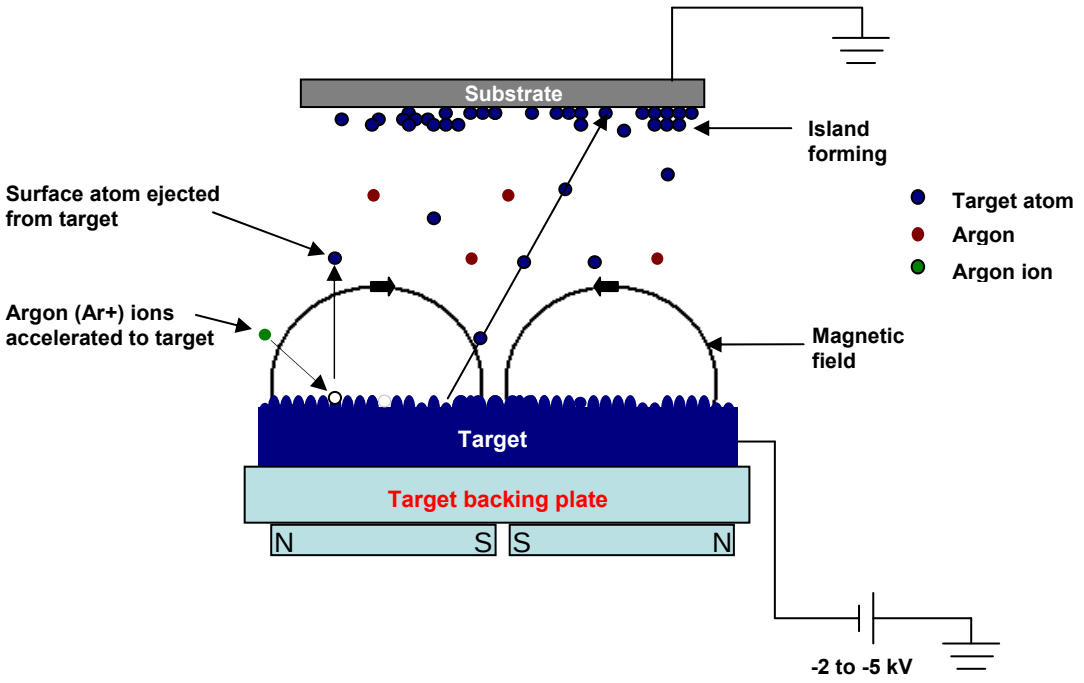

Figure 2.1. Schematics of magnetron sputtering principle and process

In this study, the sputtering was performed with a CVC601 sputtering system and high purity argon (99.999%) was used as a sputter gas. The target was Pd/Ag-23wt% and the substrate was highly polished silicon single crystal wafer. Up to twelve silicon wafers were mounted on a carousel, rotating with constant speed, allowing growth of homogeneous films of uniform thickness. The thickness of the prepared thin films was controlled by the sputtering rate and time. The sputtering procedure has been reported in more detail elsewhere [2, 3]. After sputtering, the film thicknesses were measured by white light interferometry (WYKO NT-2000, Veeco Instruments, USA).

2.2 Atomic force microscopy

The atomic force microscope is one of the main techniques belonging to the Scanning Probe Microscopy (SPM) family of methods. The first SPM technique was Scanning Tunneling Microscopy (STM) [4], invented by Binnig and Rohrer, for which they were awarded Nobel Prize for Physics in 1986 [5].

The basic principle behind the atomic force microscope is to detect the interaction forces between a sharp tip and the sample. A tip is a sharp needle with an atomic probe (apex radius ~20 nm), which is mounted at the end of a cantilever. When the atomic probe tip-cantilever assembly and the surface atoms are close to each other, forces which will depend upon the tip-sample distance will be exerted by the tip-sample

interaction as illustrated in Fig. 2.2. The interaction energy can be described by a Lennard-Jones potential which deals with the interaction between two atoms.

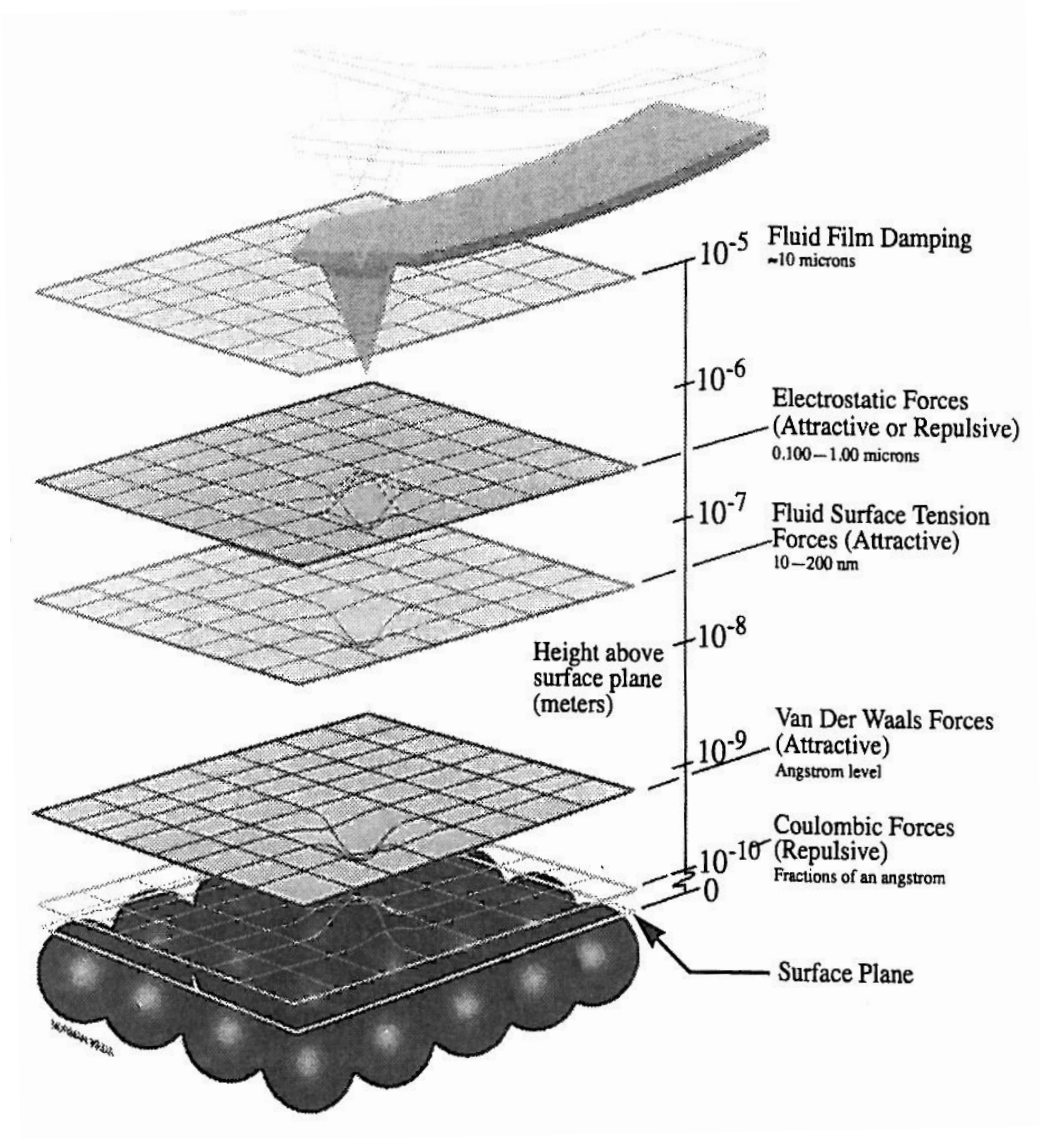

Figure 2.2. Interaction force diagram for two particle system [6]

As can be seen in the Fig. 2.2 when the tip - sample distance is typically sub-Ångstrom, the two atoms are repelled by each other, while the two atoms experience attractive forces when the separation distance is at the angstrom level. In the latter case, the attractive forces exerted by the tip-sample system are known as van der Waals forces. They originates from the polarization of the electron cloud surrounding the atomic core.

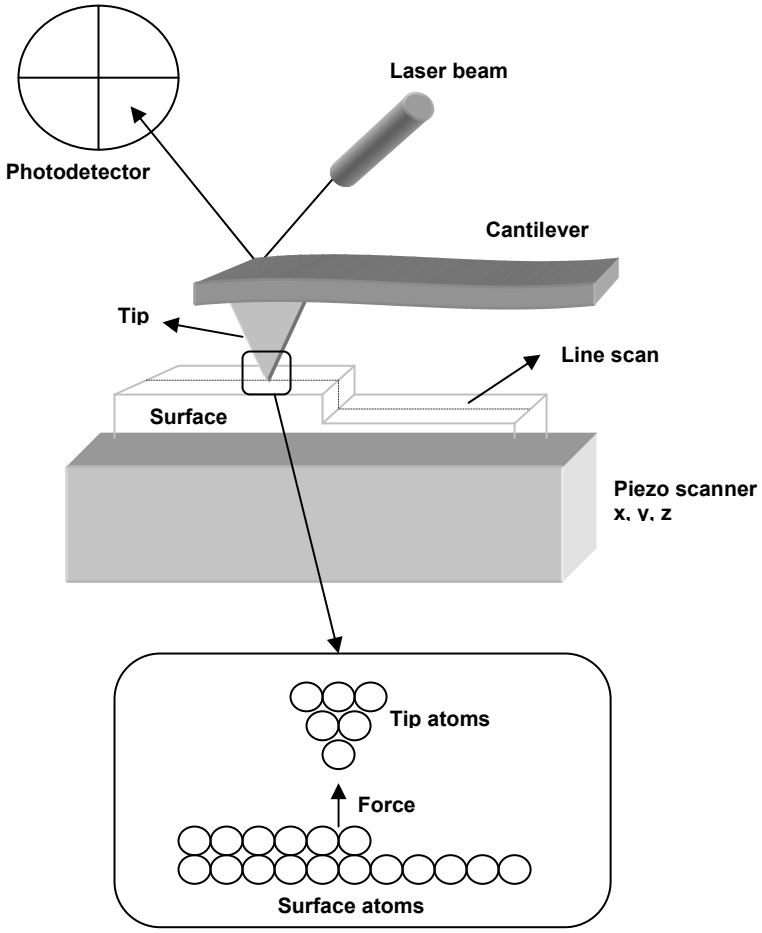

Figure 2.3. Sketch of AFM instrumentation

A schematic drawing of an AFM set-up is shown in Fig. 2.3. A laser beam is incident on the tip-cantilever assembly. The position of the tip can be inferred from the position of the laser spot on the position sensitive detector. Depending on the distance between the tip and sample, the forces experienced change the deflection of the laser beam from the cantilever [7, 8]. Therefore, tracking the deflection of the cantilever gives information on the forces exerted between the tip and sample. The deflection of the cantilever is used to drive a feedback loop which further allows the piezo-electric scanner to adjust the height (z position) of the tip to maintain a constant deflection (i.e. constant force).

The AFM can be used in different modes; (i) contact mode (ii) non-contact mode and (iii) tapping mode. In the contact mode, the tip and the sample remain in close contact during the scan. Compressive forces originating from the tip-sample contact and shear forces attributed to the lateral scan movement may induce elastic and/or plastic deformation of the sample. The non-contact mode, even if it provides no risk to damage

to the sample, results in a lower lateral resolution and slower scan rates. More details on contact mode and non-contact mode are reviewed in [9]. Another mode is called tapping mode, in which the tip-cantilever assembly is allowed to oscillate in free air at its resonant frequency (between 50-50,000 kHz). After approach, the tip-cantilever assembly taps the sample surface with each oscillation and the oscillation amplitude is set to be sufficient to overcome the adhesiveness of the surface. The resulting oscillation amplitude is about 20-100 nm. The oscillation amplitude is measured as an RMS value of the deflection detector signal. Due to the intermittent contact of the tip and sample, a perturbation in oscillation amplitude occurs, which may be detected by the feedback system. The modified oscillation amplitude may be used as a set point, so that when the tip scans the surface, the height variation may be adjusted with the feedback to maintain the set point at a constant value. This is used to generate a high resolution topographic image of the surface. Tapping mode overcomes problems associated with friction, adhesion and electrostatic forces. The advantage of tapping mode compared to the other modes is reviewed in [10]. In the present study, the tapping mode is used for analyzing PdAg membranes.

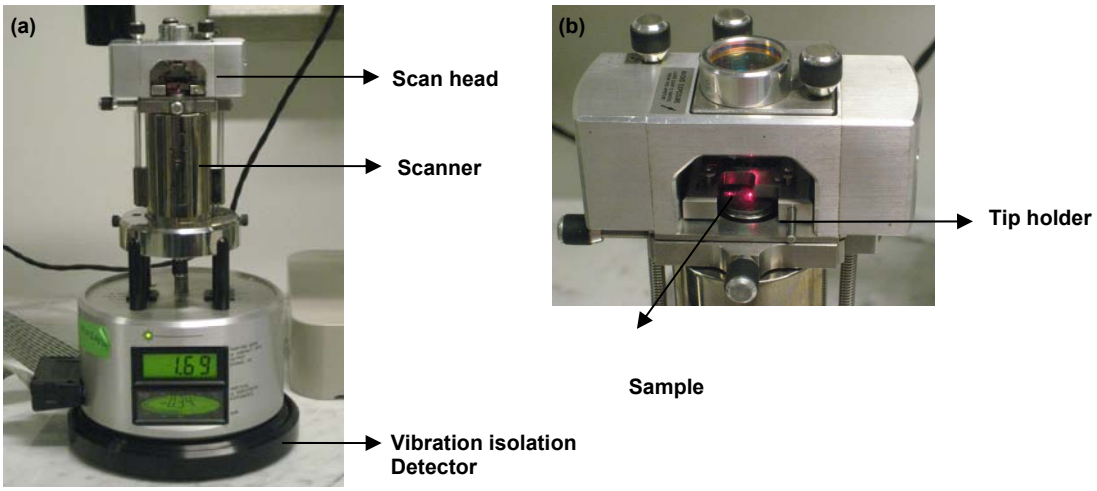

Figure 2.4. (a) AFM instrumental unit (b) Scan head shows the tip holder and sample

The instrument used for our topography analysis was a Multimode SPM from Digital Instruments and it is shown in Fig. 2.4 (a). We used a longer scanner referred to as AS-130 ('J') which yielded 125 µm x 125 µm scan sizes and the vertical range of 5.0 µm [11]. The tips are typically made of Si_3N_4 or Si for AFM. The tips and cantilevers used in this study were made from silicon (NSC15/AIBS/50) with force constant 20-75 N/m, provided by MikroMasch. The tip height was 15-20 µm and had radius of curvature <10nm. The length and width of the cantilever was (125 ± 5)µm and (35 ± 3)µm respectively. The thickness of the cantilever was (4.0 ± 0.5) µm.

The resonant frequency varies for different tips, but was usually found to be between 265 to 400 kHz. Because of this, the driving frequency of the tip is also varied. The amplitude used depends on the type of tip and the sample, but usually was set

approximately to 2 V. The highest resolution imaging was performed with 512 numbers of samples per line in both directions.

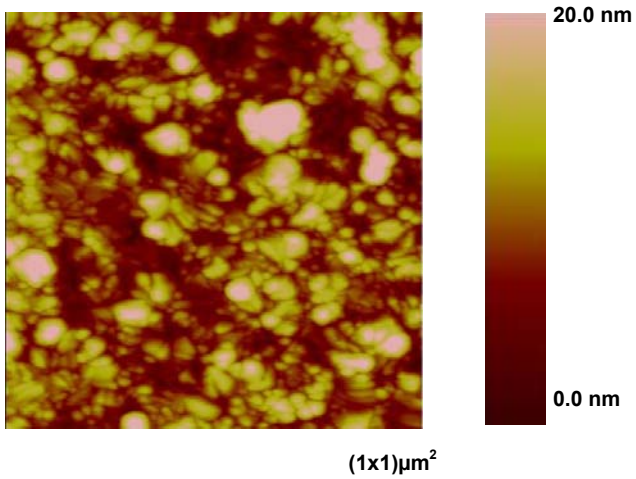

Figure 2.5. AFM image of 2 μm PdAg as-grown film growth surface. The height scale of the image is 20 nm from dark to bright. The scan size of the image is (1x1) μm^2.

Fig. 2.5 shows an AFM image of a PdAg as-grown 2 μm thick film with a scan size of (1x1) μm^2. It shows the height variations of the membrane surface measured in constant force mode. The height scale chosen is 20 nm from dark to bright (white). As can be seen from figure, the surface grains are small.

Analysis of the surface topography measured by AFM was performed with Nanoscope III software [6, 11]. Before quantitative analysis, the images were flattened to the order of either zero or one, depending on the sample flatness.

The surface roughness was calculated as the RMS value of the height deviations within the chosen image size, given by

$$\text{RMS} = \sqrt{\frac{\sum Z_i^2}{n}}$$

Where Z_i is the current height in point 'i' and n is the number of points in the image.

Usually, the entire scan area was used to calculate the surface roughness. The 'particle analysis' command was used to calculate the surface area. For each image, the threshold height (~0.8 nm) was set to calculate the change in surface grains, such as surface area and the grain diameter. The three dimensional area from the entire scan size was used for the calculation of surface area. This is performed by adding the area of all triangles formed by three adjacent data points [11]. The calculation of grain diameter is based on

the average diameter of all grains in the chosen region of the image. The analysis of these parameters was performed using for the entire scan area.

2.3 Electron spectroscopy techniques

The experimental techniques described in this section are, X-ray photoelectron spectroscopy and Auger electron spectroscopy.

2.3.1 The electron mean free path

Electron spectroscopy techniques in general yield information on both electronic and chemical properties of the top few atomic layers of a sample. The electrons emitted through an excitation process from atomic core levels or valence band states interact with the material and may loose energy through inelastic scattering processes limiting the mean free path of the electrons. The change in mean free path of the electrons as a function of their kinetic energies is shown in Fig. 2.6. The data points are measured data from different elemental solids and the dashed line is a model calculation of the mean free path independent of the material [12]. The data points are scattered around the dashed curve, known as the 'universal curve'. As can be seen in the Fig. 2.6 the highest surface sensitivity can be obtained when the electrons have kinetic energies around 50 eV, where the electron mean free path is of the order of 4 Å.

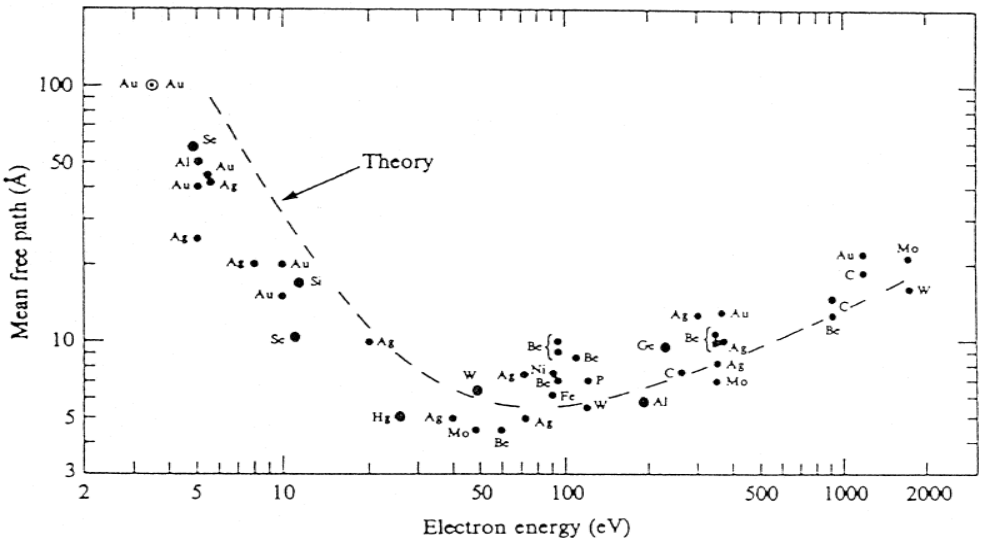

Figure 2.6. The mean free path of electrons in solids. The circles refer to the experimental measurements for different elements and the dashed line is based on the theoretical calculations called as universal curve [12]

2.3.2 X-ray photoelectron spectroscopy

In 1887, H. Hertz discovered a quantum electronic phenomenon called the photoelectric effect in which the electrons are emitted from matter after the absorption of energy from electromagnetic radiation, such as X-rays or visible light [13]. Later in 1905, A. Einstein explained the effect, by suggesting that light propagates and is absorbed in

fixed amounts, called photons [14]. This principle was later developed into the technique called X-ray photoelectron spectroscopy by Kai Siegbahn and his group [15].

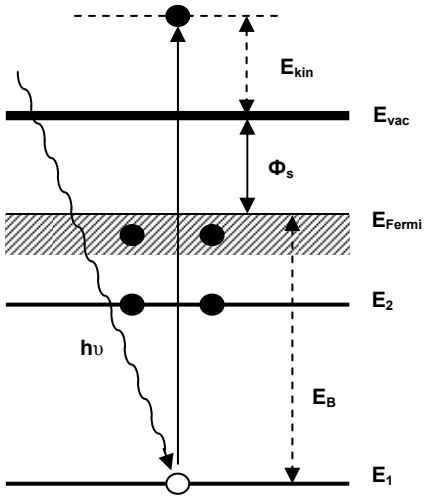

Figure 2.7. Schematic drawing of the principle of PES. hυ is the photon energy, E_1, E_2 are the energy levels of the core electrons, E_{Fermi} and E_{vac} refers the Fermi level energy and vacuum energy level. E_B is the binding energy seen by the electron. [16]

The basic principle of photoelectron spectroscopy is shown in Fig. 2.7. A beam with a certain photon energy hυ penetrates the surface. Photons are absorbed by the atoms and then excite the electron with their various binding energies. The impinging photon has to be above certain energy to emit an electron. This minimum energy is material specific and is denoted as the work function $\Phi_s = h\upsilon_{min}$ of the material. Here h is the Planck constant and υ is the photon energy. A photon with higher energy than the work function will emit electrons with a kinetic energy given by,

$$E_{kin} = h\upsilon - E_B - \Phi_s \qquad (2.1)$$

where hυ is the energy of incoming photon, E_B is the binding energy of the electron and Φ_s is the work function of the material, the energy required to take the electron from the Fermi level to vacuum level $E_{vac.}$

All elements have a unique set of core levels. When they are excited with a specific photon energy, the energy distribution of the elastically emitted electrons will be related to the energy of the core levels from which the electrons are ejected [15, 17, 18]. The kinetic energy of the emitted electrons is measured by an energy analyzer and recorded as an energy distributed spectrum of photoelectrons. When electrons in different core levels are excited with the same photon energy, it gives rise to characteristic peaks in the kinetic energy spectrum. In order to be measured by the energy analyzer, the emitted electron from the core level has to have higher kinetic energy than the work function of the analyzer Φ_A, which may be different from the work function of the sample.

Therefore, the resulting measured kinetic energy (E'_{kin}) is different from that described in equation 2.1, and can be written as [18].

$$E'_{kin} = h\upsilon - E_B - \Phi_A \tag{2.2}$$

Equation 2.2 holds when the sample and the analyzer Fermi are levels aligned. Then the relevant work function becomes that of the analyzer. This process is illustrated in Fig. 2.8.

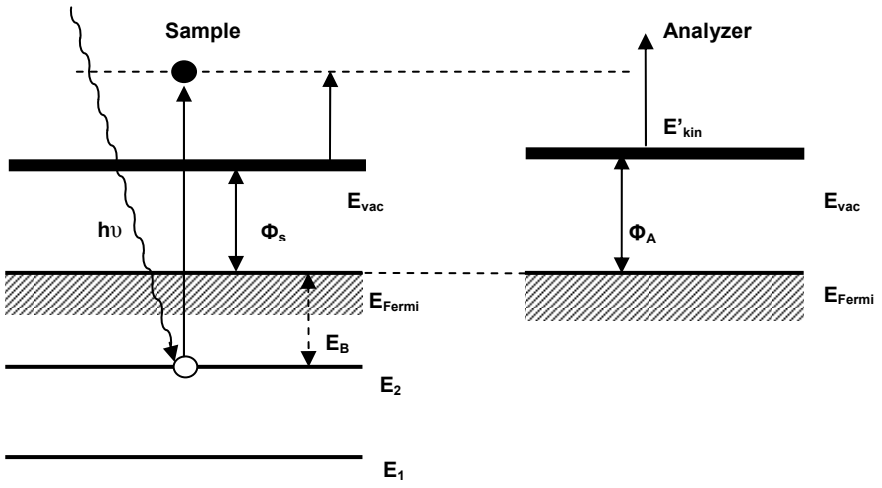

Figure 2.8. Graphical representation of change in work function between the sample and the analyzer. E_1 and E_2 are the core level energies and E_{Fermi} and E_{vac} are for the Fermi level and the vacuum level energies. hν is the photon energy. Φ_s and Φ_A are the work function of the sample and analyzer respectively.

In addition, we recorded each core level measurements followed by the corresponding Fermi edge spectra to perform the Fermi level alignment (see paper IV).

The photoemission process is the simplest picture as far as the approximation that the energy distribution of photoelectrons should correspond to the energy distribution of electron states in the solid surfaces. In practice, the probability of photons being absorbed and electrons excited are not the same for each electron state of the solid surfaces and are also dependent on the incident energy. There is a variety of possible final states of the ion from each element, and therefore there is a corresponding variety of kinetic energies of emitted electrons. In addition, there is different probability or cross-section for each final state.

A number of light sources and radiation frequencies are available today. Common conventional sources for the primary radiation are AlKα (1486.6 eV) and MgKα (1253.6 eV) sources. Synchrotron radiation light sources produce soft X-rays in a wide energy range. Synchrotron sources are described briefly in chapter 2.3.3. The two radiation sources we used for the work presented in the thesis are a dual anode

monochromated X-ray source with photon energy 1486.6 eV (AlKα) and synchrotron radiation source with variable photon energies from 10-2000 eV.

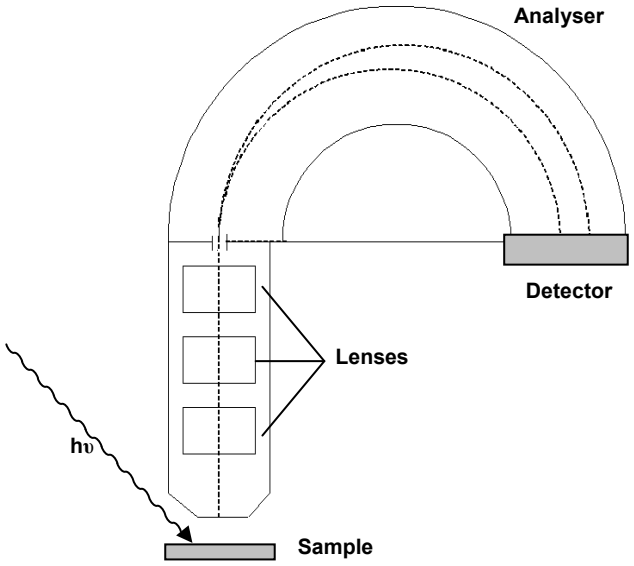

Figure 2.9. Schematics of electron spectrometer used to detect the photoelectrons emitted from the surface using soft X-rays.

A schematic sketch of an electron spectrometer used to detect photoelectrons is shown in Fig. 2.9. Different set of electron lenses, an energy analyzer and detector are integrated in this unit. When a monochromated AlK_{α} radiation source excites the electrons from the solid surface, they will be collected by the electron optics, where the electrostatic lenses focus the collected electrons onto the analyzer entrance slit and also decelerate or accelerate the electron to the kinetic energy set as the pass energy of the analyzer. The detector commonly consists of micro channel plates connected to a phosphor screen at the end of the analyzer. The electrons which pass through the analyzer are detected by these micro channel plates and then accelerated to the phosphor screen producing light flashes which are further detected by a CCD camera. The XPS results from the papers in this thesis related to PdAg membranes were performed with a KRATOS AXIS ULTRA^{DLD} spectrometer using monochromatic AlKα radiation (hν =1486.6 eV).

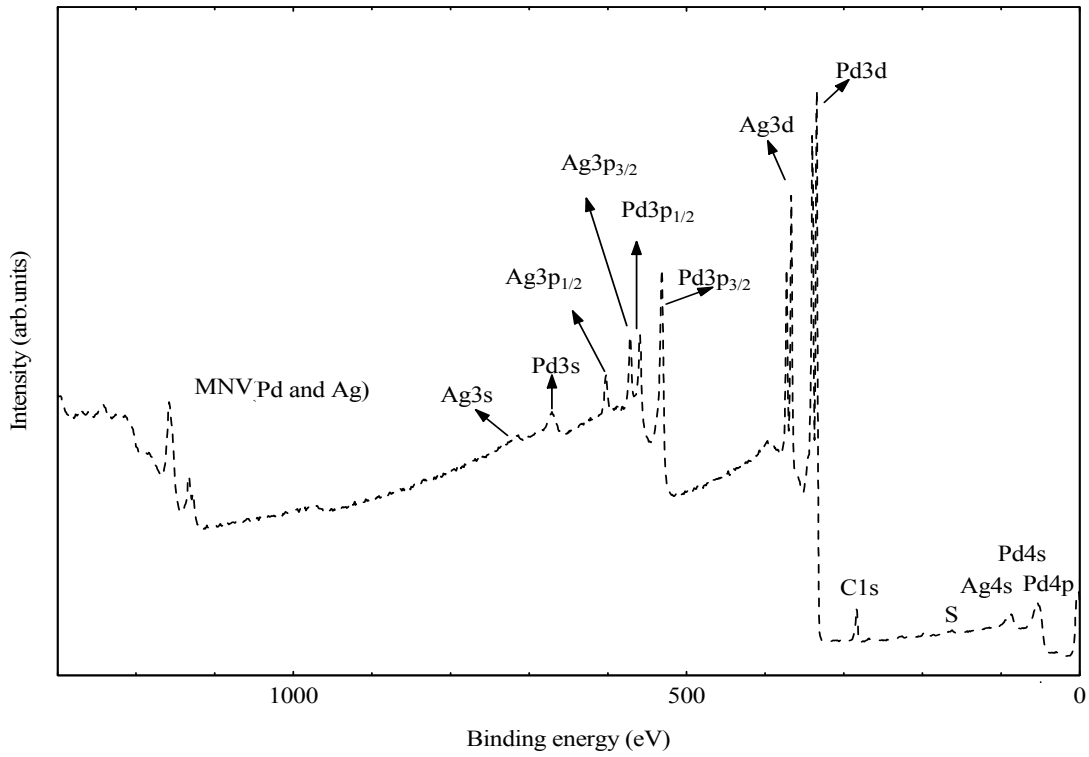

Figure 2.10. Widescan XPS spectra for PdAg as-grown thin film

A wide scan photoelectron spectrum recorded from an as-grown PdAg membrane is shown in Fig. 2.10. The core levels of Pd3d, Ag3d, Pd3p (coinciding with O1s [19]) and C1s can be identified. The Auger signals (will be described in chapter 2.4.) can be seen at higher binding energies (> 1000 eV) while the valence states (will be described in chapter 2.3.6) are at low binding energies close to Fermi level.

Also, a $Pd3d_{5/2}$ core-level spectrum recorded for a 2 μm thin membrane exposed to pure oxygen at 300˚C is shown in Fig. 2.12. A more thorough description of the features of core the level photoelectron spectrum will be presented in chapter 2.3.4. The intensity distribution of the core level peaks contains quantitative information about the chemical composition of the surfaces. In order to determine the intensity of the core level peaks, we performed curve fitting procedures as will be discussed in chapter 2.6.

2.3.3 Synchrotron radiation

Synchrotron radiation is electromagnetic radiation which is generated by the acceleration of charged particles moving in circular orbits at relativistic speeds. In storage rings, synchrotron radiation is produced by fast moving electrons, and they are accelerated by the bending magnets and by insertion device (wiggler or undulator). The emitted photons are directed along the tangent of the electron orbit where the electron beam is bent. This radiation is collected in beam-lines which use focusing mirrors and various types of monochromators. Synchrotron radiation source is superior to other light sources, due to its unique properties of wide spectral range, high brilliance (high intensity of photons) and high collimation of the light beam [18]. The results presented in paper IV and V were performed at I311 beam-line at MAX-lab, LUND which is a beam line utilizing radiation from an undulator. The design of the beam-line is described elsewhere [20]. A schematic top and side view of I311 beam-line is shown in Fig. 2.11. M1 is the cylindrical pre-mirror where the light from the undulator is focused. The plane mirror M2 moves synchronously with monochromator grating (G) and is then followed by a spherical mirror (M3). This arrangement keeps the image of the virtual source (S') fixed on the exit slit (S1).

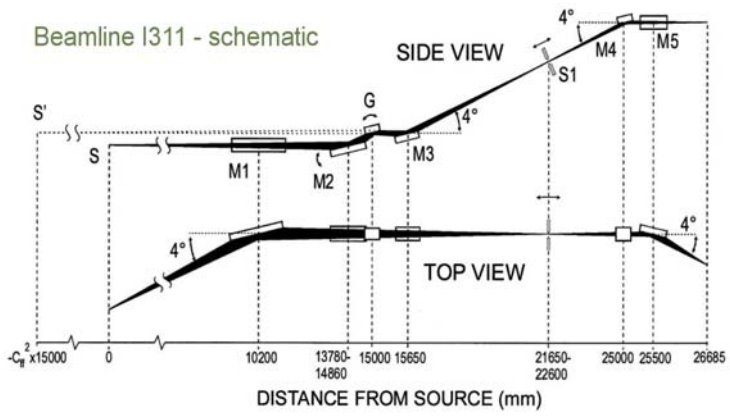

Figure 2.11. Schematics of I311 beam line top view and side view shown in the upper and lower panels respectively [20]

2.3.4 Core level spectroscopy

Core level spectroscopy is used to probe the electrons close to the nuclei. The atomic orbitals are more localized and thus give information about the properties of individual atoms. The core level electrons are not directly participating in chemical bonding, but yet this may affect the binding energy of the specific electron due to the chemical environment. Changes in local charge and potential of an atom due to chemical environment cause shifts in the core level binding energies [21]. The consequence of this is a difference in binding energy, called chemical shift. These shifts were unambiguously observed by Hagström et.al for the first time [22].

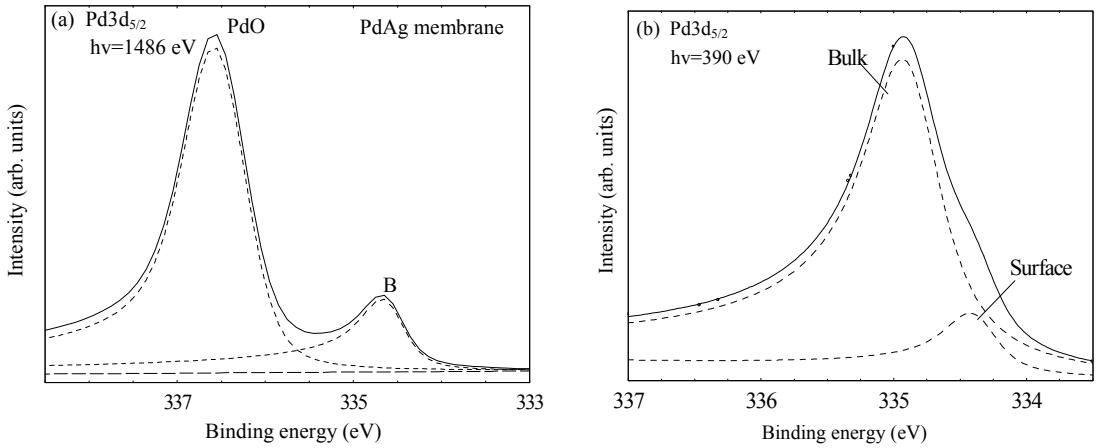

Figure 2.12. (a) $Pd3d_{5/2}$ core level spectra of thin PdAg membrane exposed in pure oxygen (see paper II for details) (b) $Pd3d_{5/2}$ high resolution core level spectra for clean Pd(110 (see paper IV for details)

As an example, fully developed PdO with a chemical shift ~1.9 eV on the surface of PdAg membrane surface is shown above in Fig. 2.12 (a). The peak B belongs to the bulk Pd component and there is another peak with BE shift ~1.9 eV, due to the surface palladium oxide (PdO) formed on the surface. Due to the strong electronegativity of oxygen, it attracts an additional electronic charge from Pd valence electrons and leaving less electronic charge for Pd. The potential at the Pd sites is lowered and the photoelectrons with lower kinetic energy, i.e. at higher binding energy. In addition, other type of core level shift may occur, for example surface core level shift. The SCLS is the difference in the energy that it takes to remove the core electron from a surface atom and from a bulk atom respectively. SCLS is expected to be larger for more open surfaces due to the deviation from bulk coordination is larger than for a close packed surface. Surface core level shifts from 4d metal single crystal surfaces found experimentally and theoretically are reviewed in [23]. One example of a SCLS from our work is shown in Fig. 2.12 (b), where the $Pd3d_{5/2}$ spectrum of clean Pd(110) is presented. The SCLS is found to be -0.51, eV in this case paper IV.

2.3.5 Vibrational fine structure

During the photoemission process, an electronic transition takes place, which leads to the redistribution of electronic charge in the nuclei thus changing the coloumbic interactions. This process can lead to vibrations of the molecule and may result in characteristic vibrational contributions in the photoemission spectrum. Several studies of alkanes and alkenes have shown that the C-H normal vibrational stretching mode is found at about 400 meV, irrespective of the number of C-H bonds [24-26]. For the gas phase methanol, the first C-H stretch vibrational mode is about 392 ± 6 meV with an intensity ratio of 33 ± 3% compared to the adiabatic component shown in Fig. 2.13. [27, 28]. A slight change in intensity ratio and the binding energy difference for the C-H stretch vibrational component have been found compared to the adiabatic peak are 381 ± 15 meV and 39 ± 2% for methoxy adsorbed on Cu(100) surface [28].

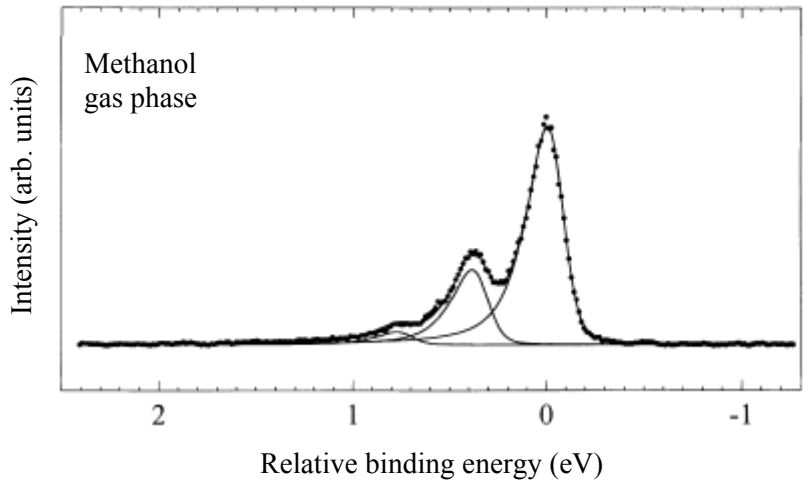

Figure 2.13. C1s core level spectra for CH_3OH gas phase [28].

2.3.6 Valence band region

The spectrum in the valence region consists of many levels close to each other giving rise to a band structure of the material. The electrons in the valence levels have low binding energies and are close to the Fermi level. The electronic states in valence levels are weakly bound and less localized than the core levels and thus the valence spectrum is strongly influenced by the molecular orbital bonding [29]. An example of valence band spectra is shown in Fig. 2.14. The upper spectrum in the figure is recorded after methanol decomposed into CO at 250K (see paper IV). These peaks are related to the outer filled orbitals of adsorbed molecules. The adsorbate induced new spectral features at 8 eV and 11 eV are assigned to the 5σ and 4σ states respectively [30]. The shape of the spectra are often complex and may also vary when the photon energy changes.

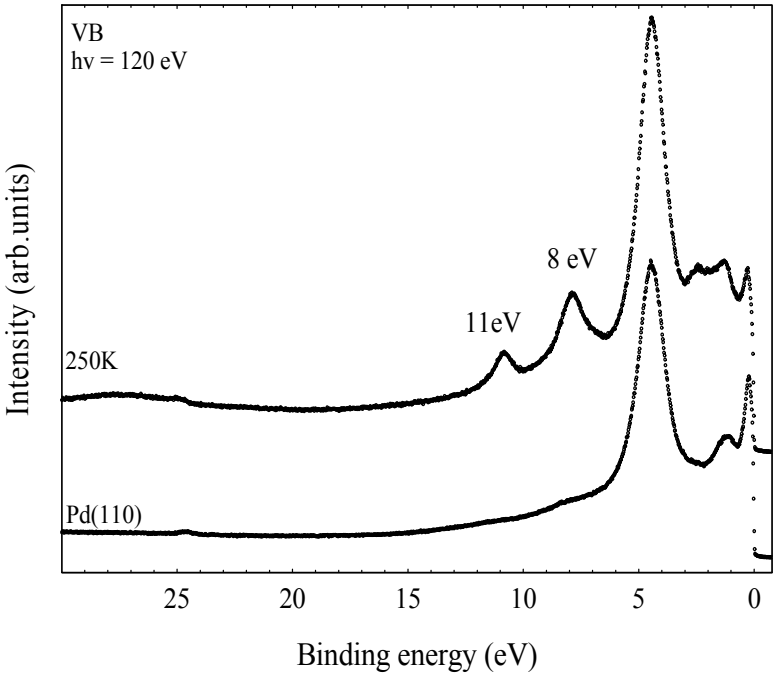

Figure 2.14. Valence band spectra measured for clean Pd(110) (lower spectra) and 0.5L CH_3OH deposited on Pd(110) (upper spectra)

2.4 Auger electron spectroscopy

The Auger effect was discovered independently by both Lise Meitner and Pierre Auger in the 1920's [31, 32]. The Auger electron spectroscopy technique can be used for chemical analysis, in a way similar to X-ray photoelectron spectroscopy. The basic principle of AES is shown in Fig. 2.15. When a core level electron is ejected from the material through excitations by electrons or photons, a core hole is formed. This is an unstable state; hence the core hole can be filled by an outer electron. During the transition of outer electron to the core hole, there is a release of energy equal to the difference in orbital energy. This transition energy may be transferred to a second orbital electron which will be ejected to vacuum when the transfer energy is higher than the new orbital binding energy. An Auger emitted electron will have a kinetic energy of

$$E_{kin} = E_1 - E_2 - E_3 \tag{2.3}$$

where E_1, E_2, and E_3 are the energies of the core level, first outer shell and second outer shell as measured from the vacuum level. The kinetic energy of the emitted electron depends only on the energy levels of the atom; and the distribution of kinetic energies provides a finger-print for the various elements in the sample.

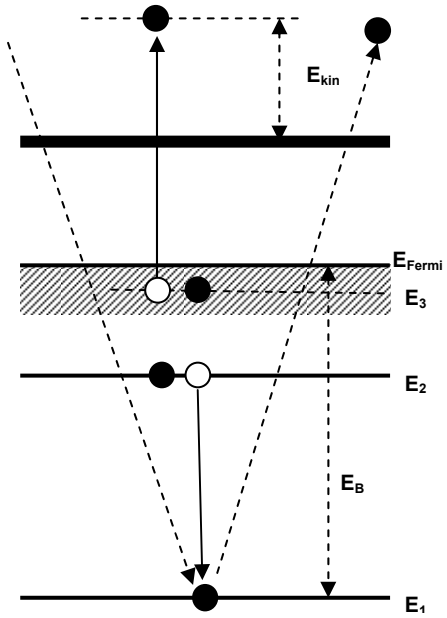

Figure 2.15. Schematics of the principle of AES

A schematic illustration of an AES instrument is shown in Fig. 2.16. An electron gun is used as the excitation source and an energy analyzer detects the Auger electrons. The sample is inclined at 30˚ to maximize the signal yield that can be seen vertically by the analyzer. Auger transitions are seen in XPS measurements too as shown in Fig. 2.10. In order to avoid the large background of secondary electrons, the first derivative of Auger signal intensities is often used. As the detected signals from the AES spectra are from the outermost atomic layers, the depth profile of the chemical composition can be performed by removing layer by layer by using Ar-ion bombardment in conjunction with measuring AES spectra.

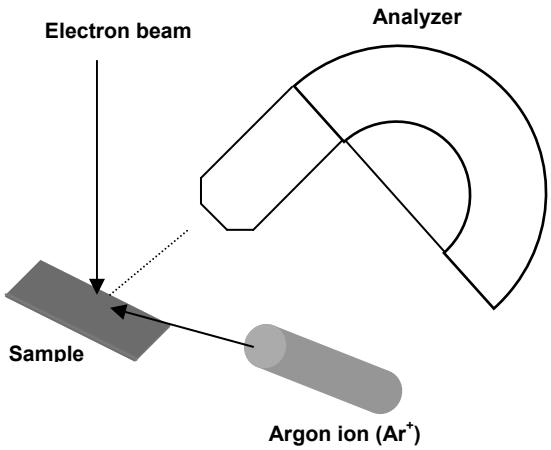

Figure 2.16. Schematic for the AES instrumentation

In this thesis, the depth profile of PdAg thin membranes exposed to pure oxygen at 300˚C (as will be described in chapter 3), was performed. An example of the change in the amount of Pd, Ag and O are plotted in Fig. 2.17 as a function of depth. On the surface, an oxide is formed, and as can be seen in the Fig. 2.17 the amount of Ag is reduced on the surface and after ~2 nm, the oxide disappears and the Ag intensity increases. Quantitative analysis of the Auger spectra after depth profiling was performed with CASAXPS [33]. The relative sensitivity factors for Pd, Ag and O for the JEOL instruments were included for the representative peaks before analyses [34]. These results are discussed in paper II.

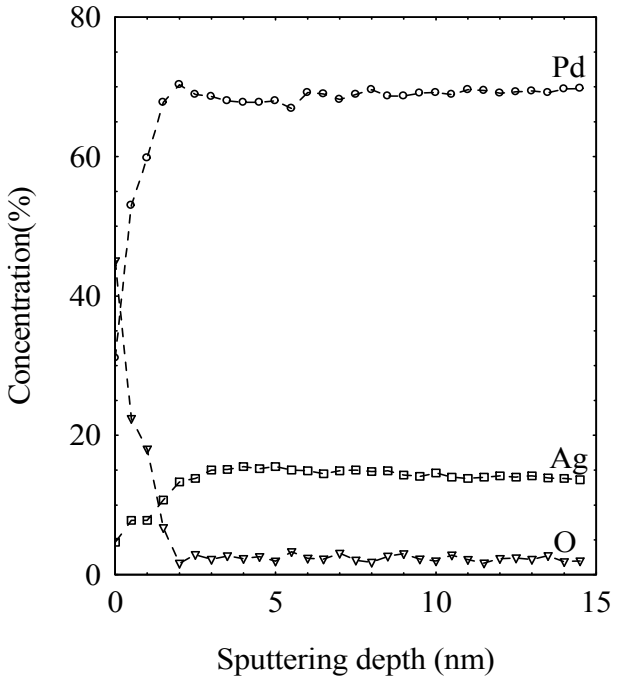

Figure 2.17. AES depth profile for the PdAg thin membranes exposed in pure oxygen. Empty circles refer to Pd, empty squares refer to Ag and empty triangles refer to O on the surface.

2.5 Density Functional Theory

Density functional theory has in the present thesis been used for studying adsorption geometries of adsorbates, interactions between adsorbates and substrates for determining core level shifts. The main advantage of first principle DFT is that no experimental input is needed for performing the calculations. The details of the first principle DFT calculations are not the focus of this thesis, as it is a complementary approach to the experimental work in paper IV and V. A more detailed description of DFT can be found in ref. [35].

To describe the quantum mechanical behaviour of electrons in solids, it is necessary to calculate ground state energy of the system. The energy may be computed by solution of Schrodinger equation, as follows.

$$H\Psi(r_1, r_2, ...r_N) = E\Psi(r_1, r_2, ...r_N) \tag{2.4}$$

The Hamiltonian operator H consists of three terms; the kinetic energy (E_k), the interaction with an external potential (V_{ext}) and the electron-electron interactions (V_{ee}).

$$H\Psi = (E_k + V_{ext} + V_{ee})\Psi \tag{2.5}$$

The equation (2.5) is valid for Born-Oppenheimer approximation, i.e nuclear and electronic motions are largely to be separated due to the faster motion of electrons compared to nuclei.

To determine the ground state energy of any system, it is necessary to calculate the total wave function of the system. In principle, this can be done by solving the Schrodinger equation. Due to the electron-electron interactions (V_{ee}), the Schrodinger equation is not separable which makes it very difficult to solve.

Density functional theory (DFT) is a successful approach for determining the ground state properties of an electronic system. The Hohenberg-Kohn theorem says that the ground state is uniquely defined by the electron density [36].

According to the Kohn-Sham theorem [37], the real system can be replaced by a fictitious system of non-interacting particles moving in an effective potential so that the true charge density is maintained. The Kohn-Sham equation is an exact mapping of the many body Schrodinger equation on to a set of one-electron equations:

$$\left(\frac{-h^2}{2m}\nabla^2 + V_{eff}\right)\varphi_i = \varepsilon_i\varphi_i \tag{2.6}$$

$$V_{eff} = V_H + V_{ext} + V_{xc} \tag{2.7}$$

Where φ is an electron density, V_H is the Hartree potential, V_{ext} is the external potential and V_{xc} is the exchange-correlation potential. In equation (2.7) all contributions can be

calculated except V_{xc} which has to be approximated. The many-electron interactions are contained in V_{xc}

The electron density can be expressed as

$$\sum |\varphi_i|^2 = n(\vec{r}) \tag{2.8}$$

As the potentials are a function of electron density the Kohn-Sham equation (2.6 and 2.7) is solved iteratively until self-consistency is obtained.

2.6 Core level analysis

High resolution core level spectra give information about behavior of atoms in different chemical environments, for example as shown in Fig. 2.11. In order to extract the information available in the photoemission spectra, one has to decompose the spectra into several contributions based on the knowledge of chemical interactions. The parameters included in the decomposition are binding energies, intensities and line shapes of atomic spectra in different chemical environments.

The line shape of any photoemission spectrum depends upon the following parameters.

1. Life time of the core-hole
2. Electron-hole pair excitations
3. Vibrational excitations
4. Electronic shake-up and shake-off contributions
5. Instrumental broadening

2.6.1 Lorentzian function

In the photoemission process, when an electron is excited from a core-level, system is different from the ground state energy. The life time of the excited state is short and the deexcitation proceeds through an exponential decay where the relation between the intensity and life time may be written as

$$I(t) = I_0 \exp(-\Gamma t) \tag{2.9}$$

where t is the excited state life time.

Due to Heisenberg's uncertainty principle, the decay of the excited state induces uncertainty in the binding energy. The Fourier transform of the above equation with respect to energy yields a Lorentzian contribution to the line shape as

$$I_L(E) = \frac{I_0(\Gamma/2)^2}{(E-E_0)^2 + (\Gamma/2)^2} \tag{2.10}$$

where I_0 is the intensity of the peak at $E = E_0$ and Γ is the Lorentzian FWHM [38].

2.6.2 Asymmetry function

The photoemission process is often accompanied by other processes such as excitation of electrons. This will affect the energy of the emitted electron. As an example, if the excitation occurs into bound states so-called shake-up satellites may appear and if the excitation is into the continuum, shake-off satellites appear at the high energy side of the lines in the spectrum. Electron excitations from valence states close to the Fermi level in metals create electron-hole pairs affecting the line shape of the photoemission spectrum.

The asymmetry line shape α is described by a singularity function which can be written as

$$I_\alpha(E) \propto \frac{1}{[(E-E_0)^2]^{\frac{1-\alpha}{2}}} \tag{2.11}$$

When E = E_0, $I_\alpha(E)$ becomes infinite which does not have any physical meaning. But combining this asymmetry with a Lorentzian line shape removes the singularity and the resulting line shape is known as the Doniach-Sunjic line shape [39].

2.6.3 Gaussian contribution

There is another excitation in the photoemission process that may also affect the photoemission spectrum, which is creation of vibrations or phonons. Within the harmonic oscillator approximation, assuming one vibrational mode the energy separation of the vibrational levels and the resulting binding energy shift is proportional to the number of phonons created. The probability of creating n phonons is given by the Poisson distribution,

$$P(n) = \frac{S^n e^{-S}}{n!} \tag{2.12}$$

where S = P(1)/P(0) is the ratio of the probability of creating 1 and 0 phonons, respectively.

The Gaussian broadening of the photoemission peak is given by

$$I_G(E) = I_0 e^{-\frac{\ln 2(E_0-E)^2}{\sigma^2/4}} \tag{2.13}$$

where σ is the Gaussian FWHM.

Instrumental broadening due to finite energy resolution is often assumed to be Gaussian.

2.6.4 The fitting procedure

The final line shape is determined by a convolution of the above three different contributions. With several components present in the spectrum the total line shape of the spectrum is a sum of the line shapes of each component. The fitting procedure in this thesis was performed with the software entitled FitXPS [40]. The input parameters entering into the fitting procedure are binding energy (E_0), intensity (I_0) asymmetry index (α), Lorentzian (L) and Gaussian (G) functions. These parameters will automatically be varied in a search for a total line shape as close to the measured spectrum as possible. The fitting results have to be checked if they make physical meaning, for example the same peak in two successive spectra representing any particular chemical contribution has to have the same fitting parameters. If needed additional constraints have to be applied in the fitting.

2.7 References

[1] S. Swann, Physics in Technology, 1988. **19**(2): p. 67-75.

[2] R. Bredesen, H. Klette. *'Method of Manufacturing Thin Metal Membranes' US Patent No. 6086729A*. 2000.

[3] H. Klette and R. Bredesen. Membrane Technology, 2005. **2005**(5): p. 7-9.

[4] R. H. Binnig. G.,Helv.Phys.Acta., 1982. **55**(726).

[5] G. Binnig, C. F. Quate and C. Gerber, Physical Review Letters, 1986. **56**(9): p. 930.

[6] Santa Barbara. V., *Multimode SPM Instruction Manual, Digital Instruments, Inc,*. 1996.

[7] J. N. Israelachvili,Proe. R. Soc. (London), 1972. **A331**: p. 39.

[8] J. N. Israelachvili, *Intermolecular and Surface Forces, Academic Press, New York. ch.10*. 1985.

[9] C. F. Quate,Surface Science, 1994. **299-300**: p. 980-995.

[10] Q. Zhong, D. Inniss, K. Kjoller and V. B. Elings,Surface Science, 1993. **290**(1-2): p. L688-L692.

[11] C. Fitzgerald, *Nanoscope Command Reference Manual, Version 5.12 (Revision B), Chapter 14 (Digital Instruments/Veeco Metrology Group, Inc.)*. 2001.

[12] A. Zhangwill, *Physics at surfaces, (Cambridge University Press, Cambridge)*. 1988.

[13] H. Hertz,Ann. Physik, 1887. **267**: p. 983.

[14] A. Einstein,Ann. Phys. (Leipzig), 1905. **17**: p. 132.

[15] C. N. N. K. Siegbahn, A. Fahlman, R. Nordberg, K. Hamrin, J. Hedman, G. Johannson, T. Bermark, S.E. Karlsson, I. Lindgren and B. Lindberg, ESCA: Atomic, Molecular and Solid State Structure studied by means of electron spectroscopy, Almqvist and Wiksells, Uppsala (1967).

[16] S. Raaen, *Lecture notes on Electron Spectroscopy*.

[17] S. Hufner,Springer-Verlag Berlin Heidelberg., 2003.

[18] B. D. Ratner, D.G. Castner, Ed.J.C. Vickermen, John Wiley & Sons Ltd, West Sussex.,1997: p. 43.

[19] M. Todorova, E. Lundgren, V. Blum, A. Mikkelsen, S. Gray, J. Gustafson, M. Borg, J. Rogal, K. Reuter, J.N. Andersen, and M. Scheffler.,Surface Science, 2003. **541**(1-3): p. 101-112.

[20] R. Nyholm, J. N. Andersen, U. Johansson, B. N. Jensen and I. Lindau, Nuclear Instruments and Methods in Physics Research Section A: Accelerators, Spectrometers, Detectors and Associated Equipment, 2001. **467-468**(Part 1): p. 520-524.

[21] N. Måtensson and A. Nilsson, Journal of Electron Spectroscopy and Related Phenomena, 1995. **75**: p. 209-223.

[22] S. Hagström, C. Nordling and K. Siegbahn,Physics Letters, 1964. **9**(3): p. 235-236.

[23] J. N. Andersen, D. Hennig, E. Lundgren, M. Methfessel, R. Nyholm and M. Scheffler,Physical Review B, 1994. **50**(23): p. 17525.

[24] S. J. Osborne, S. Sundin, A. Ausmees, S. Svensson, L. J. Saethre, O. Svaeren, S. L. Sorensen, J. Vegh, J. Karvonen, S. Aksela and A. Kikas,The Journal of Chemical Physics, 1997. **106**(5): p. 1661-1668.

[25] L. J. Sæthre, O. Sværen, S. Svensson, S. Osborne, T. D. Thomas, J. Jauhiainen and S. Aksela,Physical Review A, 1997. **55**(4): p. 2748.
[26] T. D. Thomas, L. J. Saethre, S. L. Sorensen and S. Svensson,The Journal of Chemical Physics, 1998. **109**(3): p. 1041-1051.
[27] M. Wiklund, A. Beutler, R. Nyholm and J. N. Andersen,Surface Science, 2000. **461**(1-3): p. 107-117.
[28] M. Wiklund, A. Jaworowski, F. Strisland, A. Beutler, A. Sandell, R. Nyholm, S. L. Sorensen and J. N. Andersen,Surface Science, 1998. **418**(1): p. 210-218.
[29] D. P. Woodruff, T.A. Delchar,1994.
[30] J. Yoshinobu, M. Kawai, S.-I. Tanaka, K. Watanabe, Y. Matsumoto and M. Kamada,Journal of Electron Spectroscopy and Related Phenomena, 1998. **88-91**: p. 665-669.
[31] M. P. Auger,Compt. Rend., 180 (1925), 65; J.de Phys. Radium (1925), 205; Compt. Rend., 182 (1926) 773, 1215.
[32] J. T. Grant, *Surface Analysis by Auger and X-ray Photoelectron Spectroscopy. Chichester: IM Publications*. 2003.
[33] N. Fairley. *www.casaxps.com*.
[34] J. Walton and N. Fairley,Journal of Electron Spectroscopy and Related Phenomena, 2006. **150**(1): p. 15-20.
[35] A. Grob, *Theoretical Surface Science (Springer, Berlin Heidelberg)*. 2003.
[36] P. Hohenberg and W. Kohn,Physical Review, 1964. **136**(3B): p. B864.
[37] W. Kohn and L. J. Sham,Physical Review, 1965. **140**(4A): p. A1133.
[38] J. N. Andersen and C.-O. Almbladh,Journal of Physics: Condensed Matter, 2001. **13**(49): p. 11267-11291.
[39] S. Doniach, M. Sunjic.,J. Phys. C: Solid State Physics, 1970. **3**: p. 285.
[40] D. L. Adams, J. N. Andersen., *FitXPS, Institute of Physics and Astronomy, University of Aarhus, DK.*

3 Experimental

This chapter describes mounting and preparing membrane set-up configuration for hydrogen permeation. In addition to this, the procedures for the different heat treatments performed for hydrogen permeation in our work are presented.

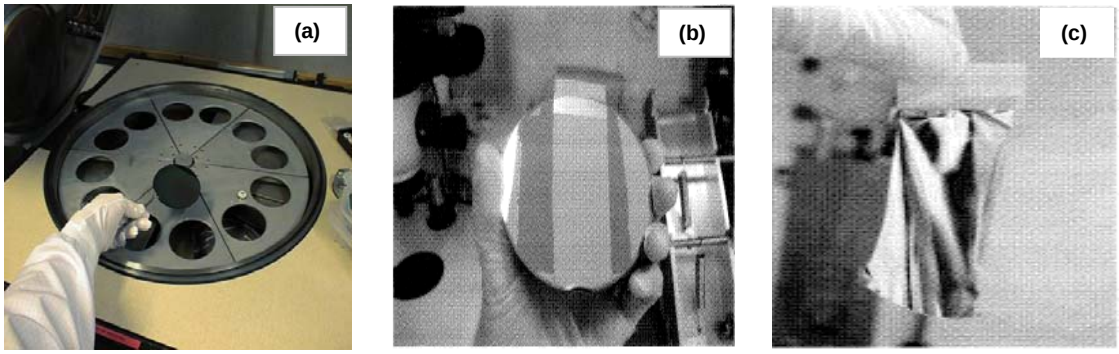

Figure 3.1. Silicon single crystal wafer (a) from the carousel (b) after depositing thin PdAg film growth side is facing opposite to the wafer (c) free standing PdAg film.

3.1 PdAg membranes

As we stated in the previous chapter, PdAg films were prepared by magnetron sputtering. The Fig. 3.1 shows the carousel on the sputtering unit, where the silicon single crystal wafers are mounted for sputtering PdAg thin films. The sputtering procedures and conditions are not the main focus of this thesis and we discuss only the steps from lifting film off the silicon wafer and mounting them on the membrane set-up. The sputtering target is Pd alloys with 23 wt% of Ag which found to be an optimum alloy for membrane materials due to its high hydrogen permeability [1]. As we can see in the Fig. 3.1 (a), at the same sputter run, twelve silicon wafers can be used. Fig. 3.1 (b) shows the membrane ready to be lifting off from the wafer while Fig. 3.1 (c) shows the free standing PdAg thin film.

3.2 Mounting of PdAg thin film in membrane set-up

Fig. 3.2 shows the parts of the membrane set-up schematically. The membrane set-up consists of two tubular stands one with a set of supporting rods. In the membrane set-up the thin film was mounted on a metal plate shown the right side in Fig. 3.2. The metal plates were polished and cleaned in ultrasonic bath with acetone before mounting the thin film. The two membrane set-up stands (shown in left) were also cleaned in an ultrasonic bath. The sample mounting was always performed in the clean room to avoid contaminations on the surfaces of the membranes.

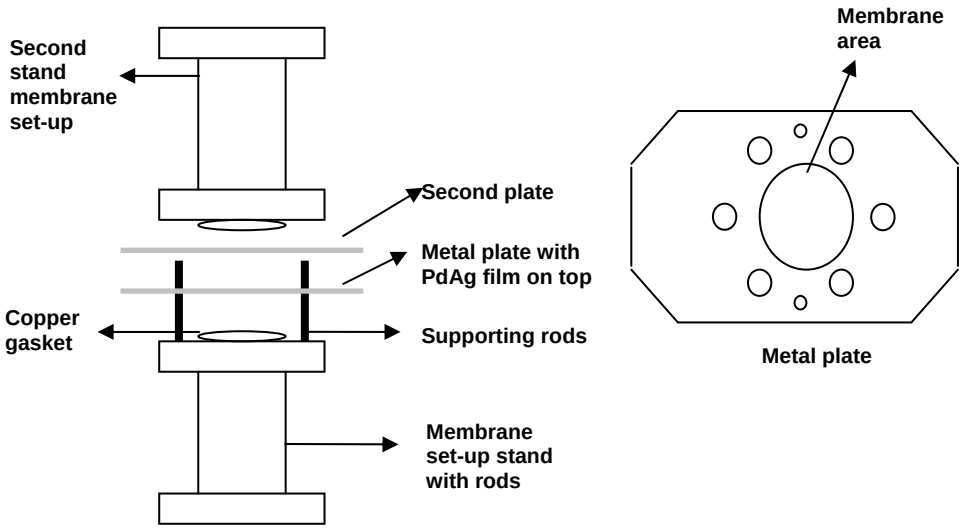

Figure 3.2. Schematic drawing of the membrane set-up parts (left) and the metal plate (right).

The pulled off thin film (Fig. 3.1 (c)) was then mounted on the metal plate, with a few drops of distilled water to enhance the adhesion of the membrane with the plate. A second plate was then mounted on top of the first plate with the PdAg film. These plates together were then placed on the supporting rods of the (bottom) membrane set-up stand. The second piece of the membrane set-up stand (top) was mounted on top and the system was screwed together. The effective area of the film used for hydrogen permeation measurements was 2.0 cm^2.

3.3 Hydrogen permeation measurement

The membrane set-up after the preparation step (Fig. 3.2) was mounted in the hydrogen permeation set-up, a schematics shown schematically in Fig. 3.3. The growth side of the film from sputtering (Fig. 3.1(c)) was always facing the feed side of the system. A thermocouple was connected to the membrane set-up to monitor the temperature of the membrane. The set-up was then covered by furnace housing. The variations in temperature recorded were within ± 2°C.

As can seen in Fig. 3.3, two gas lines were connected to the feed side of the membrane set-up for N_2 and H_2 flow and Ar flow was connected to a third gas line at the permeate side. A mass flow controller (MFC) mounted in the gas lines were used to determine the amount of gas flow in the reactor. A slight overpressure was always maintained at the feed side, and there was no sweep gas used during the pure hydrogen measurements. The permeate side pressure was set equal to the atmospheric pressure. The absolute pressure on the feed side and the differential pressure between feed and permeate sides were recorded. The differential pressure across the membrane was adjusted with a pressure valve. The applied differential pressure limitation was varied depending on membrane thickness.

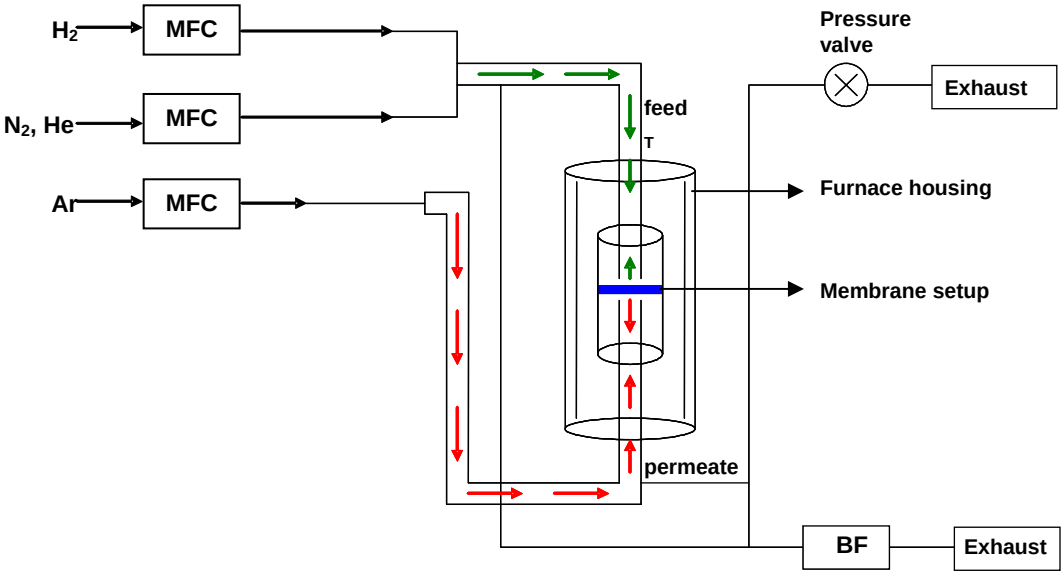

Figure 3.3. Schematics for the hydrogen permeation set-up. MFC refers the mass flow controller that measures the amount of gas flow in the system. BF refers the bubble flow meter used for hydrogen flow measurements.

The permeate side output was connected to a bubble flow (BF) meter. The pure hydrogen flow (will be discussed in chapter 3.3.) was recorded by measuring soap bubble flow in BF. Leakage tests were performed before and after each measurements using H_2 at a flow rate up to 100 ml/min at the maximum differential pressure.

3.4 Heat treatment procedures

Different heat treatment procedures of the Pd-Ag 23 wt% membranes in different gaseous atmospheres were performed. These are presented in Fig. 3.4.

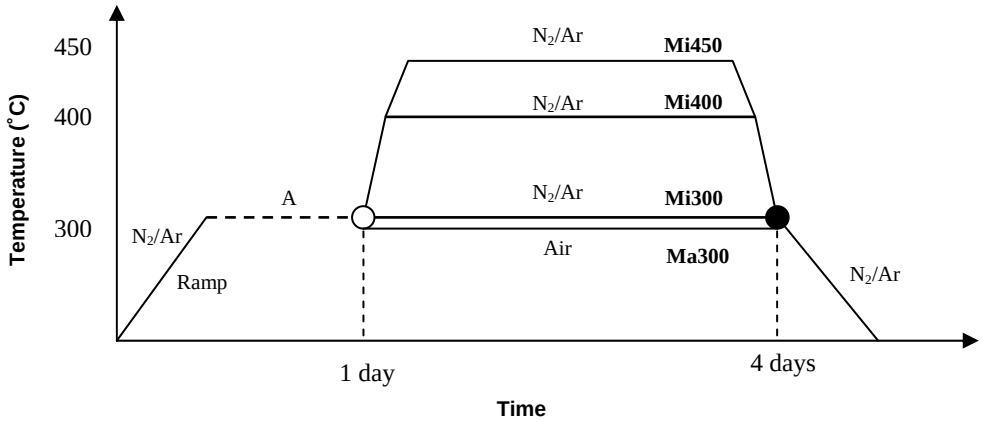

Figure 3.4. Schematics of different heat treatment procedures. Mi300, Mi400, Mi450 and Ma300 refer to the thermal treatments performed (see text for details). The gas exposures are marked as N_2/Ar or Air.

The flow of each gas was calibrated (N_2, Ar, H_2, He) by measuring the flow in the bubble flow meter. Calibration of feed gases was performed by directing the gas outlet at the feed side to the bubble flow meter. The sample code (Mi300, Mi400, Mi450 and Ma300) shown in the Fig. 3.4 are as follows. M refers to the selected membrane, the 'i' in the prefix denotes the thermal treatment in the presumed inert gases nitrogen and argon (will be denoted as N_2/Ar in the following chapters at feed and permeate sides) followed by the corresponding temperature of the treatment. Similarly 'a' represents thermal treatment in air. In addition to this, the other treatment (not shown) will be described below.

3.4.1 Pre-treatment/hydrogen stabilization

The heat treatment procedures included the following steps: The membrane set-up was initially heated to 300°C with N_2 (50 Nml/min, N refers the normal ml/min) at the feed side and Ar (50 Nml/min) at the permeate side. The temperature was ramped at a heating rate of 4°C/min (marked as 'Ramp' in the Fig. 3.2.). At the membrane set-up temperature of 300°C, hydrogen was mixed with the feed gas and the flow of hydrogen through the PdAg membrane was allowed to stabilize. The time required to reach stable hydrogen flow was ~24 hrs. This procedure is called pre-treatment or hydrogen stabilization marked as A in Fig. 3.2. After the pre-treatment N_2 and Ar at the feed and permeate sides respectively were removed slowly. At this step, pure hydrogen flow measurements by monitoring the bubble flow meter were performed marked as an empty circle in Fig. 3.2. The amount of pure H_2 at the feed side was 200 Nml/min for this measurement. As mentioned in chapter 3.2. a range of differential pressures across the membranes was chosen for different thickness membranes (see paper II). At each differential pressure, pure hydrogen flow measurements were carried out. After this step, the flow of hydrogen was decreased slowly and N_2/Ar was reintroduced at the feed/permeate sides to flush out the hydrogen from the system. The duration of the flushing was at least 30 mins. This procedure including pretreatment (A) and hydrogen permeation measurements (called before treatment in papers I and II) was followed by the thermal treatments with different gas exposures as marked in Fig. 3.2.

3.4.2 Air-treatment

The procedure for the air-treatment at 300°C included the following steps. After flushing out hydrogen from the system as described above both feed and permeate sides were exposed to air (either ambient or dry air from a gas bottle). Air exposure at 300°C was maintained for 3.5 to 4 days as indicated in Fig. 3.2. The air at both sides of the membrane was flushed out by slowly introducing N_2 and Ar after the exposure period. This was then followed by pure hydrogen permeation measurements (marked as solid circle and a vertical line) using a bubble flow meter to monitor the flow (after treatment) at selected differential pressures across the membrane. The temperature during permeation measurements was 300°C. After monitoring the flow of pure hydrogen, this gas was flushed out from the system using N_2/Ar. Then the temperature of the set-up was reduced slowly to room temperature at a similar rate (4°C/min) as during initial ramping to elevated temperature.

3.4.3 N_2/Ar thermal treatments

An alternative heat treatment was performed with N_2 at the feed side and Ar at the permeate side of the membrane. N_2/Ar at feed/permeate sides were used for flushing out the hydrogen after permeation measurements as described in chapter 3.4.1. The gas exposure was maintained for 3.5 – 4 days at selected temperatures (300°C, 400°C and 450°C). To reach temperatures above 300°C a heating rate of 4°C/min was applied. After the treatment, N_2/Ar were removed from the system and pure hydrogen was introduced to the feed side. The pure hydrogen flow measurements were always performed at 300°C after all thermal treatments. The temperature was decreased to room temperature with the same cooling rate after permeation measurements (4°C/min).

3.4.4 Oxygen treatment

In addition to the above thermal treatments, another heat treatment was performed with pure oxygen flow on both the feed and permeate sides (50 Nml/min) of the membrane. The pre-treatment (A) and the follow up procedures were similar to the air-treatment, but the gas exposure was with pure oxygen. The pure hydrogen measurements after the thermal treatment were not carried out for this membrane. The membrane was cooled down to room temperature with N_2/Ar exposure at the feed/permeate sides. The purpose of this experiment was to determine the effect of treatment in oxygen at elevated temperature (300°C) on the membrane surface topography and chemical composition (paper II).

3.4.5 Pre-treatment and cooling in hydrogen

To address the influence of hydrogen on the surface chemical composition two 2 µm membranes were taken through the pre-treatment procedure (A) and subsequent hydrogen permeation measurements. Afterward the membranes were cooled down to room temperature in hydrogen atmosphere. One of them was cooled down immediately to room temperature by opening the housing surrounding the membrane set-up. The other membrane was cooled down in hydrogen with cooling rate 4°C/min after the pre-treatment (A). (see paper II) The surface segregation analysis was performed on these films and the results are presented in paper II.

The hydrogen flux measurements from these different treatments on different thickness PdAg membranes are reported [2, 3]. Further detailed study of surface (paper II) and bulk microstructure [4] characterization were performed and reported.

3.5 References

[1] S. Uemiya, T. Matsuda, and E. Kikuchi,Journal of Membrane Science, 1991. **56**(3): p. 315-325.

[2] A.L. Mejdell, H. Klette, A. Ramachandran, A. Borg, and R. Bredesen,Journal of Membrane Science, 2008. **307**(1): p. 96-104.

[3] W.M. Tucho, H.J. Venvik, M. Stange, J.C. Walmsley, R. Holmestad, R.Bredesen,Manuscript in preparation. , 2009.

[4] W.M. Tucho, J.C. Walmsley, M. Stange, A. Ramachandran, H.J. Venvik, R.H. Mathiesen, A. Borg, R. Bredesen and R. Holmestad, Manuscript in preparation. 2009.

4 Summary of papers

This chapter summarizes the papers presented in the second part of this thesis. Paper I-III are results from the work based on PdAg membranes. Paper IV and V present the investigation performed on Pd(110) based model systems.

Paper I *Hydrogen permeation of thin, free-standing Pd/Ag23% membranes before and after heat treatment in air.*

Thin free standing Pd/Ag23wt% membranes with five thicknesses ranging from ~1.3 to ~5.0 μm were prepared by magnetron sputtering and thermally treated in air at 300°C. The hydrogen permeation measurements were performed before and after a thermal treatment. For all membranes studied, the thermal treatment resulted in enhanced permeation, and for some membranes, the hydrogen flux more than doubled. A permeance of 1.7 x 10^{-2} mol/m^2 s $Pa^{0.5}$ was observed for ~1.3 μm thick membranes, which is one of the highest reported. Bulk diffusion was found to be the main rate-limiting step after thermal treatment in air. The permeability was quite similar for all membranes studied after this treatment, with a mean value of 2.1 x 10^{-8} ± 5 x 10^{-10} mol/m^2 s $Pa^{0.5}$. Surface topography studies by atomic force microscopy showed increase in surface area and surface grains for the samples thermally treated in air compared to the as-grown membranes. An alternative thermal treatment in N_2 and Ar in feed and permeate sides (N_2/Ar) at 400°C on one membrane (1.5 μm) found similar hydrogen permeation after thermal treatment in air. Investigations on topography analysis on this sample were also found increase in surface roughness and surface area compared to the as-grown membrane.

Paper II Surface *characterization of thin Pd/Ag 23 wt% membranes after different thermal treatments*.

The investigations from paper I on thin membranes (1.5 μm) resulting similar flux in N_2 and Ar presumed inert gas atmospheres motivated the study of the alternative N_2/Ar treatment in detail. To gain further insight of this treatment we chose three different treatment temperatures (300°C, 400°C, 450°C). For a 2 μm membranes the thermal treatments in N_2/Ar at all selected temperatures enhanced the hydrogen flux. Differently the same treatments for the thicker membranes caused a decrease in hydrogen flux, except for the 5μm membrane thermally treated at 450˚C. Accompanying changes in the surface topography and chemical composition were subsequently investigated by atomic force microscopy (AFM), X-ray photoelectron spectroscopy (XPS) and Auger Electron Spectroscopy (AES) depth profiling. For a 2 μm thick membranes the surface roughness and area increase for all N_2/Ar annealing temperatures applied, while a temperature of 450°C was required for an increase in roughness of both membrane surfaces to occur for a 5 μm membrane. The thickest membrane, of 10 μm, showed change in the surface roughness and area on one side of the membrane only and a slight decrease in hydrogen permeance after all heat treatments in N_2/Ar. XPS investigations performed after

treatment and subsequent permeation measurements reveal segregation of silver to the membrane surfaces for all annealing temperatures applied. For all selected membranes, heat treatment at 300°C in air gave higher hydrogen permeance accompanied by increasing surface roughness and area as well as different segregation behavior at the membrane surfaces. The available data point at bulk limited hydrogen permeation for Pd/Ag membranes after heat treatment in air at 300°C for thicknesses down to 1.5-2.0 μm. A transition from surface to bulk control upon treatment is feasible, at least for the thinner membranes, but the changes in permeance can not be fully accounted for by the observed changes in surface structure and composition.

Paper III *Thin Pd-23%Ag/stainless steel composite membranes: Long-term stability, life-time estimation and post-process characterisation.*

Thin 2.6 μm thick PdAg membrane was mounted on a 4 cm long tubular macroporous stainless steel substrate. The long-term stability of the selected membrane has been examined in H_2/N_2 mixtures as a function of both temperature and feed pressure. During continuous operation, the membrane showed a good stability at 400°C while the N_2 leakage increased very slowly at a temperature of 450°C (P_{feed} = 10bar). After 100 days of operation (P_{feed} = 5-20bar, T=350-450°C), the N_2 permeance was 7.0 x 10^{-9} mol $m^{-2}s^{-1}Pa^{-1}$, which indicates that the H_2/N_2 permselectivity still lies around 500, based on a H_2 permeance equal to 3.0 x 10^{-6} mol $m^{-2}s^{-1}Pa^{-1}$. Despite the generation of small pinholes, a membrane life-time of several (2-3) years (T≤425°C) was estimated for the experimental conditions employed based on long-term stability tests over 100 days. Post-process characterization showed a considerable grain growth and micro-strain relaxation in the Pd-23%Ag membrane after the prolonged permeation experiment. Changes in surface area were relatively small. In addition, segregation of Ag to the membrane surfaces was observed. The formation of pinholes is identified as the main source of the increased N_2 leakage during testing at higher temperature.

Paper IV *Methanol Adsorption on Pd(110) and Ag/Pd(110) studied by High Resolution Photoelectron Spectroscopy*

As an example of the complex issue in real membranes, PdAg membranes exposed on methanol steam reforming conditions were found to be decrease in hydrogen flux [see refs 17 and 71 in chapter 1]. Possible causes suggested were carbonaceous species and unconverted methanol on the membrane surface. For this reason, it is important to understand the adsorption behaviour of Pd/Ag alloys. We addressed this issue in the present paper by studying the adsorption behaviour of methanol on Pd(110) and Ag/Pd(110) by high resolution photoelectron spectroscopy. On Pd(110) two different methanol species were observed upon adsorption at 100K and subsequent heating up on 200K. The species with lowest C1s core level binding energy was remaining at the surface for low methanol coverage. The adsorption and decomposition behavior of methanol on a Ag/Pd(110) surface alloy formed by depositing Ag on Pd(110) at elevated temperature was similar to that of the pure Pd(110) surface, a finding showing

that the amount of Ag present in the surface in this study did not affect the decomposition behavior of methanol as compare to pure Pd(110).

Paper V *Adsorption and decomposition of methylamine on Pd(110) studied by high resolution photoelectron spectroscopy and DFT calculations*

As a different application, amines were found to be promising candidates for CO_2 capturing. We performed adsorption and decomposition of methylamine on Pd(110) by high resolution photoelectron spectroscopy. Methylamine was observed to adsorb molecularly at the Pd(110) surface at low temperatures (120 K). In the temperature range 300-350 K CN species were observed formed at the surface and methylamine desorbing from the surface. CN remains on the surface up to an annealing temperature of 800 K. The theoretical calculations predict a methylamine on-top adsorption site on Pd(110) with an adsorption energy of 0.40 eV. As seen for other systems methylamine is found to bind to the surface via a lone pair on the N atom. The CN molecule is lying down on surface with the C–N axis along the [001] direction above a second layer Pd atom. The adsorption structure found for CN is in agreement with quantitative structural determinations performed by another group. The binding energy shift between methylamine and cyanide in the C 1s and N 1s states are also calculated. These values are in good agreement with the experimental findings.

5 Suggestions for further work

Some suggestions for further work related to the research work presented in this thesis are described here.

From the hydrogen permeation behaviour on PdAg membranes after different gaseous exposures, the segregation was found to be an interesting feature that may be of importance hydrogen permeation behaviour of a membrane (see paper IV). For 2 and 5 μm membranes after air-treatment at 300˚C segregation of Pd to the surface. In addition, there is a strong Pd enrichment for the 2 μm PdAg membrane exposed in pure oxygen at 300˚C. The segregation behaviour in PdAg membrane system is not fully understood from the present work. A systematic investigation of segregation behaviour at different temperatures and in various atmospheres both for thin membranes as well as PdAg model systems is suggested.

Also hydrogen induced segregation is of interest for PdAg membranes due to stronger adsorption of hydrogen on palladium. There are a few experiment and theoretical studies of segregation due to hydrogen [1, 2]. Interestingly DFT calculations showed reverse segregation on the Pd-Ag alloy surfaces [2]. In our experimental results after the hydrogen stabilization (see paper II) the membrane were cooled down in hydrogen. Two different cooling rates were chosen (see paper II). Both procedures result Ag enriched on the surface. Therefore, it would also be interesting to get deeper insight on hydrogen induced enrichments on Pd-Ag bimetallic systems.

The adsorption and decomposition of methanol interactions on Pd(110) and Ag/Pd(110) studies (paper IV) showed the intermediate species formed during the dehydrogenation reactions. The formation of methoxy intermediate species is not clear from the present work. Studying the co-adsorption behaviour of methanol reforming gases or water gas shift gases on PdAg model systems may give furthermore informations of the intermediates and their reactions with Pd and Ag. PdCu membranes are also of interest in hydrogen permeation due to its high sulfur resistant behaviour. Systematic studies of different gas atmospheres on PdCu model systems would also provide information on segregation behaviour.

The alloying of Ag/Pd is another interesting factor that needs more quantified structural analysis. The STM study for deposition of different Ag coverage on Pd(110) surface would give some basic idea of surface structures of Ag at different temperatures.

[1] J. Shu, B.E.W. Bongondo, B.P.A. Grandjean, A. Adnot, and S. Kaliaguine,Surface Science, 1993. **291**(1-2): p. 129-138.
[2] O.M. Løvvik and S.M. Opalka,Surface Science, 2008. **602**(17): p. 2840-2844.

Paper I

Hydrogen permeation of thin, free-standing Pd/Ag23% membranes before and after heat treatment in air

A.L. Mejdell, H. Klette, A. Ramachandran, A. Borg, and R. Bredesen

Journal of Membrane Science, 307 (2008) 96

Available online at www.sciencedirect.com
ScienceDirect
Journal of Membrane Science 307 (2008) 96–104
journal of MEMBRANE SCIENCE
www.elsevier.com/locate/memsci

Hydrogen permeation of thin, free-standing Pd/Ag23% membranes before and after heat treatment in air

A.L. Mejdell [a,c,*], H. Klette [b], A. Ramachandran [c], A. Borg [c], R. Bredesen [b]

[a] *Department of Chemical Engineering, NTNU, 7491 Trondheim, Norway*
[b] *SINTEF Materials and Chemistry, 0314 Oslo, Norway*
[c] *Department of Physics, NTNU, 7491 Trondheim, Norway*

Received 1 February 2007; received in revised form 7 September 2007; accepted 12 September 2007
Available online 21 September 2007

Abstract

Free-standing Pd/Ag23 wt% membranes with five different thicknesses ranging from ~1.3 to ~5.0 μm were prepared by magnetron sputtering. The hydrogen permeation was determined before and after a thermal treatment in air at 300 °C. For all membranes studied, the thermal treatment resulted in enhanced permeation, and for some membranes, the hydrogen flux more than doubled. A permeance of 1.7×10^{-2} mol/m^2 s Pa$^{0.5}$ was observed for ~1.3 μm thick membranes, which is one of the highest reported. Bulk diffusion was found to be the main rate-limiting step after thermal treatment in air. The permeability was quite similar for all membranes studied after this treatment, with a mean value of $2.1 \times 10^{-8} \pm 5 \times 10^{-10}$ mol m/m^2 s Pa$^{0.5}$. Topography studies by atomic force microscopy showed that the samples thermally treated in air had higher surface roughness, larger surface area and larger surface grains than samples not heat-treated in air.

Keywords: Palladium; Silver; Hydrogen permeation; Thin films; Treatment in air

1. Introduction

Hydrogen is one of the most important chemical commodities and is used in many industry sectors. The demand for hydrogen in petrochemical industry and in power generation is expected to grow. Sustainable large-scale production of hydrogen from fossil sources will require technology for carbon dioxide capture. Membranes, particularly palladium-based membranes, are investigated for this application along with a number of other small-scale applications for production and purification of hydrogen. Palladium has high hydrogen permeability, and is essentially non-permeable to other gases, making the material suitable for hydrogen separation membranes. A problem, however, is the high material costs, which necessitate development of composite membranes consisting of a thin palladium or palladium alloy membrane layer on a cheap, mechanically strong support. Thin membranes are also advantageous in terms of hydrogen flux, which contributes importantly to the total cost reduction for the membrane process.

The hydrogen permeability has been found to increase when palladium is alloyed with silver [1,2], and a maximum in permeability is found for silver contents around 23% [1]. Additionally, palladium–silver alloys exhibit improved mechanical properties as compared to pure palladium [1,3–5].

A general expression for the hydrogen flux (mol/m^2 s) through a membrane, J, may be written [6,7]:

$$J = \frac{P}{t}(p_1^n - p_2^n) \quad (1)$$

where P is the permeability, t is the membrane thickness and p_1 and p_2 are the hydrogen partial pressures in the gas phase on the high and low pressure sides of the membrane, respectively. The value P/t is termed the membrane permeance and is often reported when membrane thickness cannot be given with sufficient accuracy. The n-value depends on the rate-limiting steps in the permeation process. As long as bulk diffusion is the rate-limiting step, the n-value will be approximately equal to 0.5

* Corresponding author at: Department of Chemical Engineering, NTNU, 7491 Trondheim, Norway. Tel.: +47 97669763; fax: +47 73594080.
E-mail address: astridm@chemeng.ntnu.no (A.L. Mejdell).

0376-7388/$ – see front matter © 2007 Elsevier B.V. All rights reserved.
doi:10.1016/j.memsci.2007.09.024

[6–9]. At sufficiently reduced thicknesses, other processes may control the hydrogen permeation, which typically results in the observed *n*-value approaching 1 [6–9]. In the latter case, surface reaction rates or gas phase diffusion may be rate-controlling processes. Additionally, for thin membranes an *n*-value even higher than 1 has been reported [6].

A modelling study has concluded that bulk diffusion is expected to be the main rate-controlling step for pure palladium membrane thicknesses down to 1 μm for temperatures above ∼300 °C, provided that external mass transfer resistance is absent [10]. Experimentally, with hydrogen only used as feed gas, bulk diffusion has been reported as rate-limiting for 1 μm thick composite palladium membranes [8]. Other researchers have, however, reported that surface reaction rate limitation becomes important already at higher thicknesses, up to several micrometers [7,11]. The membranes investigated in the present work are between 1 and 5 μm, and thus in a thickness range where previous reports on composite membranes are inconsistent concerning the nature of the rate-limiting step.

Thermal treatment in air, where the membrane is oxidized and subsequently reduced, has shown to be beneficial, resulting in higher hydrogen flux [12–14]. Several researchers have used thermal treatment in air on fresh membranes to remove poisoning species [2,15], but also to recover deactivated membranes after operation [14,15]. Increased surface roughness, and thus an increased number of active sites for hydrogen dissociation, has been observed after thermal treatment in air [14,16,17]. However, it has been suggested that increased surface area alone is insufficient to explain the increase in hydrogen permeation [14]. It has also been shown that oxidation time and temperature can influence the permeation improvement and extent of defect formation following the oxygen treatment [13].

Composite membranes are typically made by deposition of the metal layer directly onto a porous support by various deposition techniques [18]. The pore size and distribution in the support surface determine the required metal layer thickness for obtaining a flawless membrane. A ratio LP = (separation layer thickness)/(support layer pore size) may be defined, and this is typically of the order 100 or higher [19]. In general, low LP is advantageous for the hydrogen permeation. Free-standing membranes, corresponding to LP = 0, have been fabricated by several researchers [6,20–22] and such membranes provide an excellent opportunity to investigate the membrane properties without having to take into account additional effects due to the presence of a mechanical support. A novel method enables fabrication of thin free-standing membranes by the magnetron sputtering technique [23]. The membranes are sputtered on, and subsequently lifted off, polished silicon wafers, a technique which provides highly homogenous films. These free-standing membranes may also be used to fabricate composite membranes in a two stage process, giving LP < 1 [24], a value much less than typically achieved by conventional preparation methods. In the present work, the hydrogen permeation properties of thin free-standing membranes are studied. Particularly, we have investigated the effect of heat treatment in air at 300 °C on 1–5 μm thick foils with composition Pd/Ag23 wt%.

2. Experimental

Palladium–silver membranes were produced by dc magnetron sputtering (CVC 601 sputtering apparatus) using argon as the sputter gas (purity 99.999%). The membranes were sputtered from a Pd/Ag23% target onto polished silicon single crystal substrates. Sputtering was performed from 80 to 360 min, with sputtering rates ranging from ∼0.014 to ∼0.017 μm/min. A pre-sputtering procedure was performed in order to achieve stable sputtering conditions, and also to clean the target surface. During sputtering, the silicon wafers were placed on a carousel, rotating with constant speed, so that nearly equal growth rate and composition are expected for membranes produced in the same

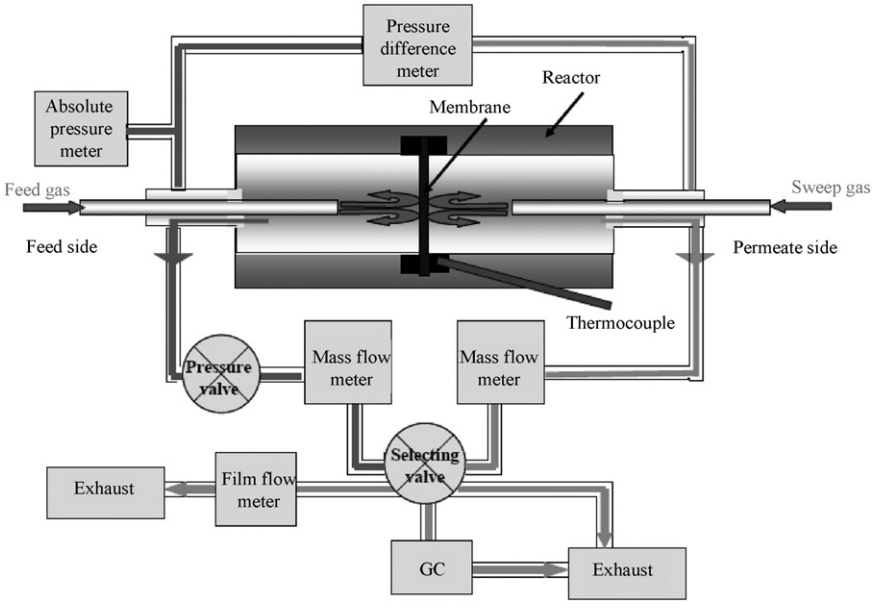

Fig. 1. The flux measurement setup.

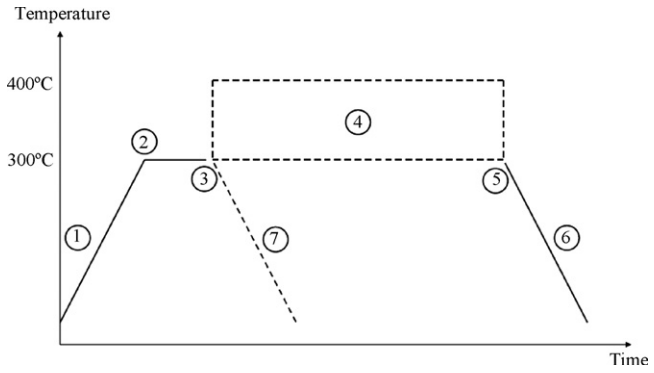

Fig. 2. Applied temperatures as a function of time.

sputtering run, i.e. for membranes in the same thickness category in the present study. After sputtering, the final membrane thickness was determined by scanning electron microscopy or white light interferometry. Based on thickness measurements at various positions on the silicon wafer, we have estimated the thickness variations to be approximately ±0.1 μm among membranes from the same sputtering run or thickness category. The testing was carried out on 5 different membrane thicknesses, ∼1.3 μm (thickness category A), ∼1.7 μm (thickness category B), ∼2.2 μm (thickness category C), ∼5.0 μm (thickness category D) and ∼1.5 μm (thickness category E).

The free-standing membrane was mounted between two stainless steel plates with a circular hole with area 2.4 cm^2, which corresponds to the active membrane surface area during the permeation measurements. The plates with the fixed membrane were placed in a stainless steel housing connected to the gas system. Sealing was achieved by placing copper gaskets between the steel plates and the housing. A schematic drawing of the flow measurement setup is shown in Fig. 1.

In Fig. 2, a summary of the applied temperatures as a function of time during testing is illustrated. The different feed and sweep gas compositions are summarized in Table 1. Steps 1, 2 and 3 are equal for all experiments. The membrane was ramped to 300 °C, flushing with nitrogen (purity 99.999%) on the feed side and argon (purity 99.999%) on the permeate side (step 1). After ramping to 300 °C, a pre-treatment was carried out by mixing hydrogen into the feed gas and leaving the hydrogen permeation to steadily increase and then stabilize; a process taking ∼24 h. The hydrogen permeation measurements (steps 3 and 5) were performed at 300 °C before and after a treatment period. During permeation measurements, the feed gas was hydrogen

Table 1
Feed and sweep gas compositions used during the different testing steps

Step	Flow (ml/min)		
	Feed		Permeate
	H_2	N_2	Ar
1, 6, 7	–	100	100
2	100	100	100
3, 5	200	–	–
4	Treatment period		

Table 2
Feed and sweep gas compositions used during the different treatments (step 4)

Treatment	Temperature (°C)	Period (days)	Flow (ml/min)				
			Feed			Permeate	
			H_2	N_2	Air	Ar	Air
In air	300	3.5–4	–	–	×	–	×
In H_2	300	3.5–4	100	100	–	100	–
In N_2/Ar	400	3.5–4	–	100	–	100	–

only (purity 99.995%). A flow meter (HORIBA group, model SF-2) was used to determine the hydrogen flow through the membrane. The hydrogen flow was measured as a function of the hydrogen differential pressure across the membrane, which was varied from ∼20 kPa down to ∼6 kPa. The permeate side was kept at atmospheric pressure.

All membranes were leak checked with helium before ramping to 300 °C, and with nitrogen, added to the hydrogen in the feed gas, in between measurements with hydrogen only. The helium and nitrogen leakages were measured with a gas chromatograph (Agilent Technologies, model Quad Series: Micro GC). For all membranes investigated, the separation factor, α_{H_2/N_2}, was found to be >500 throughout the experiments, where the separation factor is defined as $\alpha_{H_2/N_2} = (y_{H_2}/y_{N_2})/(x_{H_2}/x_{N_2})$, and the y's and x's are the concentrations on the permeate and feed side, respectively.

Step 4 represents the treatment period. The feed and sweep gas compositions during different treatments are summarized in Table 2. The procedure of thermal treatment in air was carried out as follows: The system was flushed with nitrogen and argon, before all gases were turned off. The thermocouples at both sides of the reactor were removed to allow air into the system. The system was kept like this, at 300 °C, for 3.5–4 days. The thermocouples were then reinstalled, the system was flushed with nitrogen and argon and an "after heat treatment in air" measurement series was carried out.

In addition, two other treatments were also carried out on the category E membranes. One membrane was exposed to a hydrogen mixture at 300 °C for the treatment period. In the other treatment, the temperature was raised to 400 °C, and the membrane was left in nitrogen and argon for the same period of time. After treatment, all membranes were permeation tested in hydrogen only at 300 °C (step 5), and the system was then cooled down to room temperature in nitrogen and argon (step 6).

To study how the different steps in the testing procedure affected the surface topography of the membranes, some of the membranes were examined by atomic force microscopy (AFM). A MultiMode SPM from Digital Instruments was used in Tapping Mode, and analysing tools provided by the instrument software were used to estimate the root mean square roughness, surface areas and grain sizes. As-grown samples were examined after they were lifted off the silicon wafer. Furthermore, a set of membranes was prepared, which was exposed to hydrogen until stabilization and tested in hydrogen only, but not heat-treated further (henceforth denoted "tested but not further

treated"). This means that the testing procedure went directly from step 3 to step 7 in Fig. 2. Finally, heat-treated samples were investigated. All thickness categories were included in the study, and several different areas (about 10) were investigated on each sample.

3. Results and discussion

Fig. 3 shows the hydrogen flux as a function of the difference in the square root of the pressures, measured before (Fig. 3a) and after (Fig. 3b) heat treatment in air (steps 3 and 5 in Fig. 2, respectively). A plot using $n = 1/2$ rather than $n = 1$ is chosen, because bulk diffusion is believed to be the most dominant step, at least after heat treatment in air, as will be discussed below. Before thermal treatment in air, the flux at $(p_1^{1/2} - p_2^{1/2}) \sim 30$ kPa, ranges from $\sim$0.084 mol/m^2 s (thickness $\sim$5.0 μm) to $\sim$0.27 mol/m^2 s (thickness $\sim$1.7 μm), with increasing rate for decreasing membrane thickness as a general tendency. For all membranes studied, the thermal treatment in air results in enhanced permeation, with the flux ranging from $\sim$0.12 mol/m^2 s (thickness $\sim$5.0 μm) to $\sim$0.53 mol/m^2 s (thickness $\sim$1.3 μm) at $(p_1^{1/2} - p_2^{1/2}) \sim 30$ kPa.

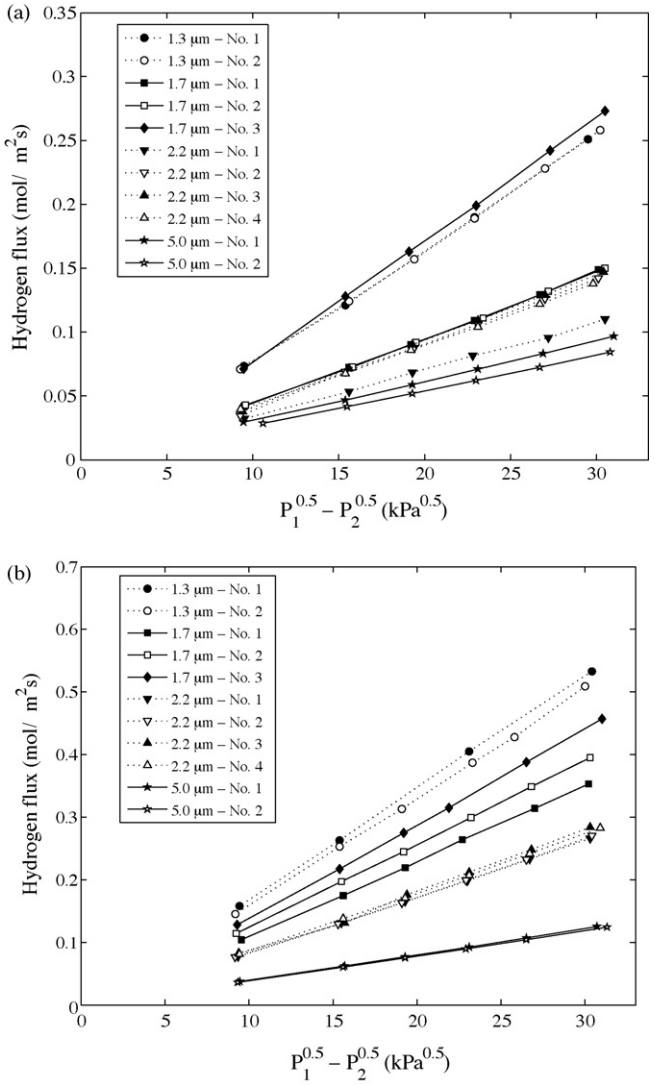

Fig. 3. Hydrogen flux through the membranes as a function of the difference in the square root of the hydrogen partial pressures, (a) before and (b) after heat treatment in air. Straight lines are guidance for the eye.

Before heat treatment in air, some variation in hydrogen flux within a given thickness category is found, and furthermore, different categories overlap to some extent. As can be seen from Fig. 3a, one of the $\sim$1.7 μm thick membranes shows higher flux than the $\sim$1.3 μm thick membranes, while the other two are close to the values observed for two of the $\sim$2.2 μm thick membranes. Also noteworthy, despite the relatively large thickness difference, the $\sim$5.0 μm thick membranes and one of the $\sim$2.2 μm thick membranes show fairly similar permeation. These variations are far too large to be explained exclusively by the uncertainty in the thickness estimations. The thermal treatment in air results both in enhanced hydrogen permeation and more distinct separation between the different thickness categories. It should be noted that the membranes prior to testing were stored for different lengths of time after fabrication, which may have affected the surface cleanliness and the corresponding permeation results within the same thickness categories. As have been reported by others, thermal treatment in air has been used to remove poisoning species from fresh membranes [2,15]. However, no correlation is observed between length of storage and flux value.

A question arising is whether or not the enhanced permeation is solely a result of the membrane being left at high temperature over an extended period of time, or if the increase can actually be attributed to the exposure to air. In an attempt to shed light on these aspects, the category E membranes were given different heat treatments. As shown in Fig. 4, heat treat-

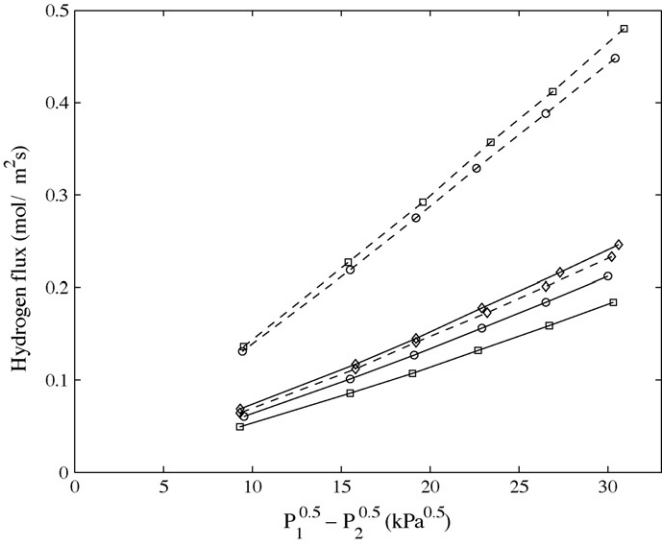

Fig. 4. Hydrogen flux through the membranes as a function of the difference in the square root of the hydrogen partial pressures for different treatments of category E membranes. (◯) The membrane which was heat-treated in air at 300 °C, (□) the membrane which was heat-treated in nitrogen and argon at 400 °C and (◇) the membrane which was exposed to hydrogen at 300 °C for an extended period of time. The straight lines are guidance for the eye. Solid lines indicate the results before the treatments, while the dashed lines indicate the results after the treatments.

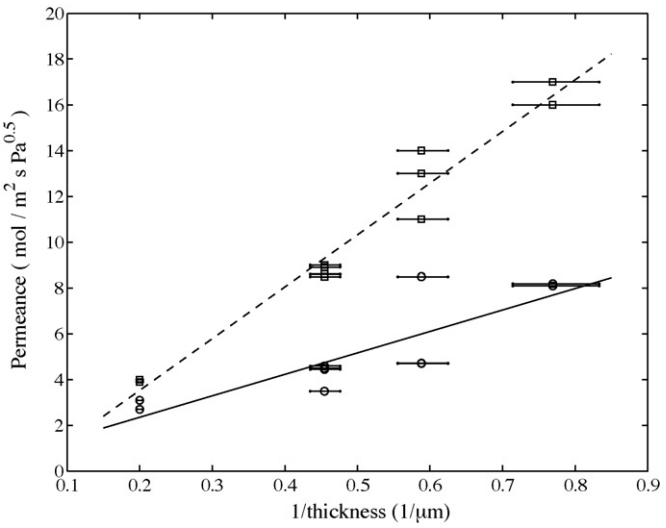

Fig. 5. Permeance versus the inverse membrane thickness. (◯) Results before thermal treatment in air and (□) after treatment. Also plotted are regression lines fitted to all data, solid for before thermal treatment and dashed for after treatment.

ment in air at 300 °C results in significantly enhanced hydrogen permeation. On the other hand, the membrane, which was heat-treated in hydrogen at 300 °C over the same period of time (3.5–4 days), shows a slight decrease in hydrogen flux during testing. The heat treatment in nitrogen and argon at 400 °C, however, gives an almost identical result to the heat treatment in air at 300 °C. These results show that the enhancement in flux is critically dependent on both temperature and ambient atmosphere.

To gain further insight, we have analysed our data to elucidate the type of the rate-limiting step. The most common way to determine the rate-controlling steps is to estimate the n-value, from fitting the experimental data J versus $(p_1^n - p_2^n)$ in Eq. (1). However, for the small pressure range applied in this study, such an analysis does not give an unambiguous value of n. Nearly straight lines are observed, both with $n = 1/2$ and with $n = 1$. Even though the burst pressure of the thinner membranes is as high as ∼80 kPa, some plastic deformation occurs already at lower pressures. To avoid significant interpretation problems related to change in membrane area and thickness, we have restricted our measurements to differential pressures up to ∼20 kPa, and are therefore not able to determine the n-value directly from these experiments.

For membranes of equal composition and with equal microstructure, the permeability should be a material constant which is independent of thickness. As long as bulk diffusion is the rate-limiting step, a linear relationship is expected between the permeance and the inverse membrane thickness. In Fig. 5, the permeance versus the inverse membrane thickness is plotted, together with a regression line fitted to all data. The results before thermal treatment in air appear to have a weak tendency of increasing permeance with decreasing thickness. After heat treatment in air the measurements are closer to a fitted regression line. Even though the n-values cannot be determined, these plots indicate that bulk diffusion is the main rate-limiting step for the membranes after heat treatment in air, while also other processes influence the permeation rate more importantly prior to the treatment.

Permeance and permeability values calculated from our experimental data may give further understanding of the limiting factors discussed above. The values for the most and least permeable samples in thickness categories A–D are listed in Table 3. As already mentioned, the permeability should be independent of thickness, as long as bulk diffusion is rate controlling. The thermal treatment in air clearly results in reduced scatter in permeability, giving a mean value $2.1 \times 10^{-8} \pm 5 \times 10^{-10}$ mol m/m^2 s Pa$^{0.5}$. This finding thus supports that bulk diffusion is the main rate-controlling step after the treatment, and furthermore, that the material transport properties are fairly similar and independent of the membrane thickness. A decrease in the permeability value will be expected when other processes than bulk diffusion become more dominant. From Table 3, it is seen that the permeability values for thickness categories A–C are clearly lower than for category D before thermal treatment in air, with one exception (sample 3(B)). A possible explanation to this is that the A–C categories membranes are more limited by surface processes than the thicker ones. Furthermore, it is seen that the permeability clearly varies within the B and C categories, corresponding to variation in hydrogen flux, and that the thinner membranes not necessarily have the lowest value. This variation in permeation property could indicate that the membranes

Table 3
Calculated permeances and permeabilities, before and after heat treatment in air for selected membranes

Thickness (μm)	Sample (category)	Before		After		Improvement
		Permeance (mol/m^2 s Pa$^{0.5}$)	Permeability (mol m/m^2 s Pa$^{0.5}$)	Permeance (mol/m^2 s Pa$^{0.5}$)	Permeability (mol m/m^2 s Pa$^{0.5}$)	
∼1.3	1 (A)	8.1×10^{-3}	1.1×10^{-8}	1.7×10^{-2}	2.2×10^{-8}	2.1
∼1.3	2 (A)	8.2×10^{-3}	1.1×10^{-8}	1.7×10^{-2}	2.2×10^{-8}	2.1
∼1.7	1 (B)	4.7×10^{-3}	8.0×10^{-9}	1.1×10^{-2}	1.9×10^{-8}	2.3
∼1.7	3 (B)	8.5×10^{-3}	1.4×10^{-8}	1.4×10^{-2}	2.4×10^{-8}	1.6
∼2.2	1 (C)	3.5×10^{-3}	7.7×10^{-9}	8.6×10^{-3}	1.9×10^{-8}	2.5
∼2.2	3 (C)	4.7×10^{-3}	1.0×10^{-8}	9.2×10^{-3}	2.0×10^{-8}	2.0
∼5.0	1 (D)	3.1×10^{-3}	1.6×10^{-8}	4.0×10^{-3}	2.0×10^{-8}	1.3
∼5.0	2 (D)	2.7×10^{-3}	1.4×10^{-8}	3.9×10^{-3}	2.0×10^{-8}	1.4
>20	Refs. [2,25]		$\sim 1.5 \times 10^{-8}$			

are limited by other factors than bulk diffusion to different extents.

In the bottom row of Table 3, the bulk permeability values for two thick membranes are listed for comparison. Both Itoh et al. [2] and Yang et al. [25] have reported a permeability of $\sim 1.5 \times 10^{-8}$ mol m/m^2 s Pa$^{0.5}$ for a 100 μm thick Pd/Ag23 wt% membrane and a 20 μm thick Pd/Ag20 wt% membrane, respectively. For these membranes, where only hydrogen was used as feed gas during the permeability tests, bulk diffusion was found to be the rate-determining step. The permeability values are fairly consistent with the ones obtained for our category D membranes, suggesting that the category D membranes are more similar to bulk materials before the treatment than the thinner ones. After heat treatment in air, all membranes in the present study have permeability values, which exceed those reported for the bulk membranes. One may thus speculate whether the heat treatment in air procedure changes the microstructure and composition of the films, creating membranes with higher permeability.

In the last column of Table 3, the enhancement achieved by thermal treatment in air is given. For the thickness categories A–C, approximately a doubling in the hydrogen permeance/permeability is observed. A permeance reaching $\sim 1.7 \times 10^{-2}$ mol/m^2 s Pa$^{0.5}$ is found for category A membranes. Since the separation factor, α_{H_2/N_2} is higher than 500 for all membranes studied, this value represents one of the highest permeance values reported for a highly selective membrane. For the category D membranes, the enhancement is smaller (30–40%), which demonstrates that the effect of the thermal treatment depends on membrane thickness.

It should be noted that the high permeance values found in this work are partly due to the elimination of a supporting structure. We have elsewhere reported measurements on similar thin membrane foils, supported on porous stainless steel with 2 μm pore size [26]. A comparison with these studies shows that even with $L < 1$, the support imposes a noticeable resistance to the hydrogen flux. As mentioned previously, free-standing membranes have been fabricated by several researchers [6,20–22]. However, in the permeation studies reported, hydrogen has been used in a mixture with other gases [6,20,22]. Because of differences in both feed gas composition and temperature range, a direct comparison of our results with studies on other free-standing membranes is difficult. In a separate study, using a mixture of hydrogen and nitrogen on the feed side, we have observed a significant reduction in hydrogen permeation, which is larger than what would be expected from the reduction in bulk gas hydrogen concentration alone [27]. We suggest that the large reduction is due to a concentration polarization effect, resulting in nitrogen enrichment adjacent to the membrane surface at the feed side and thus a lowering of the hydrogen differential pressure across the membrane. In the present study, all permeation tests were performed with only hydrogen in the system, providing results, which are not influenced by a mechanical support or possible concentration polarization effects.

In order to study how the different treatments affected the surface topography, some of the membranes were examined by AFM. In Fig. 6, representative AFM images for ~1.3 μm thick membranes are shown, both an as-grown sample, a sample, which was tested but not further treated, and a sample heat-treated in air. The topographical values are listed in Table 4. Calculations of these values are based on a series of AFM images, taken from about 10 different locations on each sample. The rms value is a measure of surface roughness. Also given are the area of the surfaces imaged, the average grain diameter and the density of grains in the image. Both sides of the membranes were examined, that is, both the surface facing the high-pressure side and the surface facing the low-pressure side. For the as-grown membranes, the side, which was facing the silicon substrate during membrane growth, was too smooth to be imaged. This side was facing the low-pressure side during permeation testing for all samples investigated by AFM. As can be seen, especially the differences between the surfaces facing the low-pressure side are large.

The samples which were tested but not further treated, have rougher surfaces, larger surface areas and larger and fewer grains than the as-grown samples. Furthermore, the samples which were heat-treated in air, have significantly rougher surface, larger surface area and larger and fewer surface grains than the samples which were not exposed to this treatment. The same trend is found for all thickness categories. Furthermore, the membrane sides facing towards the plasma during sputtering are rougher for the thicker membranes.

The topography investigations may enable us to explain at least parts of the improvement achieved by heat treatment in air. We find it plausible that the categories A–C membranes, and possibly also the category D membranes, are to some extent limited by surface processes before the treatment, and that the treatment alters the membrane surface in a favourable way. Higher surface area may give an increased number of active sites for hydrogen dissociation, and thus higher permeation, as has been observed by others [14,16,17]. This explanation is consistent with Fig. 5 and Table 3, which showed that the membranes are most likely bulk diffusion limited after the heat treatment in air, but probably also limited by other processes before the treatment. It was further argued that the category D membranes most likely are more limited by bulk diffusion than the thinner ones (A–C). If this is indeed the case, the category D membranes are expected to show a smaller increase in the permeance due to surface alterations. From Table 3, it is clear that these membranes show smaller enhancements by heat treatment in air than the thinner ones.

An additional correlation between surface topography and permeation is found when comparing the AFM images of as-grown samples and samples, which were tested but not further treated. After the initial exposure to hydrogen at 300 °C the membrane flux increases until stabilization, and as already stated, the samples examined after this point have higher surface area, roughness and grain size than the as-grown samples.

Investigation of the category E membranes further verifies a relationship between permeation and surface topography. The membrane, which was heat-treated in nitrogen and argon at 400 °C has higher surface area, roughness and grain size as compared to the membrane which was tested but not further

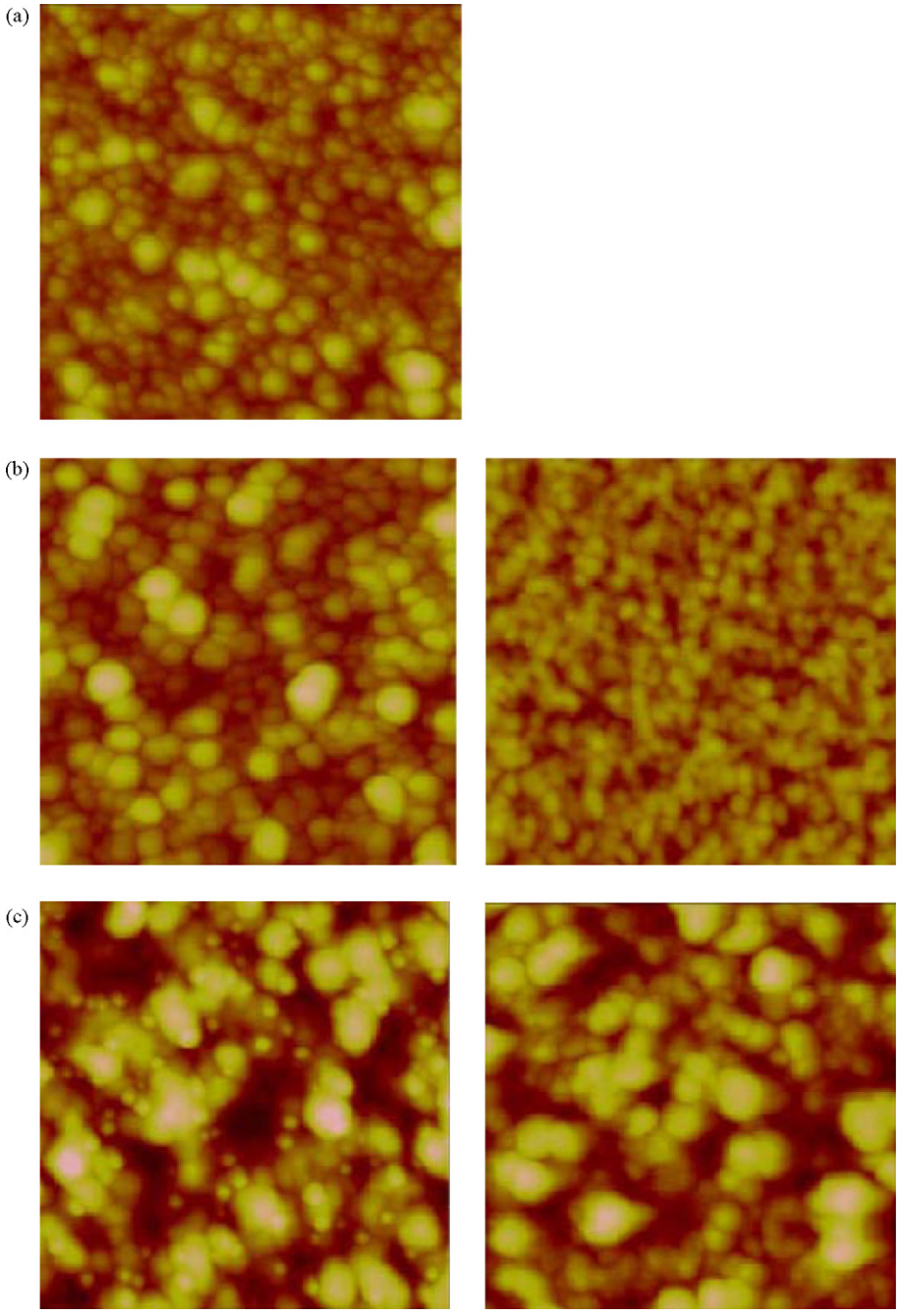

Fig. 6. AFM images of ∼1.3 μm thick membranes, (a) as-grown sample, (b) sample which was tested but not further treated, (c) sample heat-treated in air. The membrane surfaces facing the high-pressure side are shown to the left, while the membrane surfaces facing the low-pressure side are shown to the right. Image sizes are 1 μm × 1 μm, and the height range is 40 nm from dark to light.

treated, and the hydrogen permeation is significantly higher. It should be noted that the membrane heat-treated in air has even higher surface roughness, area and grain size than the membrane heat-treated in nitrogen and argon at 400 °C, despite similar permeation results. However, it could be that further improvement in permeation cannot be achieved after a certain change in surface topography is reached. If bulk diffusion limitation then starts to dominate, further alternation of the surface will not influence the hydrogen flux to any noticeable degree. In agreement with the trend observed, the membrane, which was exposed to hydrogen for an extended period of time and the membrane, which was tested but not further treated, have both similar surface topography and similar permeation rates.

We observe larger surface grains on the samples which have been heat-treated in air at 300 °C or heat-treated in nitrogen and argon at 400 °C. Grain growth in the membrane bulk has been reported to hamper the hydrogen flux by several researchers [28–30]. This has been attributed to a reduction in the grain boundary volume fraction, and thus a reduction in the hydrogen diffusion along the grain boundaries, and also to an increased

Table 4
Topographical values for ∼1.3 μm thick membranes

Condition	rms Values (nm)	Area (nm^2) × 1000	Diameter (nm)	Density ($1/\mu m^2$)
1[a]	3.0 ± 0.2	3.4 ± 0.4	34.1 ± 1.2	144 ± 9
2[a]	4.4 ± 0.1	6.0 ± 0.4	49.3 ± 1.6	84 ± 4
3[a]	7.5 ± 0.2	12.5 ± 2.3	73.8 ± 8.7	50 ± 7
2[b]	3.0 ± 0.1	2.7 ± 0.5	37.1 ± 3.0	150 ± 13
3[b]	6.4 ± 0.4	9.4 ± 0.7	62.2 ± 4.0	53 ± 4

Condition 1 refers to the as-grown samples, condition 2 to the membranes, which were tested but not further treated and condition 3 to the membranes heat-treated in air at 300 °C. The calculations are based on images of size 1 μm × 1 μm, and are averages of several images taken at different positions on each sample. Also given are the standard deviations.
[a] The membrane surface facing the high-pressure side.
[b] The membrane surface facing the low-pressure side.

membrane surface resistance. However, other researchers have found that grain growth in industrial membranes, as opposed to pure samples, does not influence the permeation rate to a high degree [31]. This was attributed to an opposing effect of impurities in the grain boundaries. Moreover, it has also been reported that hydrogen permeance appears to increase by grain growth [32]. It is unclear how the surface grain growth observed in this study, influences the permeation, but there is at least no indication that the growth significantly reduces the hydrogen flux of the membranes studied, rather the opposite tendency was found.

4. Conclusions

Free-standing Pd/Ag23 wt% membranes with thicknesses ranging from ∼1.3 to ∼5.0 μm were produced by magnetron sputtering. Thermal treatment in air at 300 °C significantly enhanced the hydrogen flux for all membranes, and a permeance reaching 1.7×10^{-2} mol/m^2 s Pa$^{0.5}$ was observed for the ∼1.3 μm membranes. Before heat treatment in air, the permeability values were found to vary, but they became fairly similar after the thermal treatment, indicating that the treatment resulted in mainly bulk diffusion limited hydrogen flux. The effect of thermal treatment on permeation was also found to depend on the membrane thickness, with less enhancement for the ∼5.0 μm thick membranes. AFM studies revealed that increased hydrogen permeation coincided with higher surface roughness, larger surface area and larger and fewer surface grains.

Acknowledgements

This work was supported by the Research Council of Norway, Grant No. 158516/S10 (NANOMAT). Astrid L. Mejdell would also like to thank the Gas Technology Center (NTNU-SINTEF), which is supported by the Research Council of Norway.

References

[1] S. Uemiya, T. Matsuda, E. Kikuchi, Hydrogen permeable palladium–silver alloy membrane supported on porous ceramics, J. Membr. Sci. 56 (1991) 315.
[2] N. Itoh, W.-C. Xu, Selective hydrogenation of phenol to cyclohexanone using palladium-based membranes as catalysts, Appl. Catal. A 107 (1993) 83.
[3] A.K.M. Fazle Kibria, Y. Sakamoto, The effect of alloying of palladium with silver and rhodium on the hydrogen solubility, miscibility gap and hysteresis, Int. J. Hydrogen Energy 25 (2000) 853.
[4] M. Nuovo, F.M. Mazzolai, F.A. Lewis, Studies of anelasticity in the palladium–silver–hydrogen system, J. Less-Common Met. 49 (1976) 37.
[5] G.J. Grashoff, C.E. Pilkington, C.W. Corti, The purification of hydrogen: a review of the technology emphasising the current status of palladium membrane diffusion, Plat. Met. Rev. 27 (1983) 157.
[6] J.T.F. Keurentjes, F.C. Gielens, H.D. Tong, C.J.M. van Rijn, M.A.G. Vorstman, High-flux palladium membranes based on microsystem technology, Ind. Eng. Chem. Res. 43 (2004) 4768.
[7] J.P. Collins, J.D. Way, Preparation and characterization of a composite palladium-ceramic membrane, Ind. Eng. Chem. Res. 32 (1993) 3006.
[8] T.S. Moss, N.M. Peachey, R.C. Snow, R.C. Dye, Multilayer metal membranes for hydrogen separation, Int. J. Hydrogen Energy 23 (1998) 99.
[9] S.-E. Nam, S.-H. Lee, K.-H. Lee, Preparation of a palladium alloy composite membrane supported in a porous stainless steel by vacuum electrodeposition, J. Membr. Sci. 153 (1999) 163.
[10] T.L. Ward, T. Dao, Model of hydrogen permeation behaviour in palladium membranes, J. Membr. Sci. 153 (1999) 211.
[11] A. Criscuoli, A. Basile, E. Drioli, O. Loiacono, An economic feasibility study of water gas shift membrane reactor, J. Membr. Sci. 181 (2001) 21.
[12] D. Fort, J.P.G. Farr, I.R. Harris, A comparison of palladium–silver and palladium–yttrium alloys as hydrogen separation membranes, J. Less-Common Met. 39 (1975) 293.
[13] J.N. Keuler, L. Lorenzen, Developing a heating procedure to optimise hydrogen permeance through Pd–Ag membranes of thickness less than 2.2 μm, J. Membr. Sci. 195 (2002) 203.
[14] F. Roa, J.D. Way, The effect of air exposure on palladium–copper composite membranes, Appl. Surf. Sci. 240 (2005) 85.
[15] J.K. Ali, E.J. Newson, D.W.T. Rippin, Deactivation and regeneration of Pd–Ag membranes for dehydrogenation reactions, J. Membr. Sci. 89 (1994) 171.
[16] H. Uchikawa, T. Okazaki, K. Sato, New technique of activating palladium surface for absorption of hydrogen or deuterium, Jpn. J. Appl. Phys. 32 (1993) 5095 (Part 1, No. 11A).
[17] D. Wang, J.D. Clewley, T.B. Flanagan, B. Balasubramaniam, K.L. Shanahan, Enhanced rates of hydrogen adsorption resulting from oxidation of Pd or internal oxidation of Pd–Al alloys, J. Alloys Compd. 298 (2000) 261.
[18] S. Uemiya, State-of-the-art of supported metal membranes for gas separation, Sep. Purif. Methods 28 (1999) 51.
[19] R. Bredesen, K. Jordal, O. Bolland, High-temperature membranes in power generation with CO_2 capture, Chem. Eng. Proc. 43 (2004) 1129.
[20] B.A. Wilhite, M.A. Schmidt, K.F. Jensen, Palladium-based micromembranes for hydrogen separation: device performance and chemical stability, Ind. Eng. Chem. Res. 43 (2004) 7083.
[21] D.J. Edlund, Hydrogen permeable membrane and method for producing the same, US Patent 6,419,728 (2002).
[22] H.D. Tong, E. Berenschot, M.J. De Boer, J.G.E. Gardeniers, H. Wensink, H.V. Jansen, W. Nijdam, M.C. Elwenspoek, F.C. Gielens, C.J.M. van Rijn, Microfabrication of palladium–silver alloy membranes for hydrogen separation, J. Microelectromech. Syst. 12 (2003) 622.
[23] R. Bredesen, H. Klette, Method of manufacturing thin metal membranes, US Patent 6,086,729 (2000).
[24] H. Klette, R. Bredesen, Sputtering of very thin palladium-alloy hydrogen separation membranes, Membr. Technol. 5 (2005) 7.
[25] L. Yang, Z. Zhang, B. Yao, X. Gao, Hydrogen permeance and surface states of Pd–Ag/ceramic composite membranes, AIChE J. 52 (2006) 2783.
[26] H. Klette, H. Raeder, Y. Larring, R. Bredesen, Development of supported palladium alloy membranes, in: D.C. Thomas (Ed.), Carbon Dioxide Capture for Storage in Deep Geologic Formations—Results from the CO_2

Capture Project Capture and Separation of Carbon Dioxide from Combustion Sources, Elsevier, New York, 2005, pp. 377–384.
[27] To be published.
[28] U. Stuhr, T. Striffler, H. Wipf, H. Natter, B. Wettmann, S. Janssen, R. Hempelmann, H. Hahn, An investigation of hydrogen diffusion in nanocrystalline Pd by neutron spectroscopy, J. Alloys Compd. 253–254 (1997) 393.
[29] H. Natter, B. Wettmann, B. Heisel, R. Hempelmann, Hydrogen in nanocrystalline palladium, J. Alloys Compd. 253–254 (1997) 84 .
[30] K.J. Bryden, J.Y. Ying, Nanostructured palladium–iron membranes for hydrogen separation and membrane hydrogenation reactions, J. Membr. Sci. 203 (2002) 29.
[31] S. Heinze, B. Vuillemin, J.C. Colson, Relation between grain size and hydrogen diffusion coefficient in an industrial Pd–23% Ag alloy, Solid State Ionics 122 (1999) 51.
[32] B.A. McCool, Y.S. Lin, Nanostructured thin palladium–silver membranes: effects of grain size on gas permeation properties, J. Mater. Sci. 36 (2001) 3221.

Paper II

Surface characterization of thin Pd/Ag 23wt% membranes after different thermal treatments

A. Ramachandran, W. M. Tucho, A.L. Mejdell, M. Stange, H. Venvik, J. Walmsley, R. Holmestad, R. Bredesen and A. Borg

To be submitted to Applied Surface Science

Surface characterization of Pd/Ag23wt% membranes after different thermal treatments

A. Ramachandran[1], W. M. Tucho[1], A. L. Mejdell[2], M. Stange[4], H. Venvik[2], J. Walmsley[3], R. Holmestad[1], R. Bredesen[4], A. Borg[1].

[1]Department of Physics, Norwegian University of Science and Technology (NTNU), N-7491 Trondheim, Norway

[2]Department of Chemical Engineering, NTNU, Trondheim, Norway

[3]SINTEF Materials and Chemistry, N-7465 Trondheim, Norway

[4]SINTEF Materials and Chemistry, N-0314, Oslo, Norway

Abstract

Pd/Ag23wt% membranes with thickness of 1.5-10 μm were prepared by magnetron sputtering and mounted in a self-supported configuration. Hydrogen permeation measurements before and after thermal treatments in the temperature range 300°C-450°C in N_2(feed side) and Ar (permeate side) were performed. Accompanying changes in the surface topography and chemical composition were subsequently investigated by atomic force microscopy (AFM), X-ray photoelectron spectroscopy (XPS) and Auger Electron Spectroscopy (AES) depth profiling. For a 2 μm thick membrane the surface roughness and area increase for all N_2/Ar annealing temperatures applied, while a temperature of 450°C was required for an increase in roughness of both membrane surfaces to occur for a 5 μm membrane. The thickest membrane, of 10 μm, showed change in the surface roughness and area on one side of the membrane only and a slight decrease in hydrogen permeance after all heat treatments in N_2/Ar. XPS investigations performed after treatment and subsequent permeation measurements reveal segregation of silver to the membrane surfaces for all annealing temperatures applied. In comparison, heat treatment at 300°C in air gave higher hydrogen permeance accompanied by increasing surface roughness and area as well as different segregation behavior at the membrane surfaces. The available data point at bulk limited hydrogen permeation for Pd/Ag23wt% membranes after heat treatment in air at 300°C for thicknesses down to 1.5-2.0 μm. A transition from surface to bulk control upon

treatment is feasible, at least for the thinner membranes, but the changes in permeance can not be fully accounted for by changes in surface structure and composition.

Key words: PdAg membranes, hydrogen permeation, topography, segregation.

Corresponding author: anne.borg@phys.ntnu.no

1. Introduction

Hydrogen has many applications in industry and is one of the energy carriers that have recently attracted interest due to its potential as a zero emission fuel [1-3]. Hydrogen can be produced from renewable biomass as well as fossil fuels, in addition to the energy intensive electrolysis of water [4-6]. A potentially efficient technology for hydrogen production and purification is the use of inorganic hydrogen separation membranes. Palladium (Pd) is both highly soluble and permeable to hydrogen, thus a potential candidate membrane material. To prevent embrittlement occurring in pure Pd due to hydride phases formation [7, 8], Pd alloys suppressing the phase transition are often used. Silver (Ag) has been identified as a favorable alloying element, giving membranes with even higher hydrogen permeation than pure Pd. Alloying of Pd with 23wt% Ag has been found to be an optimum composition for the hydrogen permeability [9]. The hydrogen flux generally being inversely proportional to the membrane thickness and the high material costs of Pd, have motivated research to develop thin supported membranes (composite membranes). PdAg films can be prepared by different methods [9-13], but our approach is based on the SINTEF method [14] where magnetron sputtering onto highly polished silicon single crystal wafers is combined with a lift-off technique [14]. These films can further be used in various membrane support and reactor configurations [15, 16], of which a flat, self-supported membrane has proved particularly useful for investigations using advanced characterization techniques.

The hydrogen permeation process through Pd based membranes involves dissociative adsorption of hydrogen at the membrane high pressure, feed side, bulk diffusion of atomic hydrogen and subsequent recombinative desorption at the low pressure, permeate side membrane surface [17, 18]. In addition, gas phase transport phenomena may influence the permeation under certain conditions and configurations. It is commonly reported that the bulk diffusion is the rate-limiting step for thicker membranes [19]. The hydrogen flux in such cases is assumed proportional to the difference in the square root of the pressure at the feed side and at the permeate side of the membrane. Deviations from a linear dependence on the difference of square root

pressures suggest that the surface processes as well as other effects could be dominating the hydrogen permeation process [20].

The hydrogen transport properties of Pd-based membranes depend on the combined history of temperature and gaseous exposure, in addition to the thickness and the as-prepared material properties. Gaseous species other than H_2 are either components of the separation mixture or the sweep gas, or they are introduced during various treatments that are applied to enhance the membrane properties. Species such as N_2 and Ar are normally considered inert, at least when present in mixture with hydrogen [15, 21], but some studies report negative effects of N_2, [22-24]. Species that have received attention because they are often part of separation mixtures include O_2/air [25-27], H_2O [28-32] , CO [24-26, 28, 29, 31, 33-35], CO_2 [24, 28, 32, 35], CH_4 [24, 28], methanol [25, 27, 29] and H_2S [36-38], of which e.g. CO and H_2S may strongly affect permeation even when present in low concentrations [35, 38, 39]. An inhibitive effect of O_2 was reported when present in mixture with H_2, over a pure Pd membrane as well as formation of H_2O (by catalytic combustion over the Pd membrane surface) [26], while addition of Ag to the surface was found to suppress this effect [27]. Several authors, including our group, report on enhanced hydrogen flux through Pd-based alloy membranes after thermal treatment in air at temperatures of 300˚C or higher [22, 38, 40-42], but a clear understanding of the effect of air/oxygen is not established. Removal of carbonaceous and other poisonous species has been suggested as an explanation for the increase in flux, and it was shown that air can be used to regenerate poisoned membranes [41]. Roa and Way [42] found, however, that the cleaning-only hypothesis was insufficient in explaining the improvements in hydrogen flux. In our previous study we suggested roughening and increase of surface area to be part of the explanation for PdAg membranes in the 1-5 μm thickness range [40]. We furthermore found that an alternative heat treatment at 400°C in an atmosphere consisting of N_2 at the feed side and Ar at the permeate side of a 1.5 μm thick Pd/Ag23wt% membrane gave enhanced hydrogen flux similar to that observed after heating in air at 300°C [40]. The N_2/Ar atmosphere was presumed inert, i.e. to have no effect on the membrane except the temperature during exposure.

It is also important to mention that surface segregation effects between Pd and Ag under various atmospheres have been both predicted and reported for PdAg alloys. Shu et al. [43] reported segregation of both Pd (to feed surface) and Ag (to permeate surface) under pure hydrogen, and furthermore predicted segregation of Ag to the surface as a result of N_2 exposure, based on findings on catalysts/single crystal surfaces. First-principles band-structure calculations also indicated hydrogen adsorption induced segregation of Pd to the surface [44].

The effects of N_2/Ar treatment have been investigated in more detail in the present work, and the influence of treatment temperature and membrane thickness have been addressed. The hydrogen permeation results based on these experiments is the topic of a separate publication [45]. An investigation of the resulting membrane bulk microstructure is also reported separately [46]. The current paper focuses on the surface topography changes observed after the treatment procedures and subsequent hydrogen flux measurements and the accompanying segregation effects at the membrane surfaces. These findings are compared to corresponding measurements performed on membranes with similar thicknesses heated in air at 300°C.

2. Experimental

Pd/Ag (23 wt %) thin films were prepared by dc magnetron sputtering (CVC 601 sputtering apparatus) using high purity argon (99.999%) as the sputter gas. The films were sputtered from a Pd/Ag23wt% target onto polished silicon single crystal substrates. The detailed description of the PdAg thin film preparation technique has been published earlier [14]. During sputtering, the silicon wafers were placed on a carousel, rotating at constant speed, so that nearly equal growth rate and composition are expected for membranes produced in the same sputtering run. Films in three thickness categories, i.e. 2 μm, 5 μm and 10 μm, were prepared. The 5μm and 10μm films were prepared using the same sputtering target. After sputtering the film thicknesses were determined by white light interferometry (WYKOT NT-2000, Veeco

Instruments, USA). The thicknesses of the membranes investigated in the present study were determined at 1.9 μm ± 0.1 μm, 5.4 μm ± 0.4 μm and 10.0 μm ± 1.0 μm. The thin membrane exposed to air at 300°C was prepared separately and was measured at a thickness of 1.5 μm [40, 46]. After sputtering the films were carefully lifted off the silicon substrate and mounted in the self-supported configuration. The procedure for preparing and mounting the membrane set-up for hydrogen permeation measurements has been described in earlier work [40]. The growth side of the as-grown film was always facing the feed side and the surface in contact with the silicon wafer during film deposition was facing the permeate side during treatment and permeation measurements. The effective area of the membrane used for the hydrogen permeation measurements was ~2.0 cm^2.

The different heat treatment procedures performed for the PdAg membranes are listed in Table 1. All membranes were initially heated to 300°C in N_2 and Ar. At this temperature, the N_2 feed gas was mixed with an equal flow of H_2 and each membrane was left for ~24 hrs to reach a stable hydrogen flux. This was followed by permeance measurements under pure hydrogen at the feed side (200 Nml/min) and without sweep gas at the permeate side. The differential pressure across the membrane was varied from ~5 kPa to ~25 kPa for the 1.5 and 2 μm membranes during hydrogen permeation measurements. The upper limit of the differential pressure across the membrane was extended up to 43 kPa and 52 kPa for the 5 and 10 μm membranes respectively. Membranes from each thickness category were then subjected to thermal treatment in N_2 (feed side) and Ar (permeate side) at 300°C, 400°C and 450°C or in air at 300˚C. The thermal treatments had duration of 3.5 to 4 days. Permeance measurements in pure hydrogen were then performed in the same way as before heat treatment. Additionally, to investigate the temperature dependence of the permeation, the H_2 flux through the 10 μm membrane heated in N_2/Ar at 450°C was measured at 375 and 450°C [45]. Leakage tests were performed before and after each measurement using He at a flow rate up to 100 ml/min at the maximum differential pressure applied. In addition to this measurement series, a 2 μm membrane was treated in pure oxygen at 300°C after the hydrogen stabilization and without performing the subsequent hydrogen permeation measurements. Finally, two 2 μm membranes were cooled down in hydrogen after the

first hydrogen permeance measurements (see table 1). Two different cooling rates were chosen, one at 4°C/min as for cooling down in in N_2/Ar (see table 1), and the other through rapid cool-down by opening the furnace surrounding the membrane set-up.

The samples are labelled with membrane thickness, gas exposure and the temperature of the treatment, for example 2Mi300 where 2 refers the thickness of the membrane being 2 μm, 'i' represents the inert (N_2/Ar) atmosphere and 300 denotes the temperature during the treatment. Pure oxygen treatment is denoted by "o", while exposure to air at 300°C for the selected membranes is represented by 'a'. High purity (99.999%) gases N_2, Ar and O_2 were used.

Table 1.

The surface topography of both the feed and permeate sides of the heat treated membranes were examined by Atomic Force Microscopy (AFM). A Multimode SPM from Digital Instruments was used in tapping mode, and the instrument software was used to determine the root mean square surface roughness and the surface area of both membrane surfaces. For comparison, as-grown samples, denoted AG, were examined after they were lifted off the silicon wafer. All images were flattened using a first order polynomial.

The surface chemical composition was determined by X-ray photoelectron spectroscopy (XPS) with a KRATOS AXIS ULTRA^{DLD} spectrometer using monochromatic Al K radiation ($h\nu$ =1486.6 eV). The pass energy for the wide scan and the element scan was 160eV and 20 eV, respectively, the latter yielding an overall energy resolution of 330 meV. Depth profile analysis of the elemental composition was performed by Auger Electron Spectroscopy (AES) using a JEOL JAMP 9500F Field Emission Auger Microprobe. The spectral energy resolution for the AES measurements was 0.6% of the kinetic energy. The electron beam voltage and current during AES measurement were 10 keV and 2.73×10^{-9} A, respectively. An ion energy of 500 eV was used during depth

profile sputtering, which was performed in steps of 15 s. The sputtering rate was calibrated with the as-grown PdAg membranes and determined to 2 nm/min.

3. Results

3.1 Hydrogen permeation

Fig. 1 shows the hydrogen flux results obtained before and after thermal treatment in N_2/Ar at 300°C (a), 400°C (b) and 450°C (c) as well as before and after heat treatment in air at 300°C (d). The hydrogen flux is plotted as a function of difference between the square root of the feed and permeate side partial pressures. The power dependency of the differential pressure is chosen as 0.5 so that the present results can be compared to previously reported data [38, 39, 45-47].

(Figure 1)

As can be seen from Fig. 1a thermal treatments in N_2/Ar at 300°C give increased hydrogen flux as compared to the flux measured before the thermal treatment for the 2 μm membrane while the flux decreases for the two other membrane thicknesses, more pronounced for the 10 μm membrane. Turning to the corresponding N_2/Ar heat treatment at 400°C, the flux behavior is similar (Fig. 1b). At the highest N_2/Ar treatment temperature, 450°C, the flux is increasing for both the 2 μm and 5 μm membranes while this is not observed for the 10 μm membranes. Heat treatment in air at 300°C results in increased flux for all membrane thicknesses as shown in Fig. 1d. It should be noted that the flux measured for the 10 μm membrane before treatment in air was lower than observed for the other 10 μm membranes investigated in the present work. The calculated hydrogen permeance values for all investigated samples before and after the abovementioned treatments are summarized in Table 2. A more detailed presentation of the hydrogen permeation results is given elsewhere [45].

(Table 2)

3.2 AFM investigations

The surface topography as measured by AFM after heat treatments in N_2/Ar and air at the selected temperatures as well as for the as-grown Pd/Ag23wt% films is shown in

Fig. 2 for the 2 μm membrane, in Fig. 3 for the 5 μm membrane and in Fig. 4 for the 10 μm membrane. Representative images for both the feed (images to the left) and permeate side (images to the right) membrane surfaces are presented except for the as-grown membranes where the surface facing the silicon substrate during sputter deposition was too smooth to be imaged by AFM, as also observed earlier [40]. AFM images after heat treatment in dry air at 300°C for the 5 μm thick membrane could not be obtained due to formation of large protrusions formed at the membrane surfaces after this procedure [46]. The scan size of the images for 2 μm (Fig 2) and 5 μm (Fig 3) membranes is (1x1) μm^2. Due to the large grains present in the 10 μm thick membrane, images with scan size (5x5) μm^2 are shown in Fig. 4. As seen from Fig. 2, the surface roughness at the feed side of the 2 μm thick membrane is increasing slightly after heat treatment at 300°C and 400°C, a tendency strongly enhanced after heating to 450°C. The change is more pronounced for the permeate side surface which was initially much smoother. After heat treatment in air at 300°C, both the feed and permeate surfaces topographies appear similar to the observations for the membrane heated in N_2/Ar at 450°C. In the case of the 5 μm membrane (Fig. 3) the topographic changes at the feed side are pronounced after heating to 450°C but not after heating to 300°C or 400°C, while the surface roughness appears to increase with temperature for the permeate side. Finally, for the 10 μm membrane (Fig. 4) no significant changes in the surface topography are observed for the feed side, while the permeate side also in this case shows increasing surface roughness for higher heat treatment temperatures as found for the smaller thicknesses. For this membrane the surface topography is similar at both the feed and permeate sides after heating at 400°C (10Mi400) when compared to the membrane heat-treated in air (10Ma300) at 300°C.

(Figure 2-4)

As a quantitative measure of the surface roughness the root mean square (rms) value of the roughness together with the corresponding standard deviation have been calculated from the recorded AFM images. The resulting rms roughness as determined from AFM images taken at ten different locations on each sample is listed in Table 3. The corresponding calculated surface areas are also presented in the table. The roughness

analysis of the 2 μm and 5 μm thick membranes was based on (1x1) μm^2 AFM images [40], while (5x5) μm^2 images were used for the 10 μm membrane due to the larger roughness observed initially for this membrane. As a result, the data for the 2 μm and 5 μm thick samples cannot be directly compared to the data for the 10 μm thick samples. Comparisons made for different image sizes indicate that the roughness values are generally slightly higher for larger images. The estimated surface area cannot be compared both because of different image sizes and the method of area determination [48]. Figure 5 illustrates the trends in the quantitative changes in the rms roughness (listed in Table 3) before and after the different thermal treatments for the three membrane thickness categories (vertical axis to the left) together with the corresponding permeability data (vertical axis to the right) taken from Table 2.

(Table 3)

(Figure 5)

3.3 Surface composition

The chemical composition of the feed side membrane surfaces, both for the as-grown samples and thermally treated samples was investigated using XPS in order to reveal possible changes in chemical composition due to the different heat treatments. Only two 5 μm membranes were investigated, as scattered particles iron containing particles were observed on the surface of samples 5Mi300, 5Mi400 by scanning electron microscopy and energy dispersive x-ray analysis. Wide scan XPS spectra (not shown) revealed that in addition to palladium and silver traces of carbon and oxygen were present at all membrane surfaces. Due to some exposure to the ambient during transfer between the membrane set-up and the XPS system slight oxidation as well as carbon contamination are expected in all cases. However, the carbon level does not change significantly between the different treatments. If carbon was present in the bulk of the membrane segregation to the surface upon heat treatment would be expected [49, 50]. Moreover, in the case of heating in oxygen/air surface carbon should be removed in the presence of oxygen while heating in N_2/Ar should not give this effect. Our observations therefore suggest that the main source of the carbon is exposure to ambient CO_2 during sample

transfer. Other contaminants were not observed. In particular, nitrogen was not detected for any of the samples within the XPS detection limit.

The relative amount of Pd and Ag in the surface after the different heat treatments as compared to the as-grown Pd/23%Ag films has been determined from the relative intensities of the Pd3d and Ag3d core levels. This is illustrated in Fig. 6 for the 2 μm thick membranes. A spectrum is also shown for a membrane, entitled 2Mo300, which was cooled down to room temperature without subsequent hydrogen permeation measurements after the oxygen treatment at 300°C. As can be seen by comparing the different panels in Fig. 6, the relative intensity of the Ag3d peaks is higher after heating in N_2/Ar at the selected temperatures. Similar behavior is found for the other membrane thicknesses. A very strong reduction in the silver signal is observed for the 2Mo300 sample.

(Figure 6)

A quantitative comparison for all three membrane thicknesses based on measuring the relative intensities of the $Ag3d_{5/2}$ and $Pd3d_{5/2}$ core level peaks of the heat treated membranes as compared to the as-grown films is summarized in Table 4. It is found that surface segregation of silver occurs upon heating the 2 μm membranes in N_2/Ar, with the amount of Ag in the surface region increasing with heating temperature. In comparison, a 1.5 μm membrane heat treated in air at 300°C (1.5Ma300) shows palladium segregation to the surface. The two 5 μm membranes measured by XPS follow the same trend. Also for the 10 μm membrane silver segregation occurs upon heating in N_2/Ar also for the 10 μm membrane. For this membrane thickness, however, silver segregation is even found after heat treatment in air at 300°C (10Ma300).

(Table 4)

A more detailed analysis of the Pd3d spectra of the as-grown and thermally treated membranes was undertaken. The $Pd3d_{5/2}$ core level spectrum of the as-grown 2 μm film (2AG) is shown in the lower panel in Figure 7, together with the same spectral region

for the 2 μm membranes heat treated at 300°C (2Mi300 and 2Mo300). The dashed lines are fitted curves for the spectra obtained through fitting the different contributions by Doniach-Sunjic line shapes [51] convoluted with a Gaussian function. The vertical line indicates the binding energy position of the Pd bulk component. For the as-grown film some initial oxide formation is observed, with a binding energy shift ~0.61 ± 0.03 eV relative to the bulk contribution. This sub-oxide (PdO_x with $x < 1$) is, as already stated, attributed to the exposure to air during transfer between the membrane reactor chamber and the XPS system. This spectrum is quite similar to those observed after the different heat treatments, illustrated by the spectrum for 2Mi300, followed by the hydrogen permeation measurements. In comparison, the $Pd3d_{5/2}$ spectrum obtained for membrane 2Mo300, where no hydrogen permeation measurements have been performed after the oxygen treatment, shows a strong palladium oxide (PdO) contribution with a chemical shift of 1.9 eV compared to bulk Pd. The corresponding O1s spectrum (not shown) reveals a strong oxygen contribution. This oxide formation is accompanied by a strong Pd segregation to the surface as evident from the relative Ag/Pd intensity ratio listed for this sample in Table 3. The thickness of this oxide layer was determined by Auger electron spectroscopy combined with sputtering. The resulting depth profiles measured for Pd, Ag and O are displayed in Fig. 8, and show that the oxide is about 2 nm thick. Corresponding measurements at the permeate side of this membrane gave an oxide thickness of 3 nm. The relative amount of Pd and Ag cannot be deduced from the AES data as the sputter yield is higher for silver than palladium.

(Figure 7)

(Figure 8)

4. Discussion

The hydrogen permeation behavior of free-standing Pd/Ag23wt% membranes is discussed in detail in other publications [15, 40, 45] and will in the present work be viewed in relation to the surface characterization results. From the AFM studies it should be noted that the surface roughness of the permeate side surfaces increases for all three membrane thicknesses with a larger roughness for the higher annealing

temperatures for the heat treatment in N_2/Ar. These changes are reflecting the underlying grain structures and are hence a result of grain growth within the polycrystalline membrane itself, which can be understood from the Gibbs-Thompson relation and is discussed in more detail elsewhere [46]. Due to the high density of smaller grains, as well as presence of micro-strains, near the surface facing the substrate of the as-grown film [46] more pronounced grain growth is expected at the permeate/substrate side of membrane surfaces as compared to the feed side, irrespective of the membrane thickness. This is also in agreement with our AFM measurements. Moreover, the surface roughness at the permeate side of the air treated 1.5 μm and 10 μm membranes is larger than for the corresponding membranes treated in N_2/Ar at 300˚C. This difference may in part be understood by the fact that a palladium oxide is formed at the surface upon air exposure, as illustrated through our XPS and Auger data for the 2Mo300 sample. This oxide formation causes morphological and compositional changes in the surface and near surface layers. The following reduction during the hydrogen permeation measurements results in further composition changes as can been seen from comparing the Ag/Pd intensity ratios for the samples 1.5Ma300 and 2Mo300. Morphological changes of Pd surfaces exposed to air at elevated temperatures have been reported by several researchers [42, 52]. Aggarwal et.al [52] reported self-assembly of micrometer scale hillocks of conducting palladium oxide upon heating in oxygen at 900°C, accompanied by 38% volume change due to the structural differences between Pd and palladium oxide. The origin of hillock formation was further studied by Roa and Way [42] in order to relate these structures to the air-purging effect on hydrogen permeation for Pd-Cu composite membranes. They also found hillock formation after the membranes were exposed to air at 900°C for 1 hour, with heights of the order ~0.2 μm. Due to the much higher temperature these results are not directly comparable, but we mention them as they could have relevance to our observations.

The changes in surface topography observed for the 1.5 μm membrane after air treatment (sample 1.5Ma300) is not a replica of the surface oxide formed since the size of the features responsible for the roughness far exceeds the thickness of the oxide, which is only a few nm. The surface roughness observed for the 1.5Ma300 sample (24 ± 3 nm) is considerably higher than previously reported for similar membranes after the

same thermal treatment [40]. TEM cross sectional studies of the 1.5Ma300 sample showed void formation within the first 200 nm below the surface [35]. Some of these penetrate the surface appearing as pits which contribute to the observed roughness. In comparison, we find a surface roughness of 5.8 ± 0.3 nm for the feed side surface and 5.1 ± 0.9 nm for the permeate side surface of sample 2Mo300, which for the feed side surface is the same as that observed for the as-grown film (2AG). This finding may suggest that also the reduction and hydrogen permeation measurement stage after the thermal treatment contributes to the changes in surface topography.

The topographical changes at the feed side membrane surfaces depend on the film thickness. For the 2 μm membrane the surface roughness and surface area increase for treatment in N_2/Ar at all selected temperatures, where very high values are obtained after heating in N_2/Ar at 450˚C, as also observed after the treatment in air for the 1.5 μm membrane. The annealing temperature has to reach 450˚C before the surface topography changes for the feed side surface of the 5 μm membranes, while no quantitative changes are observed for the 10 μm membranes.

As seen from the XPS data presented in Table 4, the changes in surface topography are accompanied by compositional changes in the outer surface region. Enrichment of silver in the surface due to the heat treatment in inert atmosphere is observed for all thickness categories in the present work. This segregation effect can be understood from the fact that silver has a lower surface energy than palladium [53, 54]. Dissociation of H_2 is an important initial step in the hydrogen permeation process. As is well known from literature, H_2 is readily dissociating on Pd, while the adsorption of H_2 on silver is weak [55, 56]. As a result of silver segregation the number of active sites for H_2 dissociation at the membrane surfaces may be reduced, which in turn may affect hydrogen permeation.

Hydrogen induced Pd segregation to the very first surface layer of Pd-Ag alloys has recently been predicted by theoretical calculations [44]. To address the effect of the hydrogen permeation on the composition in the surface region, two thin 2 μm PdAg membranes were cooled down in hydrogen at two different cooling rates (2Mh300F and

2Mh300S), after the initial stabilization in H_2:N_2 and first hydrogen permeance measurements at 300°C (permeance 1 in Table 1). XPS analysis of the resulting surface composition shows Ag surface segregation. Our result cannot exclude that Pd segregation to the outermost surface layer may occur, but they clearly indicate silver enrichment in the surface region during the hydrogen permeation measurements. Also contaminants such as carbon may segregate to the surface upon annealing, but differences in surface carbon concentration could not be established between the samples. However, due to the exposures to atmosphere prior to XPS measurements, we cannot draw an explicit conclusion on this point.

The effect of the air treatment at 300°C on the membrane surface composition is clearly illustrated by the XPS results for the 2Mo300 sample, where the amount of silver is decreased by 70% relative to the amount for the as-grown film within the XPS probing depth. The oxide formation induces strong segregation of palladium towards the surface and an accompanying depletion of silver. As a result, initially after air treatment and reduction in H_2, a higher number of palladium sites are available for the H_2 dissociation as compared to that for the treatments in N_2/Ar. During the continued hydrogen permeation measurements, the amount of silver in the outermost surface layers may again increase. As seen from our XPS results for the 2 and 5 μm membranes heat-treated in air, Pd enrichment is still observed after permeation measurements. Segregation of Pd has also previously been reported after hydrogen permeation measurements for the Pd-Ag/ceramic composite membranes treated in air at 400°C [38, 41], and was also in this case attributed to diffusion of Pd towards the surface during the air treatment. Combinations of heat treatment in air with reduction in hydrogen followed by flux measurements of thicker membranes have yielded both palladium segregation (high pressure side) and silver segregation (low pressure side), and hydrogen chemisorption induced Pd segregation was suggested in this case [43]. In the present work, the amount of silver at the feed side surface of membrane 10Ma300 is higher than for the as-grown film and only slightly lower than for the N_2/Ar heat-treated membranes. The reason for this deviating experimental result is not known, and further systematic studies are required to fully understand the segregation behavior of the PdAg membrane system.

An important issue for the performance of hydrogen permeable membranes is the transport limiting step. To unambiguously determine whether the hydrogen permeation is limited by the surface or the bulk, the hydrogen permeance should be plotted versus inverse membrane thickness, as in our previous paper [40]. Fig. 9 shows a plot of permeance vs inverse thickness, including all data obtained in our group on sputtered Pd/23wt%Ag membranes that were heat treated in air at 300°C and investigated in different configurations [40, 45], including the present work. The regression line fitted to all permeance data after treatment suggests a linear relationship between hydrogen permeance and inverse membrane thickness. These data therefore further support the conclusion on bulk transport limitation for 300°C air treated membranes of thickness 1.5-2.0 μm and higher. The possibility of a transition to surface limitation in the thickness range 1-1.5 μm can, however, not be excluded without investigating membranes below this thickness. .It is also possible that the transport could be surface limited before the treatment, at least for the lower thicknesses, possibly by the smooth, relatively low surface area permeate surface. Permeance data obtained before any treatment generally show larger deviations in permeance vs inverse thickness linear regression plots (not shown), and appear somewhat dependent on sputtering parameters such as batch and target, which makes it more difficult to conclude on transport limiting steps.

(Figure 9)

For the N_2/Ar treatment the number of membranes investigated in each thickness category and at the different annealing temperatures is more limited, but the permeance-inverse thickness relation appears to hold at least for thicknesses of 10 μm and higher [45]. In Fig. 5 the surface roughness data measured after the different thermal treatments are compared to the hydrogen permeability before and after treatment. For the thin 2 μm membranes increased hydrogen permeability after thermal treated in N_2/Ar at all three temperatures is observed along with increasing surface roughness and area. These observations could indicate that the hydrogen flux through the 2 μm membranes may be affected by surface limitations prior to thermal treatment and also after thermal treatments in N_2/Ar, The behavior is the quite different for the 5 μm and

10 μm membranes, where the permeability is lower after heating in N_2/Ar at 300°C and 400°C as compared to before treatment. At the same time the permeate side surface roughness is increasing, while no changes are seen in the surface topography at the feed side surfaces, indicating that available surface area for dissociative adsorption of hydrogen at the feed side and recombinative hydrogen desorption at the permeate side is not limiting the hydrogen permeation. One may therefore suggest that these membranes are bulk limited before heat treatment, though the permeability is higher after treatment in air at 300°C. For both these membrane thicknesses the permeability improves after annealing in N_2/Ar at 450°C, most significantly for the 5 μm membrane which is exceeding the value before treatment. Also an increased surface roughness at the feed side surface is observed for this membrane.

For all treatment conditions applied, the permeance generally decreases with increasing thickness (see table 2). But differently from air treatment, for a thickness-temperature treatment window an actual decrease in permeance is observed compared to before treatment in N_2/Ar. One may speculate if surface segregation effects change permeability differently depending on thickness. The ratio between silver and palladium atoms in the outermost surface layer may affect the number of available sites for H_2 dissociation. Moreover, permeability is determined by the hydrogen solubility and diffusivity [57], both parameters depending on composition. For Pd-Au alloys bulk hydrogen occupancy sites were found to change by the concentration of Au as determined from neutron diffraction and thermal desorption experiments [58]. Also inelastic incoherent neutron scattering studies for the atomically ordered phase of palladium-silver hydrides showed a large difference between Pd-H and Ag-H interactions in the hydrides [59]. Our observed surface segregation may be in line of such arguments reflecting variations in permeability for thin membrane materials.

As compared to treatment in N_2/Ar, treatment in air should also facilitate removal of possible carbonaceous contaminants from the membrane surfaces, as previously discussed for Pd-Ag/ceramic composite membranes [41]. As shown above, however, we were not able to establish any trend in contamination levels for the different treatments.

5. Conclusions

Hydrogen permeation measurements before and after thermal treatment in the temperature range 300°C-450°C in N_2/Ar for Pd/Ag23wt% membranes of different thicknesses have been compared to observed changes in the surface topography and chemical composition. For a 2 μm thick membrane the surface roughness and area increase for all annealing temperatures applied, while a temperature of 450°C was required for an increase in roughness of both membrane surfaces to occur for a 5 μm membrane. The thickest membrane, of 10 μm, showed change in the surface roughness and area on one side of the membrane only and a slight decrease in hydrogen permeance after all heat treatments in N_2/Ar. XPS investigations performed after treatment and subsequent permeation measurements reveal segregation of silver to the membrane surfaces for all annealing temperatures applied. In comparison, heat treatment at 300°C in air gave higher hydrogen permeance accompanied by increasing surface roughness and area as well as different segregation behavior at the membrane surfaces. The available data material points at bulk limited hydrogen permeation for Pd/Ag23wt% membranes after heat treatment in air at 300°C for thicknesses down to 1.5-2.0 μm. A transition from surface to bulk control upon treatment is feasible, at least for the thinner membranes, but the changes in permeance can not be fully accounted for by changes in surface structure and composition.

References

[1] Y. Kato, C.Y. Liu, K.-I. Otsuka, Y. Okuda and Y. Yoshizawa,Progress in Nuclear Energy, 2005. **47**(1-4): p. 504-511.

[2] Y. Kato, K. Otsuka and C.Y. Liu,Chemical Engineering Research and Design, 2005. **83**(7): p. 900-904.

[3] Y. Kato, Otsuka, Ken-ichiro, Ryu, Junichi,Progress in Nuclear Energy, 2008. **50**(2-6): p. 417-421.

[4] D. Wang, S. Czernik, D. Montane, M. Mann and E. Chornet,Industrial & Engineering Chemistry Research, 1997. **36**(5): p. 1507-1518.

[5] L. Garcia, R. French, S. Czernik and E. Chornet,Applied Catalysis A: General, 2000. **201**(2): p. 225-239.

[6] G.J. Stiegel and R.C. Maxwell,Fuel Processing Technology, 2001. **71**(1-3): p. 79-97.

[7] G.J. Grashoff, C.E. Pilkington, C.W. Corti.,Plat. Met. Rev., 1983. **27**: p. 157.

[8] A.K.M. Fazle Kibria, T. Tanaka, Y. Sakamoto.,Int. J. Hydrogen Energy., 1998. **23**(10): p. 891.

[9] S. Uemiya, T. Matsuda and E. Kikuchi,Journal of Membrane Science, 1991. **56**(3): p. 315-325.

[10] S.-Y. Lu and Y.-Z. Lin,Thin Solid Films, 2000. **376**(1-2): p. 67-72.

[11] D. Pizzi, R. Worth, M. Giacinti Baschetti, G.C. Sarti and K.-i. Noda,Journal of Membrane Science, 2008. **325**(1): p. 446-453.

[12] Z.Y. Li, H. Maeda, K. Kusakabe, S. Morooka, H. Anzai and S. Akiyama,Journal of Membrane Science, 1993. **78**(3): p. 247-254.

[13] W.-H. Lin and H.-F. Chang,Surface and Coatings Technology, 2005. **194**(1): p. 157-166.

[14] R. Bredesen, H. Klette.,,US Patent No. 6086729A, 2000.

[15] A.L. Mejdell, M. Jøndahl, T.A. Peters, R. Bredesen and H.J. Venvik,Journal of Membrane Science, 2009. **327**(1-2): p. 6-10.

[16] T.A. Peters, W.M. Tucho, A. Ramachandran, M. Stange, J.C. Walmsley, R. Holmestad, A. Borg and R. Bredesen,Journal of Membrane Science, 2009. **326**(2): p. 572-581.

[17] T.L. Ward and T. Dao,Journal of Membrane Science, 1999. **153**(2): p. 211-231.

[18] G.B. Alessio Caravella, Enrico Drioli.,Chem. Eng. Sci., 2008. **63**: p. 2149-2160.

[19] F.A. Lewis,Academic Press, New York., 1967.

[20] R.C. Hurlbert and J.O. Konecny,The Journal of Chemical Physics, 1961. **34**(2): p. 655-658.

[21] F. Gallucci, A. Basile and E. Drioli,Separation & Purification Reviews, 2007. **36**(2): p. 175 - 202.

[22] J.N. Keuler and L. Lorenzen,Journal of Membrane Science, 2002. **195**(2): p. 203-213.

[23] W.P. Wang, S. Thomas, X.L. Zhang, X.L. Pan, W.S. Yang and G.X. Xiong,Separation and Purification Technology, 2006. **52**(1): p. 177-185.

[24] T.A. Peters, M. Stange, H. Klette and R. Bredesen,Journal of Membrane Science, 2008. **316**(1-2): p. 119-127.

[25] H. Amandusson, L.G. Ekedahl and H. Dannetun,Surface Science, 1999. **442**(2): p. 199-205.

[26] H. Amandusson, L.G. Ekedahl and H. Dannetun,Applied Surface Science, 2000. **153**(4): p. 259-267.
[27] H. Amandusson, L.G. Ekedahl and H. Dannetun,Applied Catalysis A: General, 2001. **217**(1-2): p. 157-164.
[28] A. Unemoto, Kaimai, Atsushi Sato, Kazuhisa, Otake, Takanori, Yashiro, Keiji, Mizusaki, Junichiro,Kawada, Tatsuya, Tsuneki, Tatsuya Shirasaki, Yoshinori Yasuda,Isamu,International Journal of Hydrogen Energy, 2007. **32**(16): p. 4023-4029.
[29] B. Arstad, H. Venvik, H. Klette, J.C. Walmsley, W.M. Tucho, R. Holmestad, A. Holmen and R. Bredesen,Catalysis Today, 2006. **118**(1-2): p. 63-72.
[30] S.H.K. Jung, Katsuki Morooka, Shigeharu Kim, Sang-Done,Journal of Membrane Science, 2000. **170**(1): p. 53-60.
[31] A. Li, W. Liang and R. Hughes,Journal of Membrane Science, 2000. **165**(1): p. 135-141.
[32] F.C.K. Gielens, R. J. J. Duysinx, P. F. J. Tong, H. D. Vorstman, M. A. G. Keurentjes, J. T. F.,Journal of Membrane Science, 2006. **279**(1-2): p. 176-185.
[33] F. Scura, G. Barbieri and E. Drioli,Desalination, 2006. **200**(1-3): p. 239-241.
[34] G.S. Barbieri, F. Lentini, F. De Luca, G. Drioli, E.,Separation and Purification Technology, 2008. **61**(2): p. 217-224.
[35] A.L. Mejdell, Jøndahl, M. T. A. Peters, R. Bredesen, H. J. Venvik,2009.
[36] B.D.C. Morreale, M. V. Howard, B. H. Killmeyer, R. P. Cugini, A. V. Enick, R. M.,Journal of Membrane Science, 2004. **241**(2): p. 219-224.
[37] A. Kulprathipanja, Alptekin, Gökhan O. Falconer, John L. Way, J. Douglas,Journal of Membrane Science, 2005. **254**(1-2): p. 49-62.
[38] Z.Z. Li Yang, Bingjia Yao, Xuhui Gao, Hitoshi Sakai, Tomonori Takahashi,,AIChE Journal, 2006. **52**(8): p. 2783-2791.
[39] H. Amandusson, L.G. Ekedahl and H. Dannetun,Journal of Membrane Science, 2001. **193**(1): p. 35-47.
[40] A.L. Mejdell, H. Klette, A. Ramachandran, A. Borg and R. Bredesen,Journal of Membrane Science, 2008. **307**(1): p. 96-104.
[41] L. Yang, Z. Zhang, X. Gao, Y. Guo, B. Wang, O. Sakai, H. Sakai and T. Takahashi,Journal of Membrane Science, 2005. **252**(1-2): p. 145-154.
[42] F. Roa and J.D. Way,Applied Surface Science, 2005. **240**(1-4): p. 85-104.
[43] J. Shu, B.E.W. Bongondo, B.P.A. Grandjean, A. Adnot and S. Kaliaguine,Surface Science, 1993. **291**(1-2): p. 129-138.
[44] O.M. Løvvik and S.M. Opalka,Surface Science, 2008. **602**(17): p. 2840-2844.
[45] W.M. Tucho, H.J. Venvik, M. Stange, J.C. Walmsley, R. Holmestad, R.Bredesen,Manuscript in preparation. , 2009.
[46] W.M. Tucho, J.C. Walmsley, M. Stange, A. Ramachandran, H.J. Venvik, R.H. Mathiesen, A. Borg, R. Bredesen and R. Holmestad,Manuscript in preparation. , 2009.
[47] James R Brenner, Gaurav Bhagat, Pareen Vasa,Int. J. Oil, Gas and Coal Technology, 2008. **1**(1/2): p. 109.
[48] C. Fitzgerald.,Version 5.12 (Revision B), 2001. Chapter 14(Digital Instruments/Veeco Metrology Group, Inc.).
[49] K. Christmann,Surface Science. In Press, Uncorrected Proof.
[50] H. Conrad, G. Ertl and E.E. Latta,Surface Science, 1974. **41**(2): p. 435-446.

[51] S. Doniach and M. Sunjic,Journal of Physics C: Solid State Physics, 1970. **3**(2): p. 285-291.
[52] S. Aggarwal, A.P. Monga, S.R. Perusse, R. Ramesh, V. Ballarotto, E.D. Williams, B.R. Chalamala, Y. Wei and R.H. Reuss,Science, 2000. **287**(5461): p. 2235-2237.
[53] H.E. Boyer, T.L. Gell (Eds.) 1985: p. pp. 2-19.
[54] P.T. Wouda, M. Schmid, B.E. Nieuwenhuys and P. Varga,Surface Science, 1998. **417**(2-3): p. 292-300.
[55] L.-G. Petersson, H.M. Dannetun, I. Lundstom.,Phys. Rev. B, 1984. **30**: p. 3055.
[56] A. Noordermeer, G.A. Kok and B.E. Nieuwenhuys,Surface Science, 1986. **165**(2-3): p. 375-392.
[57] M. Mulder,Kluwer Academic Publishers, 1997.
[58] D.E. Nanu, W.J. Legerstee, S.W.H. Eijt, W.G. Haije, J.F. Vente, M.G. Tucker and A.J. Böttger,Acta Materialia, 2008. **56**(20): p. 6132-6140.
[59] A.I. Kolesnikov, V.E. Antonov, G. Eckold, M. Prager and J. Tomkinson,Journal of Physics: Condensed Matter, 1993. **5**(38): p. 7075-7086.

Figure captions

Figure 1. Hydrogen flux through the Pd/Ag23wt% membranes as a function of difference in square root of the hydrogen partial pressures at the feed and permeate side before and after heat treatment in (a) N_2/Ar at 300°C (b) N_2/Ar at 400°C (c) N_2/Ar at 450°C and (d) air at 300°C. The dashed/solid lines in each figure with empty/solid symbols represent the hydrogen flux before/after treatments. Triangles refer to samples with thickness 10 μm, squares to 5 μm membranes and circles to 2 μm membranes. The dashed/solid circles with empty/solid circles for (d) refer to 1.5 μm membranes.

Figure 2. AFM images of 2 μm membrane surfaces for the as-grown (2AG) growth surface, after treatment in N_2/Ar at 300°C (2Mi300), at 400°C (2Mi400), at 450°C (2Mi450) and after air exposure at 300°C (1.5Ma300). The membrane surfaces facing the feed side in the membrane reactor are shown to the left, while the membrane surfaces facing the permeate side are shown to the right. Image scan sizes are 1 μm x 1 μm, and the height scale is 20 nm from dark to bright. The respective heat treatments of the membranes are indicated at the bottom of each image. All images have been flattened using a first order polynomial.

Figure 3. AFM images of 5 μm membrane surfaces for the as-grown (5AG) growth surface, after treatment in N_2/Ar at 300°C (5Mi300), at 400°C (5Mi400), at 450°C (5Mi450). The membrane surfaces facing the feed side in the membrane reactor are shown to the left, while the membrane surfaces facing the permeate side are shown to the right. Image scan sizes are 1 μm x 1 μm, and the height scale is 20 nm from dark to bright. The respective heat treatments of the membranes are indicated at the bottom of each image. All images have been flattened using a first order polynomial.

Figure 4. AFM images of 10 μm membrane surfaces for the as-grown (10AG) growth surface, after treatment in N_2/Ar at 300°C (10Mi300), at 400°C (10Mi400), at 450°C (10Mi450) and after air-exposure at 300°C (10Ma300). The membrane surfaces facing the feed side in the membrane reactor are shown to the left, while the membrane surfaces facing the permeate side are shown to the right. Image scan sizes are 1 μm x 1 μm, and the height scale is 20 nm from dark to bright. The respective heat treatments of the membranes are indicated at the bottom of each image. All images have been flattened using a first order polynomial.

Fig 5. Diagram comparing the surface roughness for the feed and permeate sides and permeability of the samples subjected to different thermal treatments, as grouped by thickness category. As permeability for the as-grown membranes was used the average for the corresponding membranes of the same thickness before treatment.

Figure 6. The spectral region covering the Pd3d, Ag3d and C1s core levels for the 2 μm as-grown sample (2AG), the 2 μm membranes thermal treated in N_2/Ar at 300°C, 400°C and 450°C, and the 2Mo300 membrane (bottom to top).

Figure 7. $Pd3d_{5/2}$ core-level spectra for the 2 μm as-grown sample (lower panel), after heat treatment in N_2/Ar at 300°C (mid panel) and for the 2Mo300 membrane (upper panel).

Figure 8. Auger electron spectroscopy depth profile for the 2 μm thin film exposed to pure oxygen at 300°C, with no further hydrogen permeation tested (2Mo300). The elements monitored are Pd (empty circles), Ag (empty squares) and O (empty inverted triangles).

Figure 9. Permeance vs inverse thickness of Pd/Ag 23 wt.% membranes exposed to air at 300˚C in the present work and from References 40 and 45.

Table captions

Table 1 Hydrogen permeation procedures and the gas flow conditions including operating temperature and duration. The samples exposed to the different treatments are listed in the last column.

Table 2 Calculated permeance and permeability before and after thermal treatment in N_2/Ar and air for the 2 μm, 5 μm and 10 μm membranes.

Table 3 Surface roughness and area, for the 2 μm, 5 μm and 10 μm as-grown and tested membranes as determined from AFM measurements.

Table 4 The relative intensities between the Ag3d and Pd3d core level peaks for the different treatments and membrane thicknesses as compared to the Ag/Pd intensity ratio measured for the corresponding as-grown membranes.

Procedure	Feed flow [Nml/in]				Permeate flow [Nml/in]				T [°C]	ΔP [kPa]	Time	Samples
	H_2	N_2	Air	O_2	H_2	Ar	Air	O_2				
Heating		50 100				50 50			20-300	(*)	70min.	All 2 µm All 5µm and 10µm
H_2 stabilization	50 100	50 100				50			300	(*)	24 h	All 2 µm All 5µm and 10µm
Permeance I	200 200 200									5-25 5-43 5-52		All 2 µm All 5µm All 10µm
Cooling in H_2	50				50				300-20			2Mh300F(***) 2Mh300S(***)
N_2/Ar HT (i)		50				50			300 400 450	(*)	3.5 - 4 days	2Mi300, M5i300, 10Mi300 2Mi400, 5Mi400, 10Mi400 2Mi450, 5Mi450, 10Mi450
Air HT (a)			Atm 40 50				Atm 40 50			(**)	3.5- 4 days	1.5Ma300, 5Ma300 10Ma300
O_2 HT (o)				50				50		(*)	3.5- 4 days	2Mo300
Permeance II	200 200 200									5-25 5-43 5-52		2Mi300, 2Mi400, 2Mi450 All 5µm All 10µm
Cooling in N_2/Ar		50 100				50 50			300-20	(*)	70min.	2Mi300, 2Mi400, 2Mi450 All 5µm All 10µm

(*) A slight overpressure (<1.0 kPa) was maintained on the feed side during flow procedures (see text for details).
(**) Heat treatment in air was performed either by introduction of equal flows of dry air from gas bottles (5 and 10 µm membranes), or by opening the feed and permeate gas lines to the ambient (marked as Atm.) after flushing by N_2/Ar.
(***) After H_2 stabilization and permeance I measurements, two of the 2µm membranes were cooled down in hydrogen. F represents the immediate cooling down by opening the housing covered the membrane set-up. S refers the same cooling rate as in N_2/Ar (see text for details).

Table 1

Sample Code	Permeance (mol/m^{2}s Pa$^{0.5}$) x10^{-3}						Permeability (mol.m/m^{2}s Pa$^{0.5}$) x10^{-8}					
	Before treatment			After treatment			Before treatment			After treatment		
	2 µm	5 µm	10 µm	2 µm	5 µm	10 µm	2 µm	5 µm	10 µm	2 µm	5 µm	10 µm
Mi300	3.02	4.58	2.06	7.75	3.07	0.73	0.58	2.75	2.06	1.47	1.84	0.74
Mi400	4.47	4.40	2.46	10.81	3.11	1.60	0.85	2.86	2.88	2.05	2.02	1.88
Mi450	3.31	3.89	2.38	12.21	5.12	2.23	0.63	2.14	2.33	2.32	2.82	2.17
Ma300	8.07(*)	4.48	1.75	15.0	5.07	3.49	1.21	2.76	1.78	2.25	3.19	3.54

(*) The thickness of this sample is 1.5 µm (see text for details).

Table 2

Samples	Roughness (nm)		Surface area x 10^3 (nm^2)	
	Feed / growth	Permeate/ substrate	Feed/growth	Permeate/ substrate
2AG	5.9 ± 0.3	-	5.0 ± 1.0	-
2Mi300	6.3 ± 0.7	3.2 ± 0.1	8.3 ± 3.0	4.3 ± 0.7
2Mi400	7.1 ± 0.6	10.3 ± 0.5	13 ± 4	11± 3
2Mi450	20 ± 4	25 ± 4	36 ± 23	26 ± 16
1.5Ma300	24 ± 3	34 ± 3	24± 14	50 ± 32
5AG	9.6 ± 1.4	-	12 ± 3	-
5Mi300	9.5 ± 1.4	3.6 ± 0.4	12 ± 2	4.0 ± 2.0
5Mi400	9.9± 1.5	6.4 ± 1.4	18 ± 9	6.7 ± 2.2
5Mi450	18 ± 8	9.1 ± 2.4	24 ± 11	12 ± 4
10AG	24± 1	-	95± 24	-
10Mi300	22± 1	2.4 ± 0.4	96± 32	3.4 ± 0.8
10Mi400	25 ± 1	3.3 ± 0.7	96± 33	5.3 ± 2.0
10Mi450	25 ± 3	14.8± 0.5	114.± 31	41 ± 15
10Ma300	21 ± 2	4.0 ± 0.4	158 ± 33	14 ± 5

Table 3

Samples	I(Ag)/I(Pd)		
	2 μm	5 μm	10 μm
Mi300	1.08	-	1.22
Mi400	1.34	-	1.33
Mi450	1.45	1.44	1.34
Ma300	0.89(*)	0.85	1.17
Mo300	0.30	-	-

(*) The thickness of this sample is 1.5 μm (see text for details).

Table 4

(a)

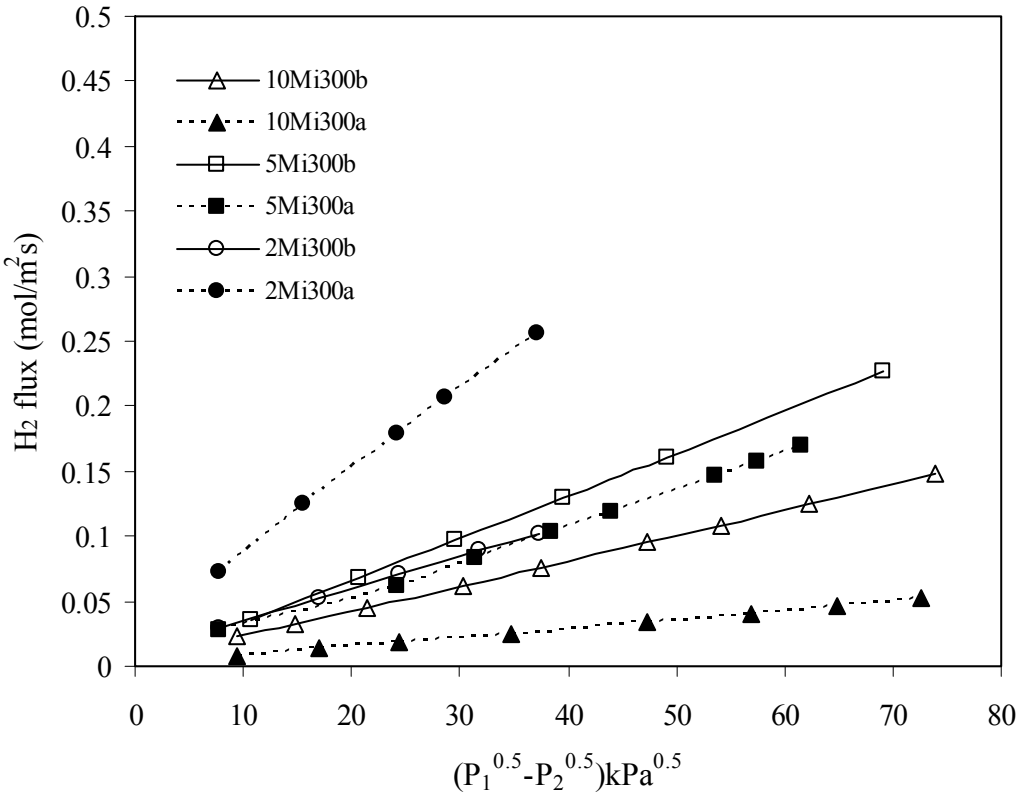
10Mi300b
10Mi300a
5Mi300b
5Mi300a
2Mi300b
2Mi300a
H2 flux (mol/m2s)
(P1 0.5-P2 0.5)kPa0.5
0
0.05
0.1
0.15
0.2
0.25
0.3
0.35
0.4
0.45
0.5
0
10
20
30
40
50
60
70
80

(b)

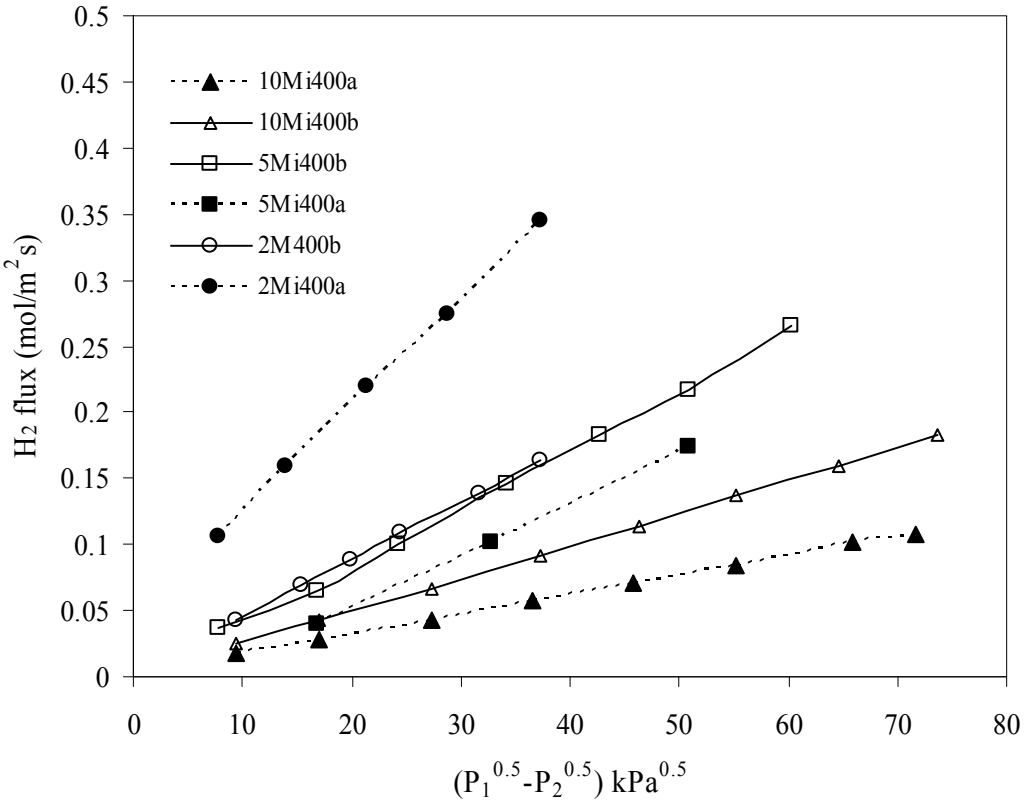
10Mi400a
10Mi400b
5Mi400b
5Mi400a
2M400b
2Mi400a
H2 flux (mol/m2 s)
(P1 0.5-P2 0.5) kPa0.5
0
0.05
0.1
0.15
0.2
0.25
0.3
0.35
0.4
0.45
0.5
0
10
20
30
40
50
60
70
80

(c)

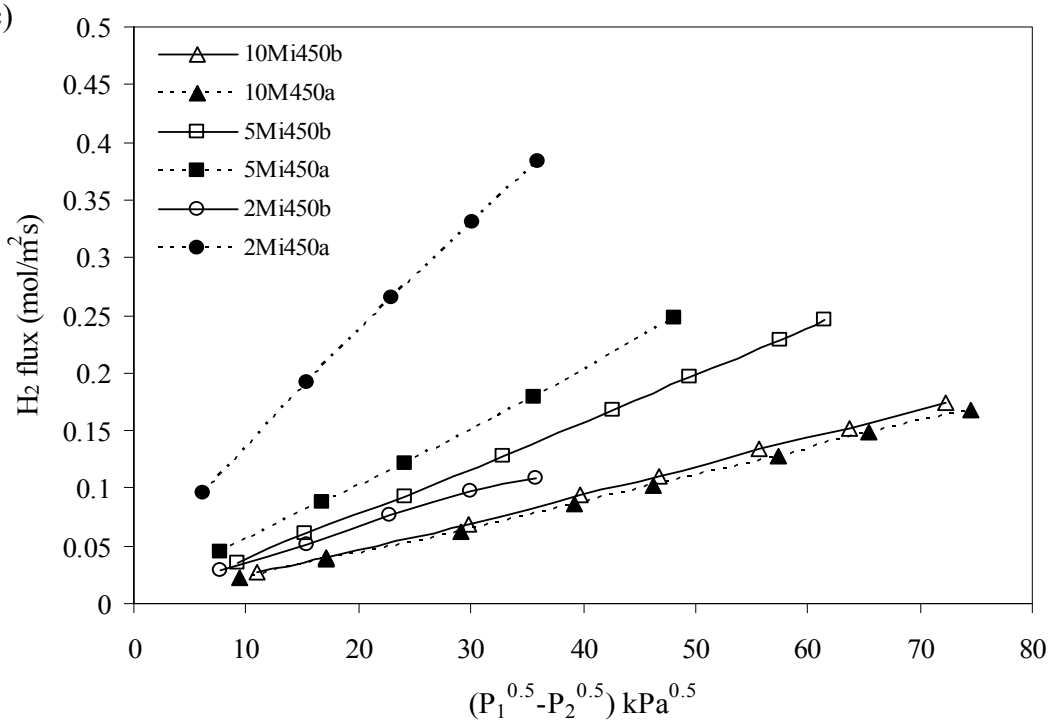
10Mi450b
10M450a
5Mi450b
5Mi450a
2Mi450b
2Mi450a
H2 flux (mol/m2s)
(P1 0.5-P2 0.5) kPa0.5
0
0.05
0.1
0.15
0.2
0.25
0.3
0.35
0.4
0.45
0.5
0
10
20
30
40
50
60
70
80

(d)

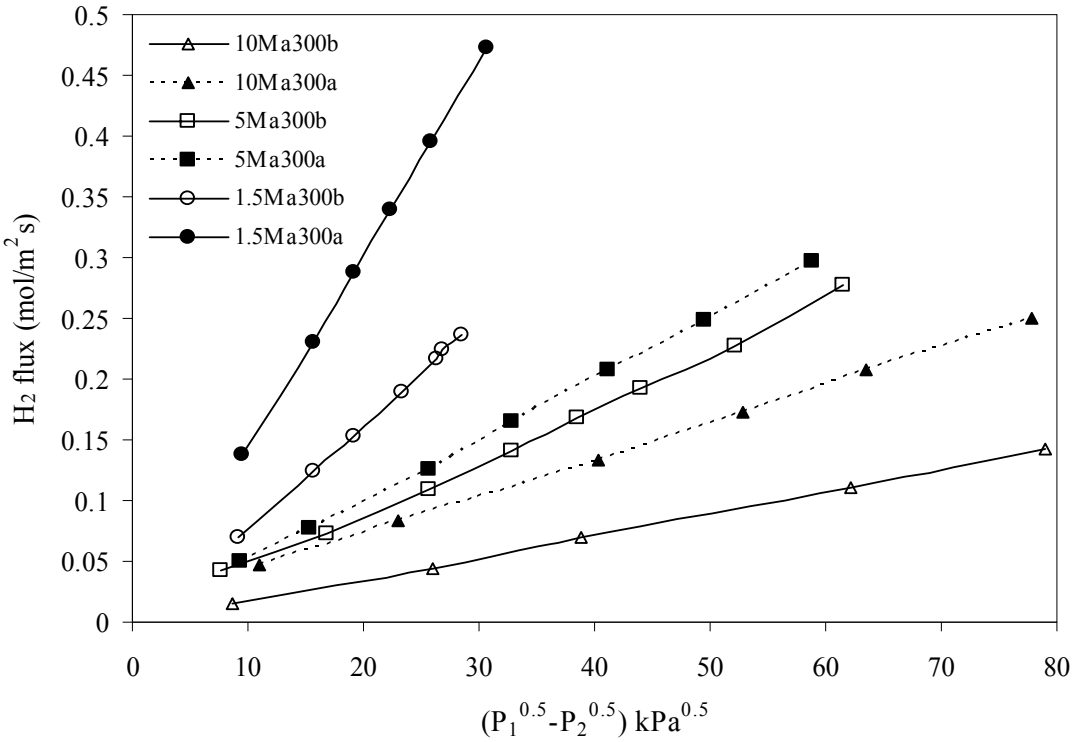
10Ma300b
10Ma300a
5Ma300b
5Ma300a
1.5Ma300b
1.5Ma300a
H2 flux (mol/m2 s)
(P1 0.5-P2 0.5) kPa0.5
0
0.05
0.1
0.15
0.2
0.25
0.3
0.35
0.4
0.45
0.5
0
10
20
30
40
50
60
70
80

Fig.1

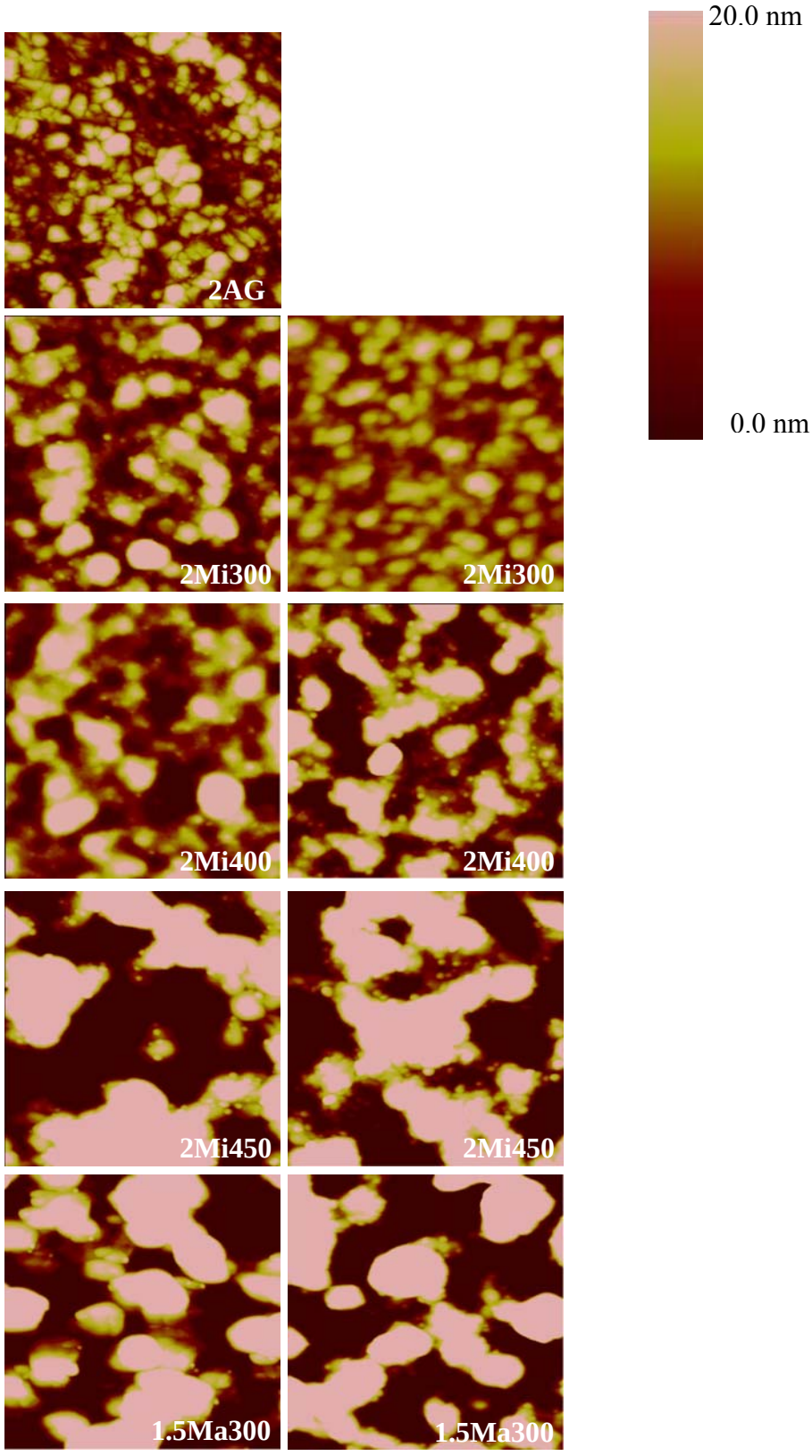
20.0 nm
0.0 nm
2AG
2Mi300
2Mi300
2Mi400
2Mi400
2Mi450
2Mi450
1.5Ma300
1.5Ma300

Fig. 2

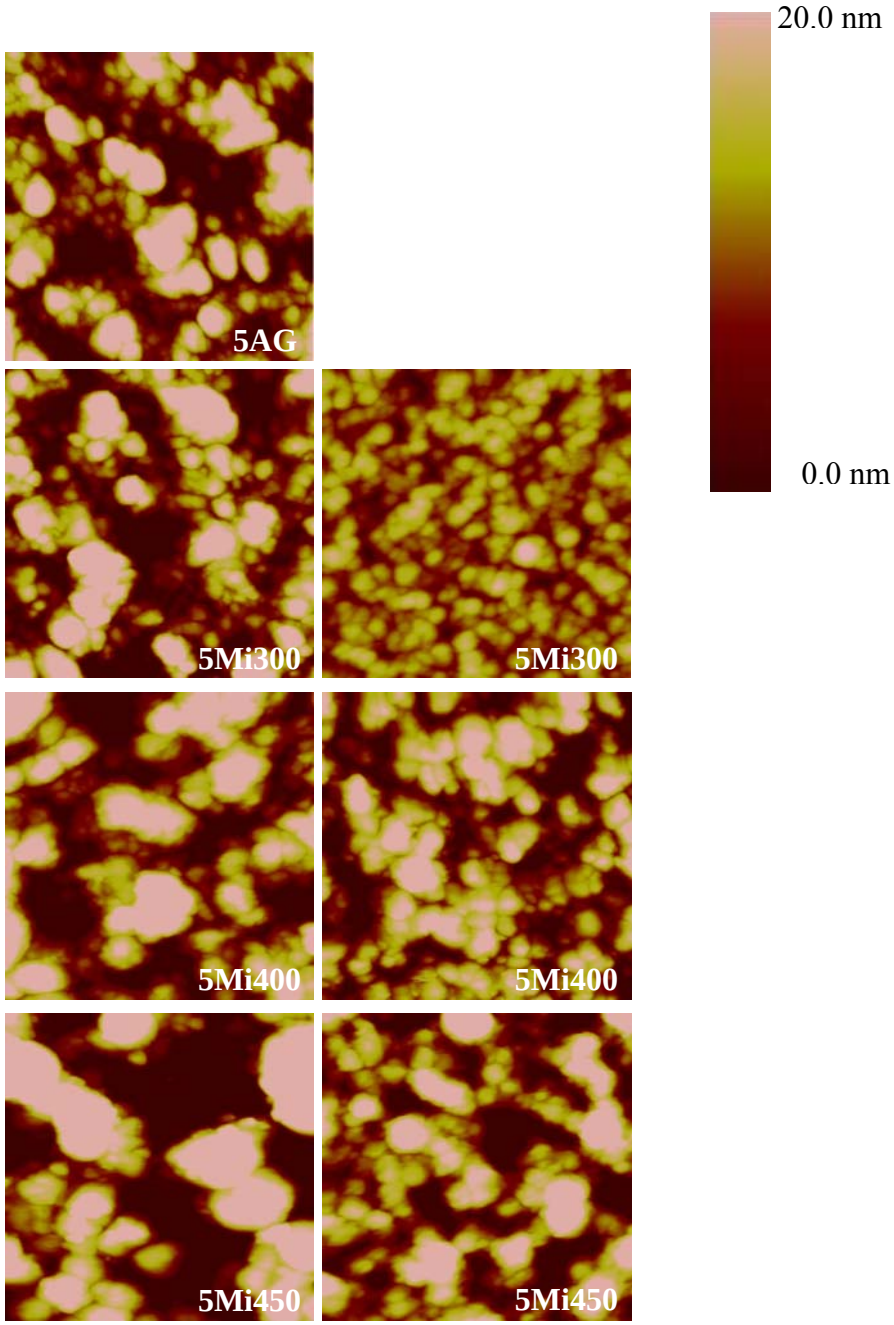

Fig. 3

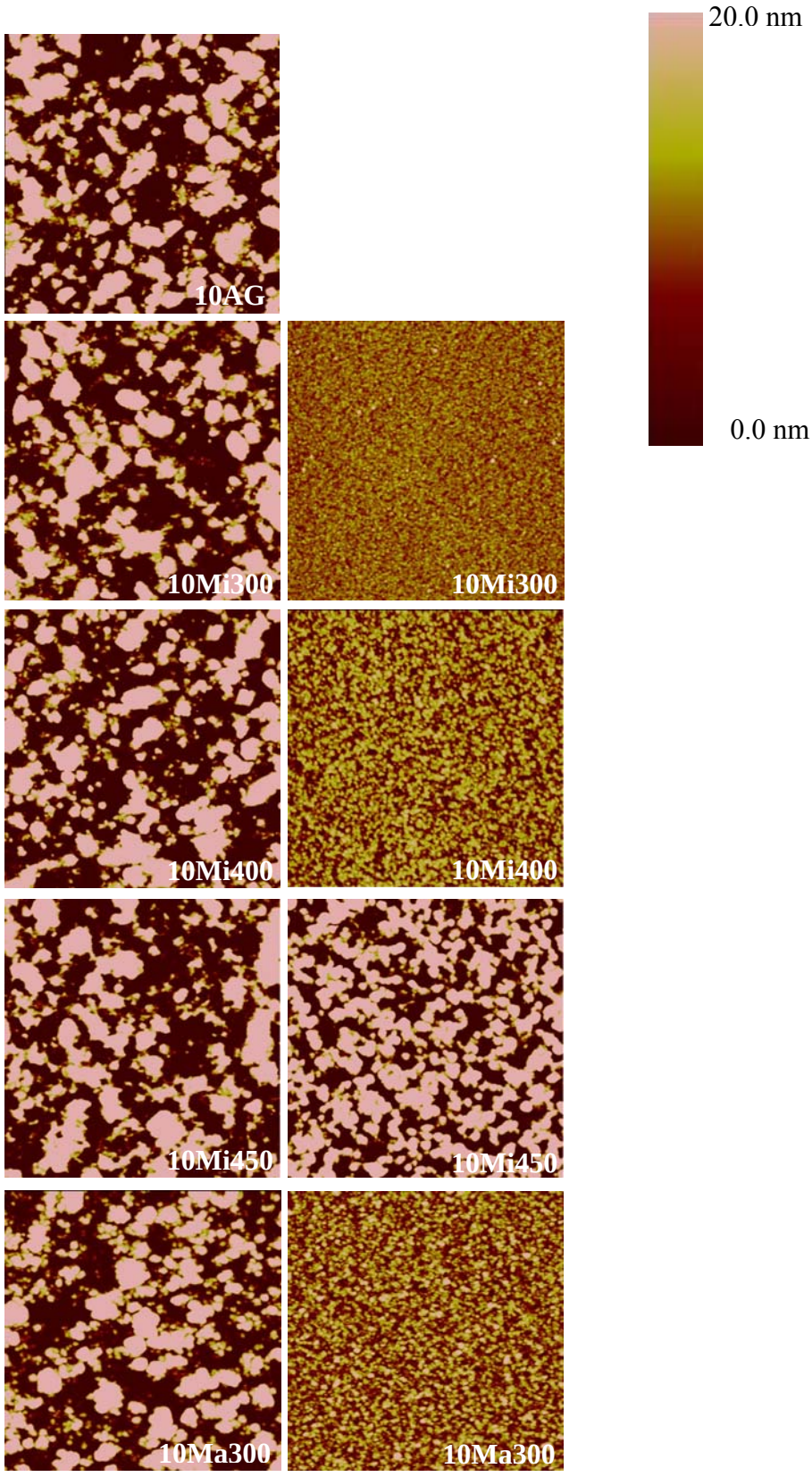
20.0 nm
0.0 nm
10AG
10Mi300
10Mi300
10Mi400
10Mi400
10Mi450
10Mi450
10Ma300
10Ma300

Fig. 4

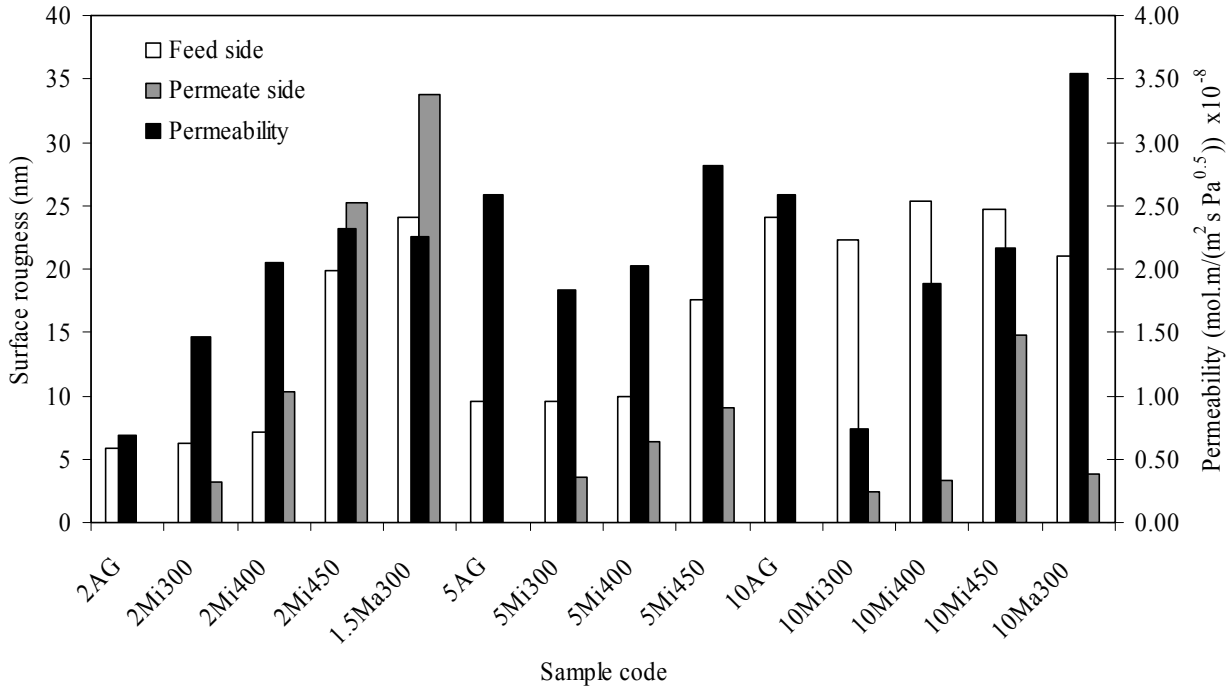
Feed side
Permeate side
Permeability
Surface rougness (nm)
Permeability (mol.m/(m2 s Pa0.5)) x10-8
Sample code
2AG
2Mi300
2Mi400
2Mi450
1.5Ma300
5AG
5Mi300
5Mi400
5Mi450
10AG
10Mi300
10Mi400
10Mi450
10Ma300

Fig. 5

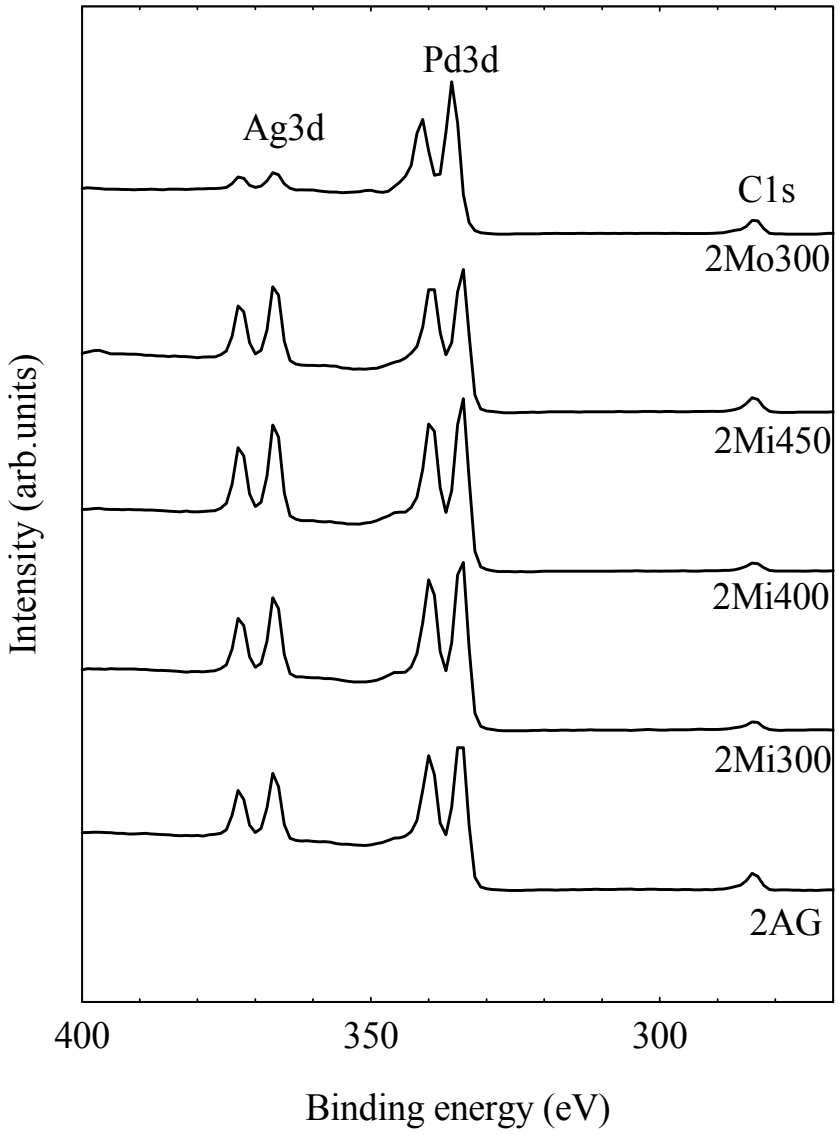
Pd3d
Ag3d
C1s
2Mo300
2Mi450
2Mi400
2Mi300
2AG
Intensity (arb.units)
400
350
300
Binding energy (eV)

Fig. 6

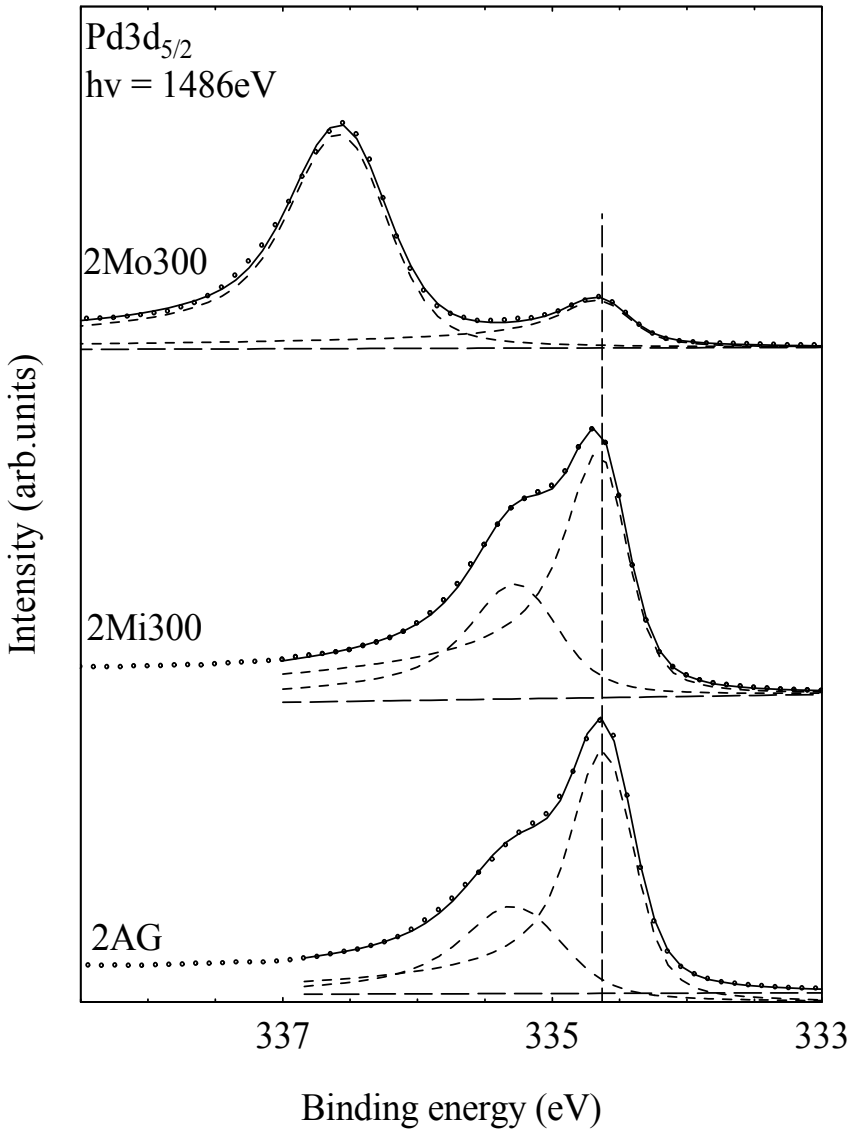
Pd3d5/2
hv = 1486eV
2Mo300
2Mi300
2AG
Intensity (arb.units)
337
335
333
Binding energy (eV)

Fig. 7

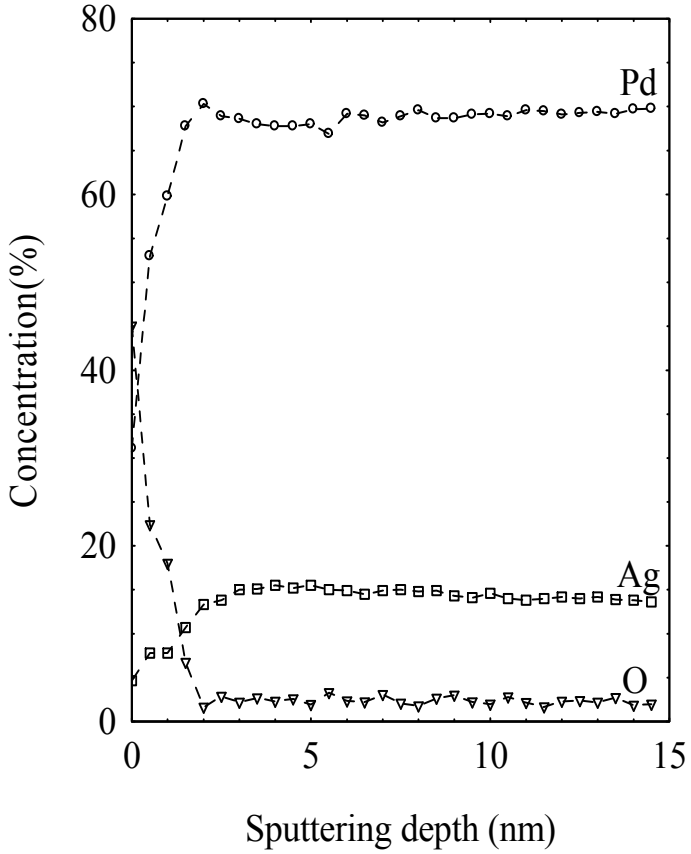
80
60
40
20
0
Concentration(%)
Pd
Ag
O
0
5
10
15
Sputtering depth (nm)

Fig. 8

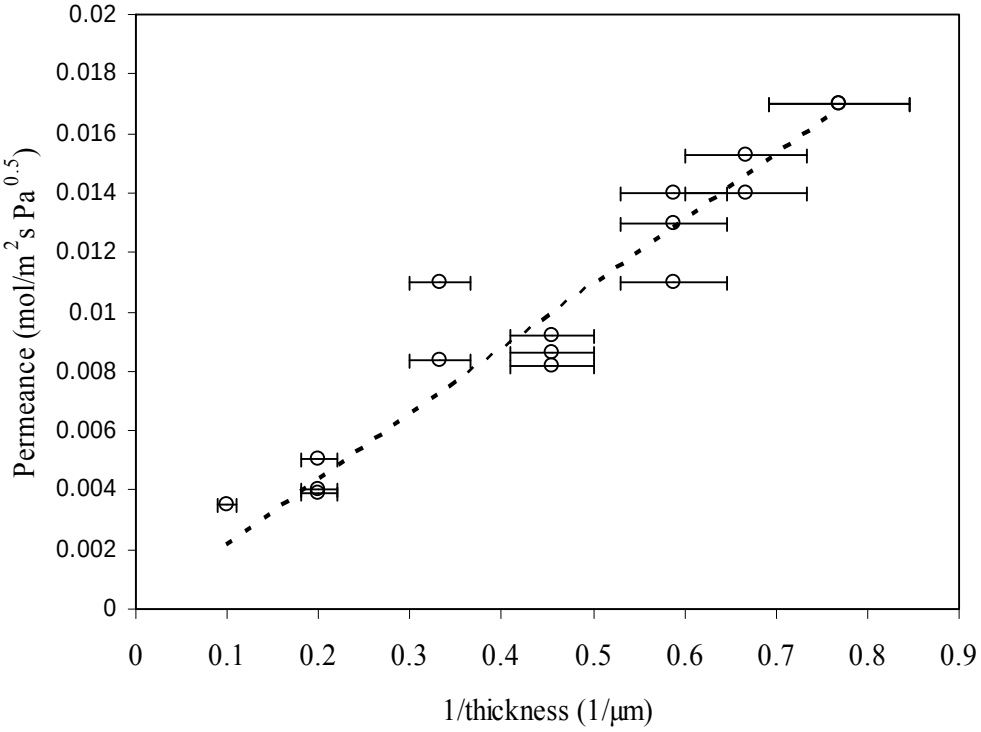
0.02
0.018
0.016
0.014
0.012
0.01
0.008
0.006
0.004
0.002
0
Permeance (mol/m2 s Pa0.5)
0
0.1
0.2
0.3
0.4
0.5
0.6
0.7
0.8
0.9
1/thickness (1/μm)

Fig. 9

Paper III

Thin Pd-23%Ag/stainless steel composite membranes: Long-term stability, life-time estimation and post-process characterisation

T.A. Peters, W.M. Tucho, A. Ramachandran, M. Stange, J.C. Walmsley, R. Holmestad, A. Borg, and R. Bredesen

Journal of Membrane Science, 326 (2009) 572

Journal of Membrane Science 326 (2009) 572–581

Contents lists available at ScienceDirect

Journal of Membrane Science

journal homepage: www.elsevier.com/locate/memsci

Thin Pd–23%Ag/stainless steel composite membranes: Long-term stability, life-time estimation and post-process characterisation

T.A. Peters[a], W.M. Tucho[b], A. Ramachandran[b], M. Stange[a], J.C. Walmsley[c], R. Holmestad[b], A. Borg[b], R. Bredesen[a,*]

[a] SINTEF Materials and Chemistry, N-0314 Oslo, Norway
[b] Department of Physics, Norwegian University of Science and Technology (NTNU), N-7491 Trondheim, Norway
[c] SINTEF Materials and Chemistry, N-7465 Trondheim, Norway

ARTICLE INFO

Article history:
Received 8 September 2008
Received in revised form 17 October 2008
Accepted 27 October 2008
Available online 8 November 2008

Keywords:
Palladium–silver membrane
Magnetron sputtering
Hydrogen flux
Membrane stability
Life-time
Hydrogen selective membrane
Microstructure
Grain growth
Segregation

ABSTRACT

The long-term stability of Pd–23%Ag/stainless steel composite membranes has been examined in H_2/N_2 mixtures as a function of both temperature and feed pressure. During continuous operation, the membrane shows a good stability at 400 °C while the N_2 leakage increases very slowly at a temperature of 450 °C (P_{feed} = 10 bar). After 100 days of operation (P_{feed} = 5–20 bar, T = 350–450 °C), the N_2 permeance equals 7.0×10^{-9} mol m^{-2} s^{-1} Pa^{-1}, which indicates that the H_2/N_2 permselectivity still lies around 500, based on a H_2 permeance equal to 3.0×10^{-6} mol m^{-2} s^{-1} Pa^{-1}. Despite the generation of small pinholes, a membrane life-time of several (2–3) years ($T \leq 425$ °C) is estimated for the experimental conditions employed based on long-term stability tests over 100 days. Post-process characterisation shows a considerable grain growth and micro-strain relaxation in the Pd–23%Ag membrane after the prolonged permeation experiment. Changes in surface area are relatively small. In addition, segregation of Ag to the membrane surfaces is observed. The formation of pinholes is identified as the main source for the increased N_2 leakage during testing at higher temperature.

1. Introduction

Hydrogen selective membranes are interesting candidates to be applied in water gas shift (WGS) membrane reactors to achieve CO_2 capture by the so-called pre-combustion decarbonisation in large-scale power generation or hydrogen production. Commercial membranes are available in the form of tubes or foils, which are relatively thick (15–20 μm). The hydrogen flux, being inversely proportional to the thickness of the membrane, is thus too low for sufficient cost efficiency in most applications. For most practical use, it is therefore necessary to develop membranes with reduced thickness of the Pd layer. In the last decade, a substantial research effort has been carried out to achieve higher fluxes by depositing thin layers of Pd or Pd alloys on porous supports, like ceramics or stainless steel. The most common methods to fabricate these composite membranes include electroless plating [1,2], chemical vapour deposition [3,4], physical vapour deposition [5], and sputtering [6–9]. In most cases, the thin Pd or Pd alloy layer is prepared directly on the surface or inside the pores of the support [3,10]. Depending on the method, a lower thickness limit exists for which a dense layer can be obtained. This thickness limit increases with increasing surface roughness and pore size in the support's top layer [6,11]. Differently from previous efforts we are using a two-step process where a defect free Pd-alloy membrane is first prepared by sputtering deposition onto the 'perfect surface' of a silicon wafer [12,13]. In the second step the membrane is removed from the wafer and transferred to a porous stainless steel support. This allows the preparation of very thin (~2 μm) membranes supported on macroporous substrates. Moreover, the magnetron sputtering technique allows for the preparation of homogeneous films using multi-component targets, where thickness and composition control using electroless plating is more cumbersome [8].

The reduced membrane thickness, however, challenges membrane stability. Possible causes of stability problems are poor matching of thermal and chemical expansion coefficients between the support material and membrane layer, possible inter-metal diffusion between the support and membrane layer, microstructural changes due to grain growth, segregation, or reaction with components in the gas mixture [14,15]. Whereas, ceramic supports, such as, *e.g.* pure alumina, are not believed to cause significant

* Corresponding author.
E-mail address: Rune.Bredesen@sintef.no (R. Bredesen).

0376-7388/$ – see front matter © 2008 Elsevier B.V. All rights reserved.
doi:10.1016/j.memsci.2008.10.053

inter-diffusion problems, stress generated due to the poor matching of the thermal expansion coefficients between Pd and alumina may cause loss of attachment, flaking-off and cracking [14]. Less interfacial stress is generated for thinner Pd layers [16,17], particularly on porous steel supports which have a thermal expansion coefficient close to that of palladium [17]. However, inter-diffusion of metals between membrane and porous metal support occurring at high temperature deteriorates the performance of the membrane. To reduce the problem, barrier layers of TiN [18], oxides [19–21] or porous Pd–Ag [22,23] are coated on the metal support. For example, membranes with a porous Pd–Ag composite layer prepared by consecutive deposition of Pd and Ag layers have been stable under hydrogen permeation conditions for over 1400 h at temperatures exceeding 500 °C [24]. The many stress generating effects, as well as the reactive components the membrane is exposed to, probably cause frequently observed microstructural changes in thin Pd-based membranes [25]. Further optimisation of the performance of thin composite membranes requires better understanding of these features.

In a recent article, we have reported the preparation and transport properties of tubular supported Pd–23%Ag membranes [13]. The effects on the hydrogen flux caused by hydrogen dilution, concentration polarization due to mass transfer limitations, and adsorption effects, were particularly addressed. For these highly selective ~2 μm thick Pd–23%Ag composite membranes, a H_2 flux reaching ~1223 mL cm^{-2} min^{-1} at 25 bar differential pressure was achieved [13]. This corresponds to a permeance of 6.4×10^{-3} mol m^{-2} s^{-1} Pa$^{-0.5}$. The permeance in mixtures and WGS conditions, however, was considerably reduced due to concentration polarisation and CO surface poisoning. In the present work, we have investigated the long-term stability of the supported membranes as a function of temperature and pressure over a period for 100 days. An intermetal diffusion barrier was applied on top of the membrane support. Thorough material characterisation has been performed employing different techniques, including atomic force microscopy (AFM), scanning electron microscopy (SEM), conventional transmission electron microscopy (TEM), scanning transmission electron microscopy/energy dispersive spectroscopy (STEM/EDS), X-ray diffraction (XRD), X-ray photoelectron spectroscopy (XPS), and Auger electron spectroscopy (AES). In addition, the life-time of the supported membranes has been estimated based on the long-term test over 100 days.

2. Experimental

2.1. Pd–23%Ag film preparation

Unsupported palladium alloy films were prepared by sputtering using a CVC 601 magnetron sputtering apparatus. The films were sputtered from a Pd–23%Ag target onto polished silicon single crystal substrates [12]. The vacuum chamber was pumped down to ~10^{-6} T before introducing the Ar sputtering gas into the system. Using a sputtering time of around 2 h a final nominal film thickness of ~2.6 μm was obtained.

2.2. Membrane preparation

After sputtering, the palladium film was removed manually from the silicon substrate and transferred to a 4 cm long tubular macroporous stainless steel substrate. During the application, the Pd–23%Ag film was wrapped along the stainless tube. An overlap region provided sealing between subsequent films. The Pd film–Si substrate interface side of the as-grown film served as the feed side and the Pd film growth side as the permeate side of the membrane during testing. Sealing was obtained by clamping. The tubular porous 316 L stainless steel (PSS®) Accusep™ support was supplied by PALL Corporation, USA. It has an average pore size of 2 μm. The outer diameter and wall thickness of the support were 11.85 and 0.48 mm, respectively. An intermetallic diffusion barrier was deposited on the porous stainless steel prior to application of the Pd film. The effective surface area of the membrane was ca. 6.8 cm^2. Due to confidentiality we are unfortunately not able to reveal more information concerning the properties of the membrane support.

2.3. Hydrogen permeation measurements

The tubular-supported palladium membrane was tested in a unit designed and constructed for high-pressure membrane permeability testing. The supported palladium membrane was placed inside a 316 L stainless steel module (inside diameter 19 mm). The feed and permeate gas flows were controlled by automated mass flow controllers (Bronkhorst High-Tech). The long-term stability of the membranes was investigated at low feed flow rates, *i.e.* high H_2 recovery, in order to prevent consumption of large quantities of gas. The membrane was heated from room temperature to 300 °C at a rate of 2 °C/min in a N_2/Ar atmosphere before H_2 was introduced. The pressure at the feed side of the membrane was controlled by a back pressure controller (Bronkhorst High-Tech). The gases at the feed and permeate side were analysed by a gas chromatograph (GC) (Varian Inc., CP-4900). Fluxes were calculated from the measured permeate H_2 concentration and the calibrated flow of Ar sweep gas. A counter-current sweep was applied. The permeate side of the membrane was kept at atmospheric pressure during the whole experiment.

2.4. Membrane characterization

After the permeation experiments, pieces of the Pd–23%Ag membrane were removed from the tubular support, and made available for microstructure, composition and other investigations. The surface topography on larger length scales was characterized with an optical microscope, OLYMPUS BX60, while detailed changes in the surface topography of the exposed membranes were examined by atomic force microscopy (AFM). A Multimode SPM from Digital Instruments was used in Tapping mode, and the instrument software was used to estimate the surface roughness and surface area of both the feed and permeate side membrane surfaces. For comparison, as-grown samples were examined after they were pulled off from the silicon wafer. A field emission scanning electron microscope (SEM), Hitachi S-43000 SE, was used to study morphology of the surfaces. Transmission electron microscopy (TEM) (Philips CM 30) and scanning transmission electron microscopy/energy dispersive spectroscopy (STEM/EDS) (JEOL 2010F) were used for bulk microstructure and composition analysis, respectively. Both TEMs were operated at 200 kV voltage. X-ray diffraction (XRD) experiments were performed at the Swiss-Norwegian Beamline, station B (SNBL B) of the European Synchrotron Radiation Facility (ESRF) in Grenoble, France. Since the grain structures of the membranes are different across the two surfaces, the samples were scanned from both surfaces, one at a time. Size and strain broadening effects were extracted from the diffraction peak profile, assuming Lorentzian line shape for the former and a Gaussian component for the later [26]. Details of the XRD experiment and the microstructure analysis will be described in the forthcoming paper on the microstructure of thin, freestanding Pd–23%Ag membranes [27]. The surface chemical compositional analysis was performed by X-ray photoelectron spectroscopy (XPS) with a KRATOS AXIS ULTRA^{DLD} spectrometer using monochromatic Al Kα radiation ($h\nu$ = 1486.6 eV). The pass energy for the wide scan and the element scan was 160 and 20 eV, respectively, the latter

yielding an overall energy resolution of 330 meV. Depth profiling of the chemical composition of the membrane was performed by Auger electron spectroscopy (AES) with a JEOL instrumental unit, JAMP 9500F, field emission Auger microprobe. The spectral energy resolution for the AES measurement was 0.6% of the kinetic energy. The electron beam voltage and current during AES measurement were 10 keV and 2.73×10^{-9} A, respectively. An ion energy of 500 eV was used during sputtering, which was performed in steps of 15 s. The sputtering rate was calibrated with the as-grown Pd–Ag membranes and found to be 2 nm/min.

3. Results and discussion

3.1. Long-term stability

The long-term stability of the supported Pd–23%Ag membranes was monitored over a period of 100 days using a feed gas mixture of 50% H_2 + 50% N_2. The H_2 and N_2 fluxes were measured while the temperature and pressure were systematically varied between 350 and 450 °C and 5–20 bar, respectively. The observed fluxes of H_2 and N_2 as a function of process time under different operating conditions are given in Fig. 1.

Initially, a stable membrane performance was obtained by applying a feed pressure up to 10 bar and temperature up to 400 °C during more than 1 month, as shown in Fig. 1. However, after the subsequent increase in operation temperature to 450 °C, the nitrogen leakage flux increases drastically. The decrease in operating temperature to 400 °C did not stabilize the N_2 leakage. Similarly, the rate of N_2 leakage was increased by increasing the feed pressure from 10 to 20 bar. By subsequently decreasing the pressure down to 5 bar and temperature down to 375 °C, the nitrogen leakage flux stabilises again. Most surprisingly, however, the nitrogen leakage flux is found to increase fairly linear as a function of time at constant temperature and pressure. Similar observations were reported by Guazzone and Ma for helium leakage through Pd composite membranes [28]. Based on experimental results, they identified pinhole formation mechanisms. They found that the formation and growth of pinholes started at about 400–450 °C. According to this investigation, the formation of new and small pinholes can increase the leak rate as a function of time at a given temperature (450 °C and above). The membrane in this work showed similar leak behaviour (Fig. 1) in the same temperature range as observed by Guazzone and Ma. They propose that leak formation and growth are related to inhomogeneous sintering and that pinhole formation is more likely at temperatures above 400 °C.

After operating the membrane for 100 days at T = 350–450 °C and P_{feed} = 5–20 bar, the N_2 permeance had increased from its initial value of 4×10^{-10} mol m^{-2} s^{-1} Pa^{-1} to a maximum of 7×10^{-9} mol m^{-2} s^{-1} Pa^{-1}, which shows that the membrane is still highly selective towards H_2. The H_2/N_2 permselectivity still lies around 500, based on a H_2 permeance equal to 3.0×10^{-6} mol m^{-2} s^{-1} Pa^{-1}. To our knowledge this is the first time that the stability of thin (<5 μm) supported Pd-alloy membranes is examined over a prolonged period (100 days) at a relative high feed pressure (10 bar). Recent data reported by Matzakos show stable operation under actual steam-reforming conditions for 6000 h using a composite porous stainless steel palladium membrane [29,30]. However, no information on the membrane thickness and operating pressure was given. Recently, Tosti et al., have published stability data obtained over a period of 12 months using thin wall permeator tubes produced by diffusion welding of Pd–Ag foils [31]. Although these rolled membranes are relatively thick (125 μm) for practical use, they showed complete hydrogen selectivity for the whole period. The applied feed pressure, however, was only up to 2 bar.

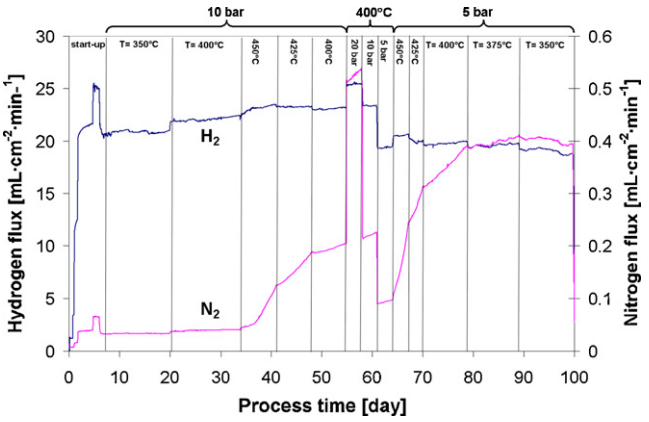

Fig. 1. Long-term stability showing the H_2 and N_2 fluxes through the membrane as a function of time, temperature and pressure. Feed mixture: 50% H_2 + 50% N_2. Note the large difference in scale of H_2 and N_2 flux.

3.2. Life-time estimation

For deployment of these Pd membranes in CO_2 capture processes, to achieve pre-combustion decarbonisation in large-scale power generation or hydrogen production, preliminary process calculations have suggested a needed H_2/CO_2 separation factor of 100 [32]. In terms of H_2 to N_2 permselectivity, this would correspond to a value of around 400 due to the absence of mass transfer and surface effects on the hydrogen flux while measuring in pure gases, which causes the H_2 flux to drop with a factor of around 4 [13]. Thus, based on the results obtained in this work, and the assumption that the membranes are maintained in operation until the H_2/N_2 permselectivity drops below a value of 400, one may estimate the membrane operating life-time. In Tables 1 and 2 we have estimated

Table 1
Increase in N_2 leakage flux and life-time estimate as a function of temperature. Feed mixture: 50% H_2 + 50% N_2; Feed pressure = 10 bar.

Temperature [°C]	dN_2 flux [mL cm^{-2} min^{-1} week^{-1}]	Pure H_2 flux [mL cm^{-2} min^{-1}]	Max. N_2 flux [mL cm^{-2} min^{-1}]	Life-time [years]
450	0.083	1400	3.5	0.8
425	0.056	1200	3	1.0
400	0.019	1000	2.5	2.5

Table 2
Increase in N_2 leakage flux and life-time estimate as a function of feed pressure. Feed mixture: 50% H_2 + 50% N_2; T = 400 °C.

Feed pressure [bar]	dN_2 flux [mL cm^{-2} min^{-1} week^{-1}]	Pure H_2 flux [mL cm^{-2} min^{-1}]	Max. N_2 flux [mL cm^{-2} min^{-1}]	Life-time [years]
20	0.061	2000	5	1.6
10	0.028	1200	3	2.1
5	0.015	700	1.75	2.2

the time period to reach H_2/N_2 permselectivity of 400 based on the observed linear increase in N_2 permeance.

From Table 1 it can be seen that a membrane life-time of 2.5 years is estimated if the membrane is operated at 400 °C, even after the initial onset of nitrogen flux increase caused during membrane operation at 450 °C. This value matches very well with the life-time of commercially available low/medium temperature WGS catalysts. Operating the membrane at temperatures higher than 400 °C, however, gives a rapid decrease in membrane life-time. Therefore, thicker Pd–23%Ag membranes (>2 μm), or alternatively other Pd-alloy compositions, for which temperature stability is enhanced, are needed above 400 °C. Although the increase in nitrogen flux is enhanced at increasing pressure, this does not have a dramatic influence on the expected life-time of the membrane as the hydrogen flux is also increased due to the larger hydrogen partial pressure difference over the membrane. At 400 °C a membrane life-time of 1.6 and 2.2 years is estimated at operating pressures of 20 and 5 bar, respectively. The results in Tables 1 and 2 suggest that thermal activation is more important than mechanical stress in the temperature–pressure region investigated. As negative effects due to coking, carbon intrusion, and adsorption have been observed employing Pd-based membranes operating in carbon containing atmospheres [15], stability experiments need to be performed in WGS mixtures as well. Such work is in progress.

For the composite Pd–23%Ag membrane, unselective N_2 transport is caused by one or several of the following reasons:

(i) Leakage through the Pd–23%Ag film overlap region.
(ii) Leakage through the sealing of the membrane, or module.
(iii) Leakage through pinholes present in the Pd–23%Ag film.

Initially, a minor leakage is present in the membrane (nitrogen permeance equals 4×10^{-10} mol m^{-2} s^{-1} Pa^{-1}), which is probably caused by a slight leakage in either the overlap or the sealing region. This conclusion is based on the fact that the as-grown Pd–23%Ag film is free from pinholes and microcracks as determined by hydrogen permeation measurements and material characterization of numerous self-standing Pd–23%Ag membranes [33]. As addressed in the following, a plausible explanation for the increase in N_2 flux in our case is therefore pinhole formation during operation. Leak appearance through the sealing, however, cannot be excluded.

3.3. Post-process characterisation

In order to investigate the membrane material stability and the sources of leakage, a thorough material characterization was performed after removing the Pd–23%Ag membrane from the PSS support. The microstructure of the membrane, changes in surface topography, chemical composition, both at the surface and in the bulk, and mechanical defects as possible sources of leakage were studied.

3.3.1. SEM and optical investigations

Optical and SEM micrographs of the feed and permeate surface topography of the tested membrane are shown in Figs. 2 and 3, respectively. The topography of the feed surface shown in Fig. 2(a) and (b) contains some bulged areas which are almost uniformly

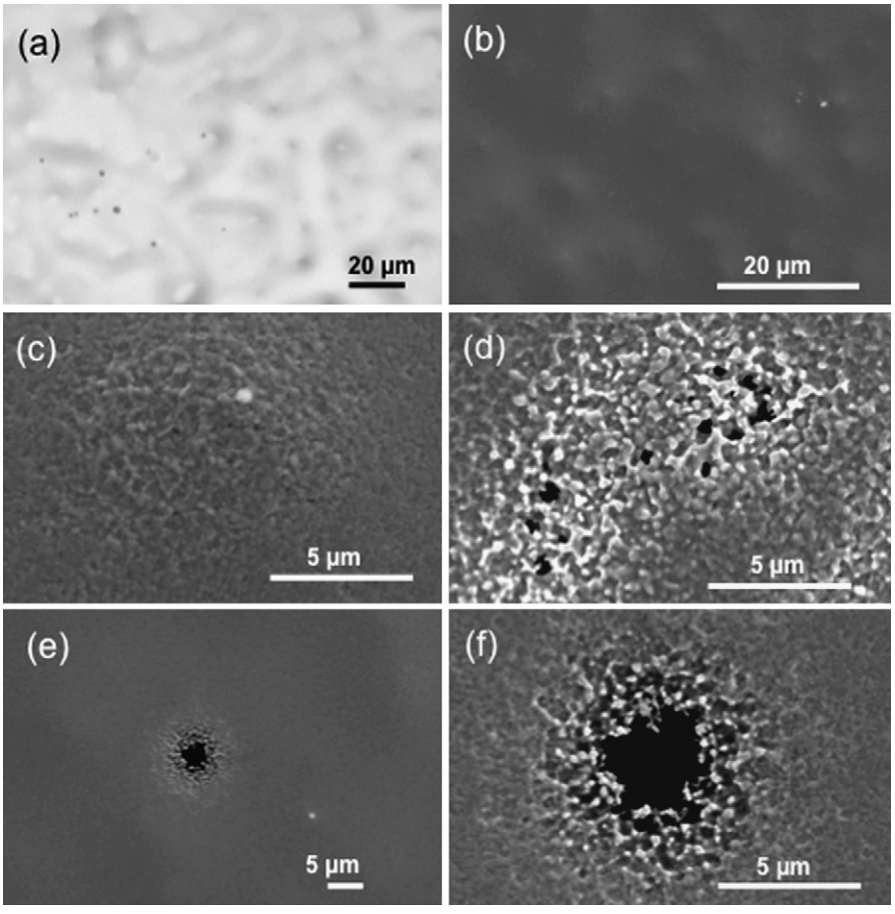

Fig. 2. Optical and SEM images of the feed surface of the tested membrane: (a) optical image of the surface topography (b) SEM image of the surface topography (c) magnified SEM image of one of the bulged site shown in (b), and (d)–(f) show SEM images of pinholes at different magnifications.

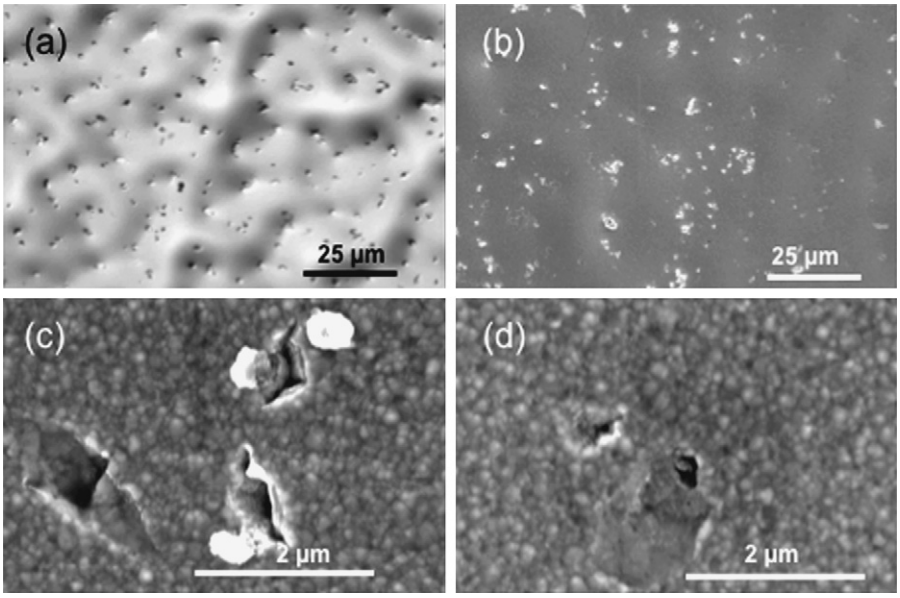

Fig. 3. Optical and SEM image of the permeate surface of the tested membrane: (a) optical image of the surface topography (b) SEM image of the surface topography. (c) and (d) show magnified SEM images of the imprints shown in part (a) and (b).

spread throughout the membrane. These bulged areas have been formed on the membrane surface due to a high and uneven stress distribution, while following the surface topography of the porous support during the high-pressure operation. These bulged areas on the membrane surface are seemingly prone to pinhole formation since the observed pinholes appeared at such sites. A magnified image from one of these areas is shown in Fig. 2(c). Fig. 2(d) displays an example of nano-sized pinholes, whereas, Fig. 2(e) displays a micro-sized pinhole. A magnified image of Fig. 2(e) is shown in Fig. 2(f). This pinhole has a diameter of about 5 μm. Pinholes at this size were very rarely found in the membrane. It is likely that an inhomogeneous stress distribution, originating from hydrogen dissolution, mismatch in thermal expansion coefficient, and mechanical pressure, causes some areas to reach above their local critical mechanical strength. The elevated operation temperature allows the material to release the excess energy through, *e.g.*, processes as plastic deformation, grain sliding and creep, which subsequently leads to microstructural changes and pinhole formation [25].

Imprints originating from the contact with the support are identified on the permeate surface, see Fig. 3. Fig. 3(c) and (d) show finer details of some of these imprints, identified as scratches or microcracks. These defects are believed to occur when the foil was pressed against the surface of the porous support during the high-pressure operation. By comparing Figs. 2(a) and 3(a), it should be noted that there is a much larger number of imprints at the permeate side as compared to pits observed at the feed side of the membrane, confirming that only a few μm-size pinholes were present in the membrane. Additionally, some material arising from the intermetal diffusion barrier is observed; see Fig. 3(c). According to the TEM investigation, no evidence has been found that these imprints are penetrating throughout the entire thickness of the membrane.

3.3.2. TEM investigations

TEM samples in cross-section geometry were used to examine the changes in microstructure of the tested membrane in relation to the as-grown film. The micrographs in Figs. 4 and 5 show the growth and permeate surfaces of as-grown and tested samples, respectively. The grains are columnar near the growth surface, in contrast to the more spherical grains observed at the substrate surface in the as-grown film, as seen in Figs. 4(a) and 5(a). In Figs. 4(b) and 5(b) it is clearly shown that the tested membrane developed significant grain growth relative to the as-grown sample. This is in agreement with previous observations of similar free-standing membranes [25].

An example of grain development from very fine to much bigger grains than before heat treatment is given by the dark field TEM images shown in Fig. 5(a) and (b). The dark field images in Fig. 5 are formed by electrons scattered into a section of a diffraction ring from the polycrystalline membrane. Different grains show bright contrast according to how close their orientation is to a strong diffraction condition. Contrast variations in the grain are due to strain and the presence of defects such as dislocations. In Fig. 5(a), individual fine grains close to the original membrane/wafer interface can be seen, whereas Fig. 5(b) shows a higher magnification of the much coarser-gained region in the tested membrane. The grain marked "G" is close to a diffraction condition. Other grains in the field of view are not showing strong diffraction contrast. The grain marked 'G' in Fig. 5(b) has a diameter of 200 nm as compared to the tiny grains of the as-grown sample with an average grain size of ~10–20 nm near the surface shown in Fig. 5(a). This substantial grain growth is most likely attributed to the effects of temperature. The measured thickness, grain size and microstrain from TEM and XRD are given in Table 3. It is shown that the on-average grain size of the tested membrane is larger than that of the as-grown by a factor of ~2.

The TEM image in Fig. 6 shows an overlap region between two Pd–23%Ag films, which were wrapped one over the other during membrane preparation. The interface is formed by the substrate–interface surface of the upper foil and the growth surface of the lower foil. It contains a completely bonded region as well as a non-bonded or weak bonded region. The results indicate that the overlap regions most probably are sealed immediately, and that possible leakage would decrease rather than increase with time. Since adhesive substances were not used, the bond formation process may be related to high temperature and pressure during the long-term stability test. The high temperature promotes diffusion of atoms at the interface of the two films forming a permanent diffusion bond. As shown in Fig. 6, the lower foil has columnar grain structure with high density of twin lamellas, similar to the as-grown

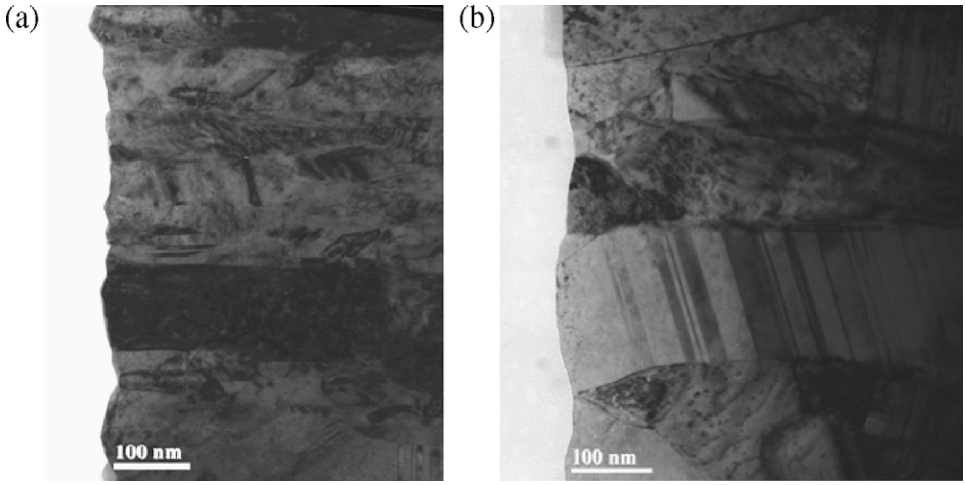

Fig. 4. TEM images showing microstructure near/at the (a) growth surface of as-grown and (b) permeate surface of tested samples. The surfaces are the left edges in the images.

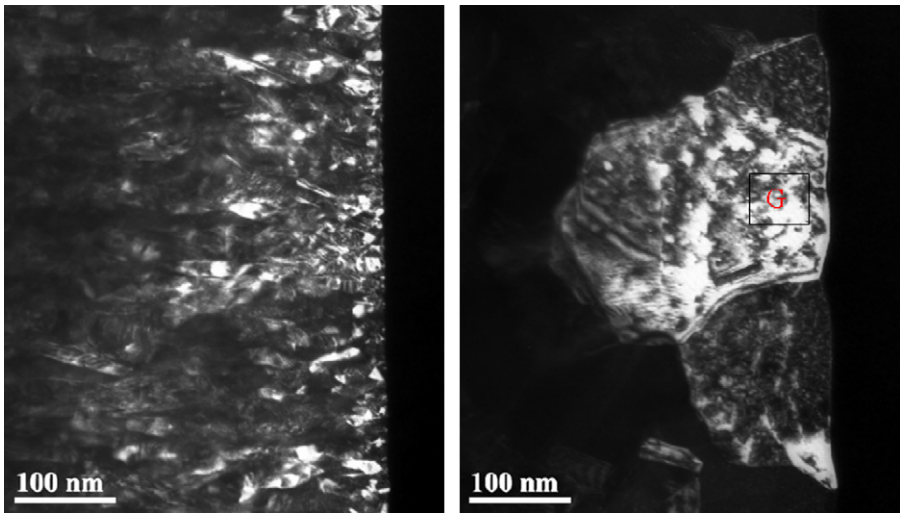

Fig. 5. TEM dark field images showing microstructure near/at the silicon wafer surface of (a) as-grown sample, and (b) feed surface of the tested sample. The surfaces are the right edges in the images.

membrane, whereas the grains of the upper foil near the interface have shown considerable size changes as compared to the grains before the test. On the other hand, the Pd–23%Ag film did not form permanent bonds with the tubular support surface. This may be attributed to the role of the intermetallic diffusion barrier applied between the foil and the porous support. Evidently, after the long-term stability test, pieces of the foils were easily removed without any resistance. Furthermore, the chemical composition of the membrane was analysed by mapping with STEM/EDS at several sites near and at the permeate (interface between Pd and the PSS support), feed surfaces and in the bulk for assurance. None of the elements from the tubular PSS support (Fe, Cr, Ni, ...) were detected in the bulk or close to the surface of the Pd–23%Ag film by EDS. Similarly, XRD did not show any satellite peaks attributed to any additional phase.

3.3.3. XRD analysis

X-ray diffractograms from the as-grown and tested membranes are shown in Fig. 7. The diffractograms of both samples indicate the presence of all the allowed low index peaks of the fcc Pd–23%Ag phase in the measured 2θ-region. The 1 1 1 peak is relatively strong for both as-grown and tested membranes, showing that ⟨1 1 1⟩ is the preferred orientation of the crystallites normal to the surfaces of the films. The absence of shoulders on the main reflections shows that the magnetron sputtered Pd–23%Ag alloy formed a membrane with homogenous composition.

Table 3
Membrane thickness and grain sizes of the as-grown and tested membrane as determined from TEM and XRD.

Sample	Thickness (μm)	Grain size (nm) TEM		Grain size (nm) XRD		Micro-strains ε (10^{-4}) XRD	
		Substrate/feed	Growth/permeate	Substrate/feed	Growth/permeate	Substrate/feed	Growth/permeate
As-grown	2.76	19	89	35	64	18.2	17.8
Tested	2.6	145	137	89	63	3.18	0.35

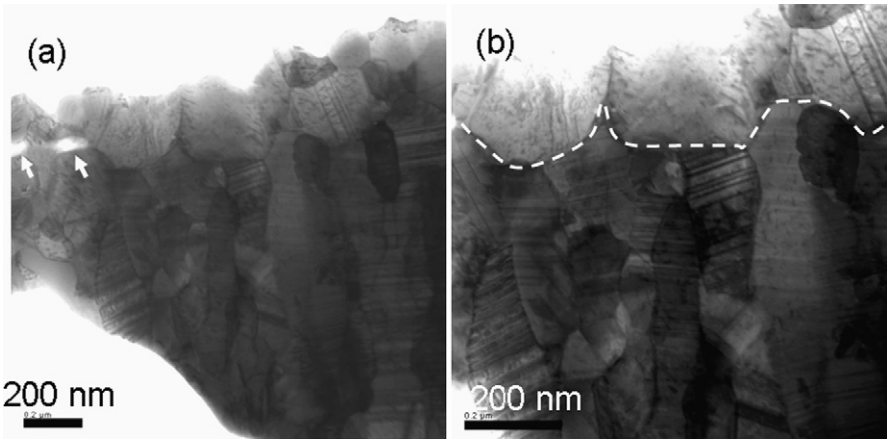

Fig. 6. TEM images of overlapped foils in the tested sample showing the interface between the growth surface of the bottom foil and a substrate–interface surface of a foil on the top. The white arrows in (a) show non-bonded regions, while the dashed curved-line in the magnified image in (b) shows the interface between the growth surface of the bottom foil and a substrate–interface surface of a foil on the top.

The grain size and microstrain estimated from X-ray lines broadening are shown in Table 3. Grain growth may occur during deposition and/or membrane operation of the Pd–23%Ag film. The inset in Fig. 7 shows the details of the 220 line profiles. The peak of the as-grown sample is broader than the tested membrane, implying changes in grain size and/or in microstrains of the tested membrane. For example, the microstrain of the tested sample is less than the as-grown sample by more than one order of magnitude with an apparent large difference between the feed and permeate side. Similarly, the grain sizes increased by a factor of more than 1.5 for the substrate/feed surfaces, but were nearly unchanged for the growth/permeate side. The significant difference shown in the grain size obtained from TEM and XRD measurements are mainly due to differences in the sampling depth/method used by the two techniques. TEM measured grain sizes encompass domains very close to the surface (50–150 nm from the surface) and are from about 200 grains, whereas the XRD data was collected from a larger volume (as deep as 1 μm) that contains larger number of grains. This indicates that the grain size decreases somewhat inwards into the Pd–23%Ag film.

3.3.4. AFM investigations

The detailed surface topography was examined by AFM for the as-grown and tested membranes. Representative AFM images, with scan sizes 1 μm × 1 μm (left), 5 μm × 5 μm (middle) and 10 μm × 10 μm (right), for the Pd–23%Ag films are shown in Fig. 8. Fig. 8(a) shows an AFM image of the as-grown growth surface facing vacuum during sputtering. The surface facing the silicon substrate during growth was too smooth to give contrast by AFM, as reported earlier for membranes of various thicknesses [33]. In Fig. 8(b) post-process images from the feed side surface are displayed. Fig. 8(c) and (d) show corresponding images of the permeate side surface without and with the observed bulged areas/imprints, respectively, as observed with optical microscopy and SEM. The images are flattened using second order polynomial functions. Topographical parameters have been determined from the AFM images and are summarized in Table 4. The determination of these values is based on a series of AFM images taken from more than ten different locations on the membranes. A scan size of 1 μm × 1 μm was used for the analysis, which has been found to be adequate for surface topography determination [34] and in the present case not affected by the observed bulging of the membrane, which is apparent from larger scale height variations in the 10 μm × 10 μm size images in Fig. 8(b–d) for the tested membrane. The root mean square value of the surface roughness together with the corresponding standard deviation is listed in Table 4. The calculated surface area is also presented in the table. Data are not included for images of the permeate side surfaces containing imprints, as these macroscopic features on the membrane surface strongly affect the topographical data. For the ~2.6 μm thick as-grown membranes, the growth surface has a surface roughness of 8.0 ± 0.6 nm, which is about twice the value observed earlier for a membrane of slightly smaller thickness [34]. The reason for this difference is not fully clear, but may be related to varying conditions during sputtering. As can be seen from Fig. 8(b) the topography of the feed side membrane surface has changed significantly after the long-term stability test. The rms value of the surface roughness is determined to 3.6 ± 0.8 nm, and the surface area is (3.0 ± 1.2) × 10^3 nm^2. For comparison, the Pd film–Si substrate interface side of the as-grown film, which served as the feed

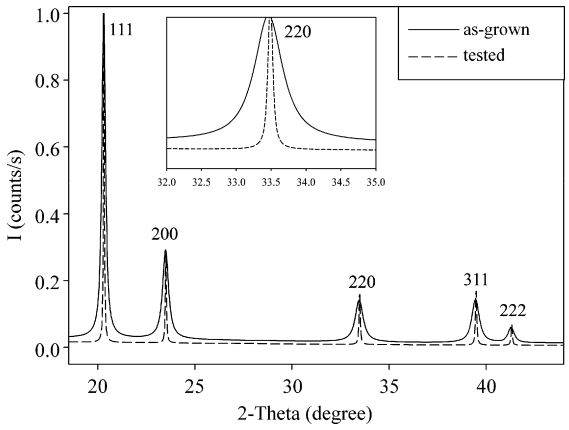

Fig. 7. XRD diffractograms of as-grown and tested samples scanned from substrate/feed surfaces. The dashed-line peaks are for the tested membrane (feed surface on top when scanned). The inset shows a magnified 220 peaks of both samples.

Table 4
Topographical data extracted from the AFM investigations of the growth side of the as-grown membrane, the feed side and the permeate side of the membrane after long-term stability testing.

Surface	Roughness (nm)	Surface area (×10^3 nm^2)
As-grown, growth/permeate side	8.0 ± 0.6	8.1 ± 3.8
Tested, growth/permeate side	6.5 ± 0.7	10.8 ± 4.7
Tested, substrate/feed side	3.6 ± 0.8	3.0 ± 1.2

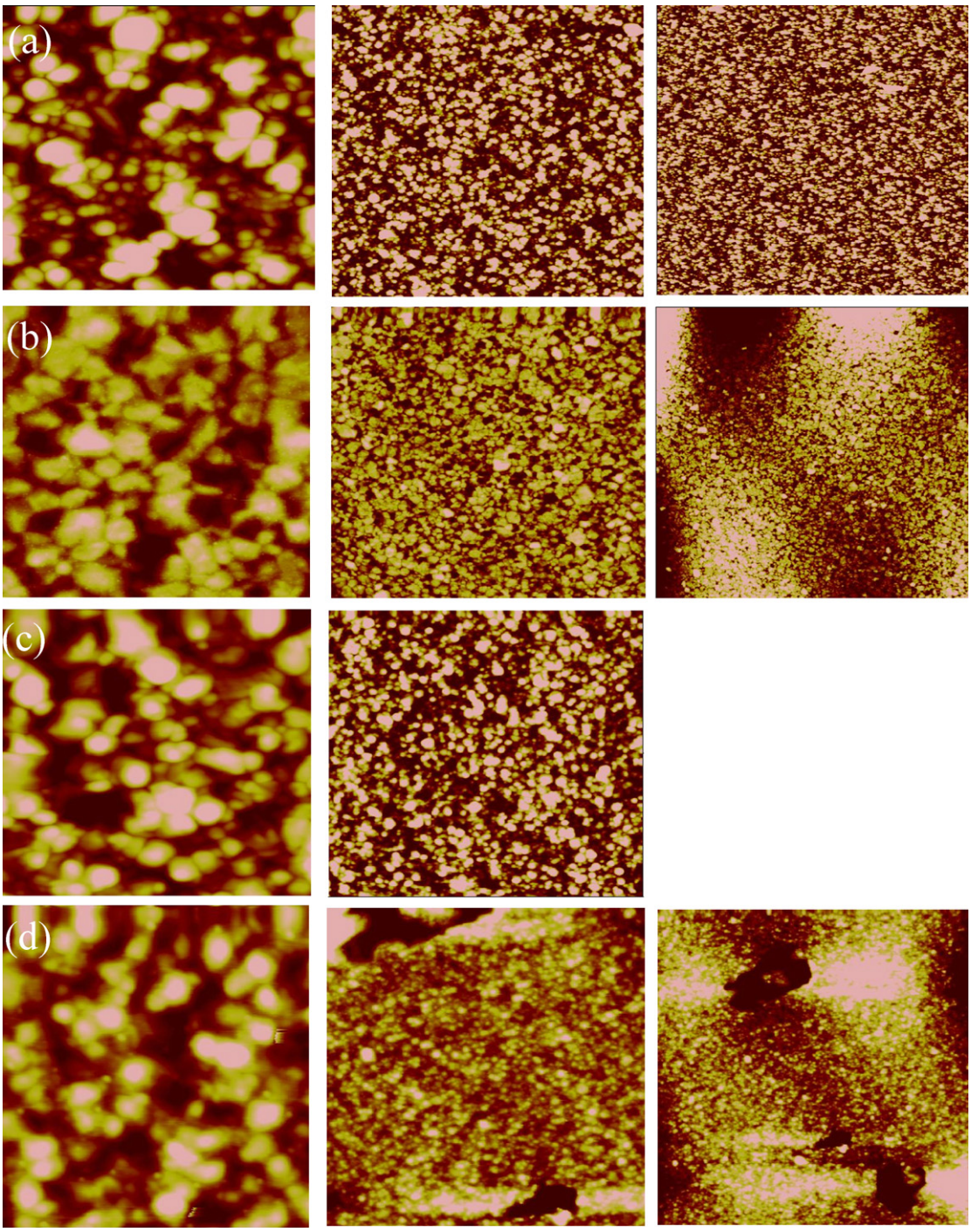

Fig. 8. AFM images of the investigated membranes. (a) As-grown, growth surface. (b) Tested membrane, feed side. (c) Tested membrane, permeate side without defects. (d) Tested membrane, permeate side with defects. The leftmost images have scan size 1 μm × 1 μm. The middle images cover an area of 5 μm × 5 μm and the rightmost images are 10 μm × 10 μm. The height scales for all images are 20 nm from dark to bright, except for the 5 μm × 5 μm and 10 μm × 10 μm images including defects where the height scale covers 50 nm.

side of the membrane, was too smooth to give contrast by AFM. From the data provided in Table 4 it should be noted that the rms roughness of the membrane permeate surface does not change significantly upon testing, it rather shows a small decrease. At the same time the surface area has increased slightly. The fact that this surface has been in contact with the intermetallic coating covered stainless steel support, suggests that the development of surface roughness perpendicular to the surface may have been constrained due to the support. Thermal treatment has earlier been shown to increase the surface roughness of both the feed and permeate side of freestanding membranes [33].

3.3.5. *XPS results*

The chemical composition of the membrane surface was investigated using XPS in order to reveal possible surface segregation effects and oxide formation during operation. Wide energy range survey scans (between 0 and 1300 eV) of the permeate and feed sides of the tested membrane are shown in Fig. 9. The only elements

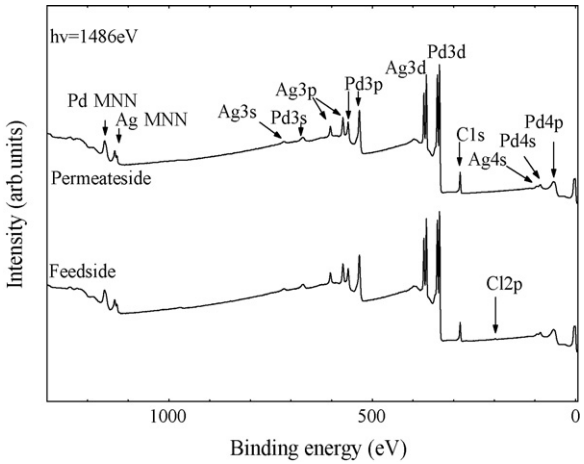

Fig. 9. Wide scan XPS spectra of the feed (lower curve) and permeate (upper curve) side surfaces of the tested membrane.

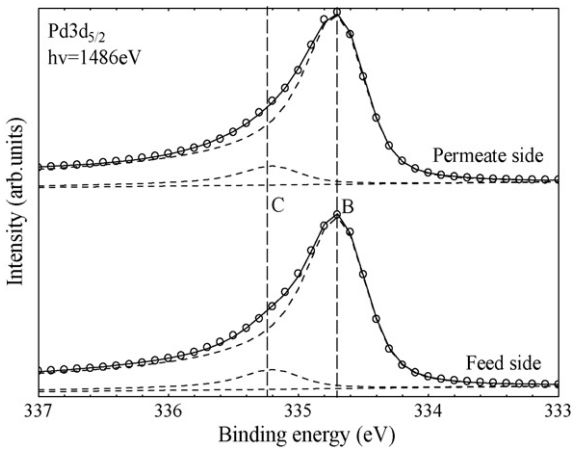

Fig. 10. Pd $3d_{5/2}$ core level spectra for the tested membrane: feed side (lower curve) and permeate side (upper curve).

present besides palladium and silver, are oxygen and carbon, in addition to some chlorine found at the feed side of the film. The origin of the chlorine contamination is unknown. From the C 1s spectra (not shown), some carbon contamination is observed at both surfaces, with a slightly higher (~13%) amount at the permeate side. Contamination can be the cause for this. No elements associated with the intermetallic diffusion barrier or the tubular PSS support were detected, which is in agreement with the STEM/EDS results. Our results generally reveal that the application of the intermetal diffusion barrier effectively prevented diffusion of metal elements from the PSS support to the Pd–23%Ag membrane layer while operating the membrane at a temperature reaching 450 °C.

Fig. 10 shows the Pd $3d_{5/2}$ core level spectra of the tested membrane surfaces. Doniach-Sunjic line shapes were used for fitting the spectra. The same fitting parameters are used for all spectral contributions. The decomposition of the Pd spectra for both the feed and permeate sides show oxide formation in both cases. Peak B is due to the Pd bulk contribution at 334.68 eV while peak C, at 0.52 eV higher binding energy, originates from PdO_x formation at the surfaces. This is similar to earlier observations for membranes exposed to different thermal treatments followed by hydrogen permeation measurements [35]. In comparison, thermal treatment in air has been reported to give a contribution due to PdO with a binding energy shift ~2.0 eV relative to the Pd $3d_{5/2}$ bulk contribution for Pd–Ag/ceramic composite membranes [36,37]. In the present work the oxide contribution is minor relative to the Pd bulk contribution, roughly estimated at about 10%. In both cases, influence by exposure to air during sample transfer to the XPS system on the oxide formation cannot be ruled out. The Ag spectra only shows a single spectral component. The intensity ratio of I(Ag)/I(Pd), as determined from the integral intensity of the Ag $3d_{5/2}$ and Pd $3d_{5/2}$ core level spectra, is equal for both the feed and permeate side surfaces of the membrane after testing indicating the same Pd and Ag content of the two surfaces. The Ag/Pd intensity ratio for the tested membrane surfaces is about 32% higher than the corresponding ratio for the as-grown membrane.

3.3.6. AES depth profiling

The chemical composition, as determined by AES, of the feed and permeate sides of the tested membrane prior to the depth profiling, was in agreement with the XPS observations. The data from the AES depth profiling of the tested membrane is presented in Fig. 11, where (a) and (b) show the depth profile of Pd and Ag at the feed and permeate side surfaces, respectively. During the depth profiling the spectral regions of S, O, and N were also monitored, but no traces of these elements were observed. In addition, Cl was

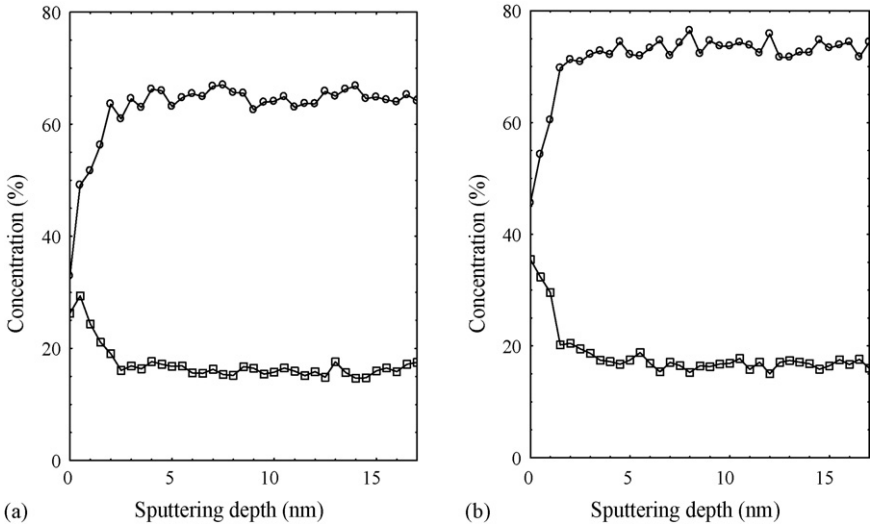

Fig. 11. AES depth profile for the feed (a) and permeate (b) surfaces of the tested membrane. The elements monitored are Pd (empty circle) and Ag (empty square).

observed at the feed side, but was removed immediately after 15 s sputtering, which indicates that Cl was a surface contaminant only. As the carbon AES peaks are overlapping with the Pd region, the carbon spectrum was not measured.

For both surfaces, the Pd intensity increases and the Ag intensity decreases for the first sputtering cycles. After a sputtering depth of ~3 nm, the Pd and Ag levels are stable. The data shows Ag segregation at both the feed and permeate surfaces. The amount of Ag was reduced to ~70% of the value before depth profiling, a number which should not be taken as a quantitative measure due to different sputtering yields for Ag and Pd. Both the XPS results and AES depth profiling data give evidence for segregation of silver to the membrane surfaces. This segregation may be a consequence of the lower surface energy of Ag compared to Pd and it can be activated when the membrane is kept at elevated temperatures. It should be noted that the surface composition of these membrane surfaces both depends on the membrane thermal treatment, but also on exposure to different gaseous atmospheres, as has been shown for freestanding membranes [35]. Recent theoretical investigations [38,39] indicate segregation of palladium to the surface for Pd–Ag alloys in the presence of hydrogen. An earlier experimental study supports this finding [40]. In the present work, the surface analysis was performed post-long-term testing. After the long-term testing the membrane was cooled down in N_2/Ar atmosphere to prevent hydrogen-induced embrittlement of the membrane at lower temperatures. The observed palladium–silver surface composition may be affected by this procedure.

4. Conclusions

The long-term stability of Pd–23%Ag/stainless steel composite membranes has been examined in H_2/N_2 mixtures as a function of both temperature and feed gas pressure. During continuous operation, the membrane shows a good stability at 400 °C while the N_2 leakage increases very slowly at a temperature of 450 °C (P_{feed} = 10 bar). After 100 days of operation (P_{feed} = 5–20 bar, T = 350-450 °C), the N_2 permeance equals 7.0×10^{-9} mol m^{-2} s^{-1} Pa^{-1}, which indicates that the H_2/N_2 permselectivity still lies around 500, based on a H_2 permeance equal to 3.0×10^{-6} mol m^{-2} s^{-1} Pa^{-1}.

Grain growth during prolonged operation of the Pd–23%Ag film is confirmed by TEM and XRD. SEM indicates that the formation of pinholes in the film is the main reason for the increase in N_2 leakage during testing at temperatures above 400 °C. The grain growth is accompanied by small increase in surface area and segregation of Ag to the membrane surfaces. TEM and XPS reveal that the application of the intermetal diffusion barrier effectively avoids diffusion of metal elements from the support to the Pd–23%Ag membrane layer while operating the membrane to a temperature reaching 450 °C. Despite the generation of small pin holes, a membrane life-time of several (2–3) years ($T \leq 425$ °C) is estimated for the employed experimental conditions based on long-term stability tests over 100 days.

Acknowledgements

This research is financed by the European Union, the CO_2 Capture Project (CCP), and the Research Council of Norway (RCN) through the following programs, CCP/RCN-Renergi 2004/2005 (Contract No: C04043 and 5299775), RCN-Nanomat (Contract no: 158516/S10), and the EU-6FP CACHET project (Contract no.: 019972) (www.cachetco2.eu). We thankfully acknowledge Pall Corp. for providing the membrane supports, S. Diplas for performing the XPS measurements and R. Mathiesen for help with the XRD experiments.

References

[1] J.N. Keuler, L. Lorenzen, R.D. Sanderson, V. Prozesky, W.J. Przybylowicz, Thin Solid Films 347 (1999) 91.
[2] K. Hou, R. Hughes, J. Membr. Sci. 214 (2003) 43.
[3] G. Xomeritakis, Y.S. Lin, J. Membr. Sci. 120 (1996) 261.
[4] N. Itoh, T. Akiha, T. Sato, Catal. Today 104 (2005) 231.
[5] A. Basile, E. Drioli, F. Santella, V. Violante, G. Capannelli, G. Vitulli, Gas Sep. Purif. 10 (1996) 53.
[6] V. Jayaraman, Y.S. Lin, J. Membr. Sci. 104 (1995) 251.
[7] V. Jayaraman, Y.S. Lin, M. Pakala, R.Y. Lin, J. Membr. Sci. 99 (1995) 89.
[8] B. McCool, G. Xomeritakis, Y.S. Lin, J. Membr. Sci. 161 (1999) 67.
[9] J. O'Brien, R. Hughes, J. Hisek, Surf. Coat. Technol. 142 (2001) 253.
[10] J.H. Tong, H. Suda, K. Haraya, Y. Matsumura, J. Membr. Sci. 260 (2005) 10.
[11] I.P. Mardilovich, E. Engwall, Y.H. Ma, Desalination 144 (2002) 85.
[12] R. Bredesen, H. Klette, US Patent 6.086.729 (2000).
[13] T.A. Peters, M. Stange, H. Klette, R. Bredesen, J. Membr. Sci. 316 (2008) 119.
[14] R. Bredesen, K. Jordal, A. Bolland, Chem. Eng. Process. 43 (2004) 1129.
[15] H.Y. Gao, Y.S. Lin, Y.D. Li, B.Q. Zhang, Ind. Eng. Chem. Res. 43 (2004) 6920.
[16] S. Tosti, L. Bettinali, S. Castelli, F. Sarto, S. Scaglione, V. Violante, J. Membr. Sci. 196 (2002) 241.
[17] F. Guazzone, E.A. Payzant, S.A. Speakman, Y.H. Ma, Ind. Eng. Chem. Res. 45 (2006) 8145.
[18] S.E. Nam, K.H. Lee, Ind. Eng. Chem. Res. 44 (2005) 100.
[19] D. Yepes, L.M. Cornaglia, S. Irusta, E.A. Lombardo, J. Membr. Sci. 274 (2006) 92.
[20] Y. Huang, R. Dittmeyer, J. Membr. Sci. 282 (2006) 296.
[21] C.L. Su, T. Jin, K. Kuraoka, Y. Matsumura, T. Yazawa, Ind. Eng. Chem. Res. 44 (2005) 3053.
[22] Y.H. Ma, B.C. Akis, M.E. Ayturk, F. Guazzone, E.E. Engwall, I.P. Mardilovich, Ind. Eng. Chem. Res. 43 (2005) 2936.
[23] A.E. Ayturk, I.P. Mardilovich, E.E. Engwall, Y.H. Ma, J. Membr. Sci. 285 (2006) 385.
[24] I.P. Mardilovich, E. Engwall, Y.H. Ma, Presentation at the 9th International Conference on Inorganic Membranes, Lillehammer, Norway, 2006.
[25] W. Mekonnen, B. Arstad, H. Klette, J.C. Walmsley, R. Bredesen, H. Venvik, R. Holmestad, J. Membr. Sci. 310 (2008) 337.
[26] R. Delhez, Th.H. de keijser, J.I. Langford, D. Louer, E.J. Mittemeijer, E.J. Sonneveld, in: R.A. Young (Ed.), The Rietveld Method, Oxford University Press, Oxford, 1995, p. 132.
[27] W.M. Tucho, M. Stange, R.H. Mathiesen, J.C. Walmsley, R. Holmestad, R. Bredesen, in preparation.
[28] F. Guazzone, Y.H. Ma, AICHE J. 54 (2008) 487.
[29] A. Matzakos, Presentation at the 2006 NHA Annual Meeting – Fuel Cells Topical – Innovations in Fuel Processing Session, 2006.
[30] A. Matzakos, Presentation at the 9th International Conference on Inorganic Membranes, Lillehammer, Norway, 2006.
[31] S. Tosti, A. Basile, L. Bettinali, F. Borgognoni, F. Chiaravalloti, F. Gallucci, J. Membr. Sci. 284 (2006) 393.
[32] P.P.A.C. Pex, Y.C.v. Delft, in: D.C. Thomas (Ed.), Carbon Dioxide Capture for Storage in Deep Geological Formations—Results from the CO_2 Capture Project; Capture and Separation of Carbon Dioxide from Combustion Sources, Elsevier, Naperville, 2005.
[33] A.L. Mejdell, H. Klette, A. Ramachandran, A. Borg, R. Bredesen, J. Membr. Sci. 307 (2008) 96.
[34] A.L. Mejdell, MSc Thesis, NTNU, 2004.
[35] A. Ramachandran, A. Mejdell, T.A. Peters, M. Stange, H.J. Venvik, A. Borg, R. Bredesen, Proceedings of the 10th International Conference on Inorganic Membranes, Tokyo, Japan, 2008.
[36] L. Yang, Z.X. Zhang, X.H. Gao, Y.J. Guo, B.F. Wang, O. Sakai, H. Sakai, T. Takahashi, J. Membr. Sci. 252 (2005) 145.
[37] L. Yang, Z.X. Zhang, B.J. Yao, X.H. Gao, H. Sakai, T. Takahashi, AICHE J. 52 (2006) 2783.
[38] O.M. Løvvik, S.M. Opalka, Surf. Sci. 602 (2008) 2840.
[39] S. Gonzalez, K.M. Neyman, S. Shaikhutdinov, H.J. Freund, F. Illas, J. Phys. Chem. C 111 (2007) 6852.
[40] J. Shu, B.E.W. Bongondo, B.P.A. Grandjean, A. Adnot, S. Kaliaguine, Surf. Sci. 291 (1993) 129.

Paper IV

Methanol Adsorption on Pd (110) and Ag/Pd(110) studied by High Resolution Photoelectron Spectroscopy

A. Ramachandran, Ø. Borck, T.H. Andersen, I.-H. Svenum, L. E. Walle and A. Borg

To be submitted to Surface Science

Methanol Adsorption on Pd (110) and Ag/Pd(110) studied by High Resolution Photoelectron Spectroscopy

A. Ramachandran, Ø. Borck, T. H. Andersen, I.-H. Svenum, L. E. Walle and A. Borg*
Department of Physics, Norwegian University of Science ad Technology, NO-7491 Trondheim, Norway

Abstract

Adsorption of methanol on clean Pd (110) and on an alloyed Ag/Pd(110) surface has been studied by high resolution photoelectron spectroscopy. On Pd(110) two different methanol species were observed upon adsorption at 100K and subsequent heating up on 200K. The species with lowest C1s core level binding energy was remaining at the surface for low methanol coverage. The adsorption and decomposition behavior of methanol on a Ag/Pd(110) surface alloy formed by depositing Ag on Pd(110) at elevated temperature was similar to that of the pure Pd(110) surface, a finding showing that the amount of Ag present in the surface in this study did not affect the decomposition behavior of methanol as compare to pure Pd(110). DFT calculations show little influence of Ag on the binding of methanol to Pd.

Key words: Methanol, adsorption, Palladium, CO, high resolution photoelectron spectroscopy, DFT.

*Corresponding author: anne.borg@ntnu.no

Introduction

Hydrogen has many applications in industry and is one of the energy carriers that have recently attracted interest due to its potential as a zero emission fuel [1-3]. It can be produced from several sources including methanol, which is an important source for hydrogen in fuel cell applications in mobile units [4-7], where hydrogen storage imposes an inherent problem. Hydrogen can be produced directly from methanol through three different processes, partial oxidation [8-11], thermal decomposition [12-15] and steam reforming [11, 16-18].

Palladium has been found to be catalytically active in methanol decomposition to CO and H_2 [10, 19-21]. However, it is less selective for the steam reforming reaction [10]. Moreover, Pd is a potential candidate membrane material for hydrogen purification in fuel cell applications due to its high selectivity and permeability to hydrogen [22]. To prevent embrittlement occurring in pure Pd due to hydride phases formation [23, 24], Pd alloys suppressing the phase transition are often used. Silver (Ag) has in this respect, as well as for the hydrogen permeation, been identified as a favorable alloying element [25]. Presence of small amounts of methanol in the feed gas has been shown to decrease the hydrogen flow through Pd/Ag membranes [26]. Possible causes for deactivation were suggested to be build-up of carbonaceous species and unconverted methanol at the membrane surface [26]. For this reason it is important to understand how alloying of silver into palladium affects the adsorption behavior of methanol on palladium. In the present work we have addressed this issue by studying adsorption and decomposition upon heating of methanol on clean Pd(110) and on Ag/Pd(110) using high resolution photoelectron spectroscopy.

Due to the importance in gaining understanding of elementary steps in catalytic reactions adsorption and decomposition of methanol on transition metal surfaces have been extensively investigated [27-35]. Generally, methanol adsorbs molecularly at low temperatures, forming multilayers at high exposures. The decomposition of methanol on single crystal surfaces upon thermal treatment is strongly dependent on the atomic composition and the geometric structure of the surface. Methanol decomposition often results in either formation of CO on the surface formed through dehydrogenation or

scission of the C–O bond. Methanol decomposition on Pd(110) and Pd(111) at 100K follows the main trend of molecular adsorption. Methanol decomposes to CO upon heating, however, the decomposition pathway leading to CO formation has been debated [29, 30, 32, 33, 36-38]. In early electron energy loss spectroscopy (EELS) studies [36] a methoxy intermediate was reported. More recent investigations by Pratt et al [32] suggest that methoxy is an unstable intermediate on Pd(110). Also desorption of chemisorbed methanol above 200K have been reported [32, 33] along with and decomposition of methanol to CO and H_2 at 250K [33, 39]. No C-O bond scission has been reported on Pd(110) and Pd(111) [33], while preadsorbed oxygen on these surfaces has been observed to enhance the C-O bond scission [37, 38, 40]. On silver surfaces molecular methanol adsorption is observed [41-44]. Upon heating the molecule desorbs without forming any decomposition products [41-44].

In the present study we investigate the adsorption and decomposition upon heating of methanol on clean Pd(110) and on Ag/Pd(110) using high resolution photoelectron spectroscopy to address the influence of silver on the methanol decomposition pathway for a Pd(110) with Ag as the alloying element. The influence of Ag on the bonding of methanol to the Pd(110) surface atoms is addressed through density functional theory calculations.

Experimental

High-resolution photoelectron spectroscopy experiments were performed at beam line I311 of the MAX II synchrotron radiation source in Lund, Sweden. This beam line is equipped with a modified SX-700 monochromator and a large Scienta type hemispherical electron energy analyzer (SCIENTA SES200) [45]. The base pressure in the UHV system was $\leq 3x10^{-10}$ mbar.

The Pd(110) crystal was cleaned by cycles of sputtering, heating in oxygen and subsequent annealing. This procedure gave well-defined, clean surfaces as judged from LEED patterns and photoemission measurements of the C1s core level region. Ag was evaporated from a tungsten basket with the Pd(110) crystal kept at a temperature of

500K during deposition. The amount of Ag deposited was determined from the damping of the $Pd3d_{5/2}$ core level intensity.

Liquid methanol (purity 99.8%) from Sigma-Aldrich Chemie GmbH, Germany, was cleaned by freeze-pump-thaw cycles prior to exposure. The sample was kept at temperature 100K during methanol exposure and subsequently flashed to selected temperatures. No ordered methanol induced structures were observed by LEED for Pd(110) or Ag/Pd(110). All photoemission spectra were recorded at a sample temperature of 100K.

The C1s core level spectra were recorded at photon energy 380 eV and the $Pd3d_{5/2}$ core level at 390 eV. The corresponding experimental resolution was about 80 meV. The $Ag3d_{5/2}$ core level spectra were measured at photon energy 450eV with a spectral resolution of 100 meV. The photon energy used for measuring the valence band spectra was 120eV, which is close to Pd4d Cooper minimum. All spectra were measured at normal emission and the binding energy was calibrated by recording the Fermi edge immediately after the core level regions.

All spectra have been normalized to the background on the lower binding energy side of the core-level peaks. Linear background subtraction has been applied. Doniach-Sunjic line shapes have been used for fitting the spectra [46]. The first vibrational component of the C-H stretch vibration in the methyl group in methanol has been included in the fitting. As this contribution could not be distinctly resolved in the spectra gas phase values [47] for the intensity ratio (0.33) and the energy shift (400 meV) were used.

Computational

The DFT calculations reported here were performed using the DACAPO code [48]. The exchange and correlation effects are taken into account using the Perdew-Burke-Ernzerhof (PBE) version [49] of the generalised gradient approximation (GGA). The ionic cores and their interactions with the valence electrons are described by ultrasoft pseudopotentials [50]. A plan-wave basis with a kinetic energy cut off of 340 eV was used in all calculations.

Several different surface models were employed in this study. The clean Pd(110) and Ag(110) surfaces were represented by periodically repeated slabs of five atomic layers separated by a ~14 Å vacuum gap. We used a (2x2) surface unit cell with four atoms per layer. Three different Pd-Ag model alloys were constructed by replacing one Pd atom in the first layer, second layer or third layer by an Ag atom, as shown in Fig. 1.

The minimum-energy adsorption geometries for methanol were determined by placing the adsorbate in the high-symmetry sites on these surfaces, and allowing the atoms of the adsorbate and three uppermost layers of the slab to relax freely until the residual forces on each atom were less than 0.02 eV/Å. An extensive set of different adsorbate orientations with respect to the surface were explored. In these calculations we employed a Monkhorst-Pack [51] k-point sampling grid of 6x8x1. The artificial electric field created by the asymmetry of the adsorption system was compensated by a self-consistently determined dipole correction applied in the vacuum region [52, 53].

The reported adsorption energies per molecule were calculated from

$$E_{ads} = - (E_{SM} - E_S - E_M)$$

where E_{SM} is the total energy of the adsorbate-substrate system, E_S is the energy of a clean surface slab, and E_M is the energy of an isolated molecule. With this definition, a positive adsorption energy indicates stabilisation.

Results and discussion

Methanol adsorption and decomposition on Pd(110)

C1s spectra recorded after 0.5 L and 5 L methanol exposure of clean Pd(110) at 100K followed by subsequent heating to selected temperatures are displayed in Fig. 2. The binding energies of the different contributions identified in the spectra are summarized in Table 1. Corresponding $Pd3d_{5/2}$ spectra are shown in Fig. 3 along with the spectra recorded for the clean Pd(110) surface (lower panels in Fig. 3a and b). Adsorption of 0.5 L CH_3OH (Fig. 2a) results in less than a monolayer methanol coverage on the

Pd(110) (see below). Four different contributions can be dissolved in the C 1s spectra. The main contribution, labelled A, has a binding energy of 285.72 eV. The vibrational contribution included in the fitting to account for the first vibration component of the C-H stretch vibration in the methanol methyl group is not labelled. This vibrational contribution is needed to obtain a proper fitting to the spectrum, even though it is not clearly resolved. A second contribution, C, appears at the high binding energy side (at 286.03.eV) of contribution A and also for this peak a vibrational contribution (not labelled) is included. A third peak (D) is found at the low binding energy side of the main contribution at binding energy 285.27 eV. Finally a minor peak F is observed at 284.51 eV, which is getting sharper upon heating. This contribution remains on the surface after annealing to 500K and can be identified as being due to carbonous species at the surface. Upon annealing to 170K one major change is observed in the C1s spectrum namely the disappearance of contribution C. Further heating to 250K give some important changes in the spectrum, even though the observed binding energies of the contributions are not significantly different from the values found after heating to 170K. First, it should be noted that contribution D has disappeared. Moreover, the shape of the spectrum has changed, as judged from the change in FWHM from 0.50 eV to 0.36.eV, indicating that new species have been formed at the surface. Also the spectrum can be fitted with one component only. This new contribution is labelled E and has binding energy 285.68 eV. The overall spectral intensity at 250K is reduced by about 65% as compared to the spectrum recorded after heating to 170K, implying a combination of methanol desorption and decomposition at this stage. Upon annealing to 350K, peak E is shifted to slightly lower binding energy (285.63 eV). Finally after heating to 500K the only remaining C1s contribution at the surface is peak F.

The main difference in the C1s spectrum upon further deposition of methanol (5 L) is the appearance of an additional, broad contribution M at binding energy 286.98 eV in the as-deposited spectrum (lower panel of Fig. 2b), which disappears upon heating to 170K. Due to the broad nature of this peak we have chosen not to include a vibrational contribution to the fitting of this spectral feature. The other contribution after deposition, marked with (A+C) clearly includes contributions due to peaks A and C observed after 0.5L exposure. As contribution M strongly influences the overall

spectrum at this stage we have chosen not to fit the (A+C) part with more than one component, which for this reason appear at an intermediate binding energy as compare to the individual A and C components as indicated in Table 1. After heating to 170K the spectral contribution C is significantly stronger as compared to peak A, indicating a larger first layer coverage than after 0.5 L exposure at 100K. To understand the behaviour of this component in more detail we have a spectrum recorded after heating to 200K, which shows that component C is still present at the surface but at lower intensity compared to peak A. Contribution D is maintained in the spectrum at this point. The spectra recorded after annealing to 250K and 350K are similar to what we observed for the lower exposure of methanol and the following annealing at the respective temperatures.

Fig. 3 shows the $Pd3d_{5/2}$ spectra for clean Pd(110) (lower panel) and after the adsorption of 0.5L (a) and 5.0 L (b) CH_3OH on this surface followed by annealing at the specified temperatures. The clean Pd spectra is decomposed into a bulk (B) (at 334.87eV) and a surface (S) (at 334.36eV) component giving a surface core level shift (SCLS) of -0.51eV, which is in close agreement with previously reported SCLS for Pd(110) at -0.55eV [54]. 0.5 L exposure of methanol on Pd(110) causes the surface component to disappears and the spectrum to broaden into one, unresolved contribution (FWHM of 0.90 eV) at binding energy 335.04 eV. Upon heating to 170K and 250K the only change in the $Pd3d_{5/2}$ spectra is a slight increase in the overall intensity accompanied by a decrease in FWHM of the spectrum. Annealing at 350K causes the Pd peak to shift to 334.90 eV, closer to the bulk Pd contribution (B) as well as the surface contribution to reappear in the spectrum indicative of reduced adsorbate coverage at this point. After exposure to 5.0 L CH_3OH, see Fig. 3b, the contribution at high binding energy side in the $Pd3d_{5/2}$ spectrum increases in intensity, showing a higher first layer methanol coverage than indicated by the disappearance of the surface contribution after 0.5L methanol exposure. In this case the spectrum can be decomposed into a bulk contribution as well as a contribution due to the interaction with methanol at binding energy 335.26 eV (peak G in Fig. 3b). After flashing to 170K, peak G is reduced in spectral weight. Only one broad feature can be seen in the spectrum at 250K as in the case of the 0.5L CH_3OH exposure. Further heating gives the same behaviour as in the

0.5L methanol exposure case. At 500K, the surface component and the overall shape of the $Pd3d_{5/2}$ spectra is similar to that of the clean Pd(110) surface.

A series of valence band spectra for 0.5L CH_3OH deposited Pd(110) at 100K and subsequent annealing at the selected temperatures is displayed in Fig. 4. The spectrum for the clean Pd(110) surface is shown in the lower panel of the figure. The energy region displayed is where we have the contributions appearing after adsorption of methanol, with new peaks at ~25eV (X), ~16eV (Y), ~12 eV (Z), and ~8.4 eV (W). In comparison spectral features due to gas phase methanol have been reported at ~23eV, ~18eV, ~16eV, 13 eV and ~11eV [55]. Moreover, methanol adsorption on Ag(110) gives contributions at similar binding energies as observed in the present case [56]. Heating to 170K only causes minor changes in the valence band spectra. At 250K, the peaks X and Y disappear along with peaks Z and W whereas two new contributions U, at ~11 eV, and V, at ~8 eV with a shoulder at 7.2 eV, appear. The latter two contributions remain after heating to 350K and disappear upon annealing to 500K. For higher methanol exposure the same spectral features (spectra not shown) are observed in the valence band region and with the same behavior upon heating.

Molecular methanol has been reported formed on the Pd(110) surface upon deposition at temperatures around 100K [32, 33, 36]. A.Barteau et.al [33] reported a desorption temperature of multilayer methanol at 147K, shifting to higher temperatures (up to 10K) for higher methanol coverages as expected for zeroth order desorption of the multilayer. At submonolayer coverages of methanol desorption was observed at about 245K, a temperature decreasing to about 225K for monolayer coverage. Contribution A could be due to either first layer methanol or methoxy formed upon methanol adsorption. The presence of methoxy at the Pd(110) surface has been debated [32, 36]. Also it has been reported to appear after heating at 200K. As peak A is the main species at the surface at low methanol exposure we propose that this peak is due to first layer methanol on Pd(110). Peak M appearing at high coverage of methanol and disappearing after heating to 170K is due to methanol multilayer formation. Turning to component C at the high binding energy side of contribution A, the intensity of this peak depends on the initial methanol exposure and the overall adsorbate coverage on the surfaces. This component

dominates the spectrum at high first layer coverage while contribution A remains stronger as the coverage decreases. Based on this behaviour we interpret contribution C to be due to first layer adsorption of a second methanol species associated with higher CH_3OH coverage at the surface. The methanol induced contributions to the C1s are accompanied by the disappearance of the surface contribution in the $Pd3d_{5/2}$ spectrum and appearance of an adsorbate induced component.

In addition to the two methanol contributions to the C 1s spectra an additional spectral feature (D) is observed at binding energy 285.25 eV, which remains after heating to 200K at similar spectral weight but disappears at 250K. As part of the decomposition pathway for methanol, before further decomposition occurs, methoxy is commonly observed as an intermediate. As already noted, in the case of Pd(110) the presence of methoxy has been debated [32, 36]. In an earlier work we have observed methoxy formation upon initial adsorption of methanol on $Ni_3Al(111)$ and NiAl(110) [57], at lower C 1s binding energies than for methanol at the same surfaces. We therefore speculate if peak D may be due to a small amount of methoxy formed at specific sites at the Pd(110) upon initial methanol deposition. The disappearance of contributions A and C along with the general changes in peak shapes in the C1s spectral upon heating to 250K are accompanied with the contributions X, Y, Z and W disappearing in the valence region at the same time as two new peaks are appearing (U and V). The binding energies of contributions U (~11 eV) and V (~8 eV) are in agreement with peaks observed at 11 eV and 8eV upon adsorption of CO on Pd(110) [58]. These peaks have been interpreted as being due to the 4σ and 5σ orbitals of CO. The shoulder observed at 7.2 eV was assigned to the CO 1π orbital. The corresponding changes in the $Pd3d_{5/2}$ spectra are minor except for indicating lower amount of adsorbate at the surface at this stage through higher spectral intensity. Previous studies [33] have shown that after heating to above 225K only CO and H are present at the surface. As noted above the shape of the C1s contribution E is distinctively different from the methanol contribution A including the corresponding vibrational contribution. CO adsorption on Pd(110) has been subject to several high resolution photoemission spectroscopy studies [59-61]. Ramsey et. al [61] reported C1s core level contributions due to CO adsorption on

Pd(110) at 286.0 eV and 286.2 eV for the higher coverage and 284.6-284.9 eV for the lower coverage cases, suggesting bridge site and two highly coordinated CO sites respectively. Jones et al. [59, 60] observed a C1s energy position at lower CO coverage at 285.65 eV, which increased by 0.26 eV after 0.7 L exposure when CO was dosed at low temperature (137K). When comparing different results reported for CO adsorption on Pd(110) one should keep in mind that several ordered adsorbate structures have been reported depending on CO exposure and substrate temperature [59-64]. The binding energy found for contribution E in the C1s spectra in the present work is in good agreement with those observed by Jones et al [59, 60] indicating that the observed spectra are consistent with CO being present on the Pd(110) surface after heating the methanol covered surface to 250K. In the literature, there is some discrepancy in assigning the adsorption site of CO on Pd(110). An on-top adsorption site was suggested by A. Wander [65], while bridge site CO was suggested by others [66-68]. Later, A. Locatelli et.al [69] concluded that CO adsorption site after 1L CO/Pd(110) system is the short bridge site. As pointed out earlier, Ramsey et.al also suggested that the higher binding energy (286.0 eV) peak is due to a bridge site of CO on the basis that the higher the coordination of adsorbate, the lower binding energy of the contribution. The appearance of peaks U (~11eV) and V (~8eV) are in good agreement observed contributions to the valence band region upon CO adsorption on Pd(110) [58] supporting the interpretation of the C1s spectra.

Methanol adsorption and decomposition on Ag/Pd(110)

Ag was deposited on the Pd(110) surface at 500K to ensure alloying of Ag into the Pd(110) surface [70, 71]. The amount of silver was estimated at about 0.6 ML from the reduction of the $Pd3d_{5/2}$ peak assuming an Ag overlayer. However, the true amount of silver in the surface is higher as the alloying causes Ag to be incorporated into the Pd(110) surface. As can be seen from Fig. 5, the $Pd3d_{5/2}$ spectrum after still has a significant surface component, reduced by ~25% as compared to the clean Pd(110) surface. The binding energy of the $Ag3d_{5/2}$ core level after deposition is 367.25 eV, which is similar to observed binding energies of thin Ag deposited on Pd at room temperature and subsequently annealed to 520K [71]. In alloy systems the core level binding energies are expected to depend on the alloy composition. For the Ag_xPd_{1-x}

alloy system Steiner and Hufner [72] reported a linearly decrease in the $Ag3d_{5/2}$ core level binding energy for x varying from one to zero. At a silver content of 25% a decrease in the binding energy by 0.75 eV is predicted. An $Ag3d_{5/2}$ core level binding energy of 367.65 eV has been measured for a (100) oriented $Pd_{75}Ag_{25}$ single crystal [73], which may suggest that our Ag composition is more dilute.

C1s spectra recorded after exposing the Ag/Pd(110) surface to 2.5 L methanol at 100K followed by subsequent heating to selected temperatures are displayed in Fig. 6. The binding energies of the different spectral contributions are summarized in Table 2. This exposure yields a multilayer methanol coverage on the surface, as can be seen from the lower spectrum in Fig. 6 containing a CH_3OH multilayer component M', which disappears upon heating to 170K. Also on this surface the two different species (A' and C') attributed to first layer methanol are formed along with a small contribution D' at the low binding energy side of peak A'. A small fraction of carbonous species (F') is also observed. In the $Pd3d_{5/2}$ spectrum, shown in the upper panel in Fig. 5 methanol deposition gives a peak (H') at higher binding energies relative to the bulk contribution (B) as well as disappearance of the surface component (S) whilst no changes occur in the $Ag3d_{5/2}$ spectra (not shown). At 170K the amount of species C' is higher than of species A', as also observed for Pd(110) after heating the multilayer covered surface to 170K. Further annealing to 200K for CH_3OH on Ag/Pd(110) results in only methanol species A' remaining on the surface along with contributions D' and G'. Even though the differences are small, the disappearance of contribution C' at 200K may suggest a lower methanol coverage on the Ag/Pd(110) alloy surface as compared to Pd(110). Above 200K the features in the C1s spectra for the Ag/Pd(110) system is following the behavior observed for Pd(110). At 250K a shift in the $Ag3d_{5/2}$ core level binding energy by 0.14eV is observed, which may be related to the interaction of the alloy surface with CO. Corresponding valence band spectra (not shown) reveal the same adsorbate induced contributions as for Pd(110) both upon methanol adsorption and after heating to the selected temperatures. In a similar experiment with a smaller amount of silver on Pd(110) but a larger surface coverage, as judged by the damping of the $Pd3d_{5/2}$ surface contribution, the overall behaviour upon methanol deposition and subsequent annealing was the same.

The high-resolution photoelectron spectroscopy results show that the adsorption, desorption and decomposition behaviour of methanol is not significantly affected by Ag as alloying element in the Pd surface. In comparison, only molecular methanol is reported formed on Ag(110) with a first layer desorption temperature of 165K [43]. To gain some further insight in this aspect we have determined the bonding geometries of methanol on some model Ag/Pd(110) surfaces shown in Fig. 1. For all the considered surface models, we found that methanol adsorb with its oxygen atom close to the on top site and the C–O axis tilted with respect to the surface normal, see Fig. 7. A similar bonding geometry has been found in previous DFT calculations of methanol adsorption on Pd(111) [28, 74, 75], Ag(110) [76], and Ag(111) [77]. The O–Pd nearest neighbour distance is 2.40Å. In comparison, the corresponding distance for methanol adsorption on Pd(111) has been reported to be 2.509 Å [75] and 2.25 Å [74]. The O–Ag nearest distance is calculated to be 2.56 Å when methanol is adsorbed on Ag(110) and 2.48 Å when adsorbed on the Ag/Pd(110) alloy (model A). This is considerably shorter than a previously reported O–Ag bond length of 2.952 Å for methanol on Ag(110) [76]. A possible reason for this is a that Sun *et al* employed a smaller (2x1) surface unit cell. The distance between the (periodically repeated) adsorbates is then smaller, giving a different adsorbate–adsorbate interaction compared to our case and possibly a different bond length. The geometry of the methanol molecule is only little perturbed by the adsorption, with changes in bond lengths and angles of less than 2% compared to the values for the free molecule. The adsorption induces a small rumpling of the surface with the atom below the adsorbate being pulled out by ~0.03 Å compared to the clean surface geometry. The calculated adsorption energies are listed in Table 3. It is immediately clear that methanol binds more weakly to the Ag(110) surface than Pd(110), consistent with the experimental findings [32, 33, 36, 43, 44].

The effect of alloying is only modest for the models considered in this work. Replacing one of the outermost layer Pd atoms by an Ag atom reduces the adsorption energy by only 0.01-0.06 eV compared to adsorption on the Pd(110) surface. Interestingly, adsorption in the Ag on top site is of comparable strength to adsorption in one of the Pd

on top sites, and with a larger adsorption energy by 56% compared to the pure Ag(110) surface. Replacing a second or third layer Pd atom by Ag has no influence on the adsorption energy when compared to adsorption on Pd(110).

Our results fit well with the *d*-band model of Hammer and Nørskov [77, 78]. The center of the 4*d* states of the Pd(110) surface atoms is higher in energy than the center of the 4*d* states of the Ag(110) surface atoms by 2.3 eV. According to the *d*-band model, methanol should then bind stronger to the Pd(110) surface than the Ag(110) surface, which is indeed the case. Alloying can result in a *d*-band shift, and thereby a change in reactivity. For our model alloys we find that the *d*-band center of the Pd surface atoms is essentially unchanged compared to the pure Pd(110) surface. The *d*-band center of the Ag surface atom (model A) is shifted 0.55 eV up in energy compared to the pure Ag(110) surface. Methanol would therefore be expected to bind with the same strength to a surface Pd atom compared to adsorption on the pure Pd(110) surface, and stronger to a surface Ag atom (model A) compared to the pure Ag(110) surface, which is exactly what we found.

We end with a brief discussion on the nature of the methanol-substrate bond. The highest occupied orbital of methanol has a lone pair character, mainly localized on the O atom and composed of O 2*p* states perpendicular to the COH molecular plane. Like the water molecule, methanol has a static dipole in the COH plane. The bonding mechanism for methanol is then either a physical interaction via the static dipole, or chemisorption involving the lone pair orbital. A dipole interaction would favour a perpendicular orientation of the molecule with the COH plane parallel to the surface normal. However, we find a preferred orientation with the COH plane at an angle of 40º with the surface normal. This suggests that the lone pair orbital is involved in the interaction. Fig. 8 shows the density of states projected onto the 2*p* states of O and the 4*d* states of the surface Pd atoms. The highest occupied methanol O 2p lone pair orbital is broadened as a result of interactions with the substrate states, and there are indications of the formation of bonding and anti-bonding states expected from hybridization with the Pd 4*d* states. In summary, we find a binding mechanism consistent with the standard picture of a lone pair interaction via the methanol O atom.

Conclusions

On Pd(110) two different methanol species were identified upon adsorption at 100K and subsequent heating up on 200K from high resolution photoelectron spectroscopy measurements. The species with lowest C1s core level binding energy was remaining at the surface for low methanol coverage. The adsorption and decomposition behavior of methanol on a Ag/Pd(110) surface alloy formed by depositing Ag on Pd(110) at elevated temperature was similar to that of the pure Pd(110) surface, indicating that small amounts of silver in the outermost Pd(110) surface is not significantly influencing the behavior of methanol at this surface. DFT calculations on selected surface alloy models support this interpretation.

Acknowledgements

This work was supported by the Research Council of Norway, through project no. 158516/S10, NANOMAT (A. Ramachandran and T. H. Andersen) and project no 148869/V30 (I.-H. Svenum). This work was also supported by the European Community - Research Infrastructure Action under the FP6 "Structuring the European Research Area" Programme (through the Integrated Infrastructure Initiative "Integrating Activity on Synchrotron and Free Electron Laser Science"). Computing time was granted through the Norwegian Metacenter for Computer Science (NOTUR). The support of the MAX-lab staff is gratefully acknowledged.

References

[1] Y. Kato, C.Y. Liu, K.-I. Otsuka, Y. Okuda and Y. Yoshizawa,Progress in Nuclear Energy, 2005. **47**(1-4): p. 504-511.

[2] Y. Kato, K. Otsuka and C.Y. Liu,Chemical Engineering Research and Design, 2005. **83**(7): p. 900-904.

[3] Y. Kato, Otsuka, Ken-ichiro, Ryu, Junichi,Progress in Nuclear Energy, 2008. **50**(2-6): p. 417-421.

[4] J.R. Lattner and M.P. Harold,Applied Catalysis B: Environmental, 2005. **56**(1-2): p. 149-169.

[5] E. Antolini, T. Lopes and E.R. Gonzalez,Journal of Alloys and Compounds, 2008. **461**(1-2): p. 253-262.

[6] B. Emonts, J. Bøgild Hansen, H. Schmidt, T. Grube, B. Höhlein, R. Peters and A. Tschauder,Journal of Power Sources, 2000. **86**(1-2): p. 228-236.

[7] Y. Men, G. Kolb, R. Zapf, D. Tiemann, M. Wichert, V. Hessel and H. Löwe,International Journal of Hydrogen Energy, 2008. **33**(4): p. 1374-1382.

[8] L. Alejo, R. Lago, M.A. Peña and J.L.G. Fierro,Applied Catalysis A: General, 1997. **162**(1-2): p. 281-297.

[9] J. Agrell, G. Germani, S.G. Järås and M. Boutonnet,Applied Catalysis A: General, 2003. **242**(2): p. 233-245.

[10] M.L. Cubeiro and J.L.G. Fierro,Journal of Catalysis, 1998. **179**(1): p. 150-162.

[11] I. Eswaramoorthi and A.K. Dalai,International Journal of Hydrogen Energy. In Press, Corrected Proof.

[12] M.S. Wilson,International Journal of Hydrogen Energy. In Press, Corrected Proof.

[13] J.C. Brown and E. Gulari,Catalysis Communications, 2004. **5**(8): p. 431-436.

[14] L. Pettersson and K. Sjöström,International Journal of Hydrogen Energy, 1991. **16**(10): p. 671-676.

[15] A.D. Schmitz, D.P. Eyman and K.B. Gloer,Energy & Fuels, 1994. **8**(3): p. 729-740.

[16] D.R. Palo, R.A. Dagle and J.D. Holladay,Chemical Reviews, 2007. **107**(10): p. 3992-4021.

[17] J.R. Rostrup-Nielsen and T. Rostrup-Nielsen,CATTECH, 2002. **6**(4): p. 150-159.

[18] N. Iwasa, S. Masuda, N. Ogawa and N. Takezawa,Applied Catalysis A: General, 1995. **125**(1): p. 145-157.

[19] A.K. M. Marczewski, R. Peplonski and M. Pawula,React. Kinet. Catal. Lett., 1983: p. 241.

[20] S. Shiizaki, I. Nagashima, Y. Matsumura and M. Haruta,Catalysis Letters, 1998. **56**(4): p. 227-230.

[21] R.J. Behm, K. Christmann, G. Ertl and M.A. Van Hove,The Journal of Chemical Physics, 1980. **73**(6): p. 2984-2995.

[22] J. Shu, B.P.A. Grandjean, A. Van Neste and S. Kaliaguine The Canadian Journal of Chemical Engineering, 1991. **69**: p. 1036.

[23] G.J. Grashoff, C.E. Pilkington, C.W. Corti.,Plat. Met. Rev., 1983. **27**: p. 157.

[24] A.K.M. Fazle Kibria, T. Tanaka, Y. Sakamoto.,Int. J. Hydrogen Energy., 1998. **23**(10): p. 891.

[25] Knapton A.G.,Plat. Met. Rev., 1977. **21**: p. 44.
[26] K. Hou and R. Hughes,Journal of Membrane Science, 2002. **206**(1-2): p. 119-130.
[27] O. Rodríguez de la Fuente, M. Borasio, P. Galletto, G. Rupprechter and H.J. Freund,Surface Science, 2004. **566-568**(Part 2): p. 740-745.
[28] R. Schennach, A. Eichler and K.D. Rendulic,The Journal of Physical Chemistry B, 2003. **107**(11): p. 2552-2558.
[29] M. Borasio, O. Rodriguez de la Fuente, G. Rupprechter and H.-J. Freund,The Journal of Physical Chemistry B, 2005. **109**(38): p. 17791-17794.
[30] M. Morkel, V.V. Kaichev, G. Rupprechter, H.-J. Freund, I.P. Prosvirin and V.I. Bukhtiyarov,The Journal of Physical Chemistry B, 2004. **108**(34): p. 12955-12961.
[31] L.J. Richter and W. Ho,The Journal of Chemical Physics, 1985. **83**(5): p. 2569-2582.
[32] S.J. Pratt, D.K. Escott and D.A. King,The Journal of Chemical Physics, 2003. **119**(20): p. 10867-10878.
[33] Ratna Shekhar, Mark A. Barteau,Catalysis Letters, 1995. **31**(2-3): p. 221-237, and references cited therein.
[34] R. Neubauer, C.M. Whelan, R. Denecke and H.P. Steinrück,Surface Science, 2002. **507-510**: p. 832-837.
[35] E. Demirci and A. Winkler,Journal of Vacuum Science & Technology A: Vacuum, Surfaces, and Films, 2008. **26**(1): p. 78-82.
[36] A.K. Bhattacharya, M.A. Chesters, M.E. Pemble and N. Sheppard,Surface Science, 1988. **206**(1-2): p. L845-L850.
[37] R.P. Holroyd and M. Bowker,Surface Science, 1997. **377-379**: p. 786-790.
[38] M. Rebholz, V. Matolin, R. Prins and N. Kruse,Surface Science, 1991. **251-252**: p. 1117-1122.
[39] J.L. Davis and M.A. Barteau,Surface Science, 1987. **187**(2-3): p. 387-406.
[40] T.E. Felter, W.H. Weinberg, G.Y. Lastushkina, P.A. Zhdan, G.K. Boreskov and J. Hrbek,Applications of Surface Science, 1983. **16**(3-4): p. 351-364.
[41] H.G. Jenniskens, P.W.F. Dorlandt, M.F. Kadodwala and A.W. Kleyn,Surface Science, 1996. **357-358**: p. 624-628.
[42] I.E. Wachs and R.J. Madix,Surface Science, 1978. **76**(2): p. 531-558.
[43] R. Zhang and A.J. Gellman,The Journal of Physical Chemistry, 1991. **95**(19): p. 7433-7437.
[44] Q. Dai and A.J. Gellman,Surface Science, 1991. **257**(1-3): p. 103-112.
[45] R. Nyholm, J.N. Andersen, U. Johansson, B.N. Jensen and I. Lindau,Nuclear Instruments and Methods in Physics Research Section A: Accelerators, Spectrometers, Detectors and Associated Equipment, 2001. **467-468**(Part 1): p. 520-524.
[46] S. Doniach, M. Sunjic.,J. Phys. C: Solid State Physics, 1970. **3**: p. 285.
[47] M. Wiklund, A. Jaworowski, F. Strisland, A. Beutler, A. Sandell, R. Nyholm, S.L. Sorensen and J.N. Andersen,Surface Science, 1998. **418**(1): p. 210-218.
[48] S. Surnev, M. Sock, M.G. Ramsey, F.P. Netzer, M. Wiklund, M. Borg and J.N. Andersen,Surface Science, 2000. **470**(1-2): p. 171-185.
[49] J.P. Perdew, K. Burke and M. Ernzerhof,Physical Review Letters, 1996. **77**(18): p. 3865.

[50] D. Vanderbilt,Physical Review B, 1990. **41**(11): p. 7892.
[51] H.J. Monkhorst and J.D. Pack,Physical Review B, 1976. **13**(12): p. 5188.
[52] J. Neugebauer and M. Scheffler,Physical Review B, 1992. **46**(24): p. 16067.
[53] L. Bengtsson,Physical Review B, 1999. **59**(19): p. 12301.
[54] J.N. Andersen, D. Hennig, E. Lundgren, M. Methfessel, R. Nyholm and M. Scheffler,Physical Review B, 1994. **50**(23): p. 17525.
[55] H. Luth, G.W. Rubloff and W.D. Grobman,Surface Science, 1977. **63**: p. 325-338.
[56] *We have studied the molecular adsorption of methanol on Ag(110). Measurements of the valence band region yield spectral contributions due to methanol at 9.6 eV, 12 eV, 17 eV and 26 eV.*
[57] I.-H. Svenum., Ø. Borck and A. Borg,Surface Science, 2009.
[58] J. Yoshinobu, M. Kawai, S.-I. Tanaka, K. Watanabe, Y. Matsumoto and M. Kamada,Journal of Electron Spectroscopy and Related Phenomena, 1998. **88-91**: p. 665-669.
[59] I.Z. Jones, R.A. Bennett and M. Bowker,Surface Science, 1998. **402-404**: p. 595-598.
[60] I.Z. Jones, R.A. Bennett and M. Bowker,Surface Science, 1999. **439**(1-3): p. 235-248.
[61] M.G. Ramsey, F.P. Leisenberger, F.P. Netzer, A.J. Roberts and R. Raval,Surface Science, 1997. **385**(1): p. 207-215.
[62] H. Conrad, G. Ertl, J. Koch and E.E. Latta,Surface Science, 1974. **43**(2): p. 462-480.
[63] P. Uvdal, P.A. Karlsson, C. Nyberg, S. Andersson and N.V. Richardson,Surface Science, 1988. **202**(1-2): p. 167-182.
[64] J.-W. He and P.R. Norton,The Journal of Chemical Physics, 1988. **89**(2): p. 1170-1176.
[65] A. Wander, P. Hu and D.A. King,Chemical Physics Letters, 1993. **201**(5-6): p. 393-398.
[66] M.A. Chesters, G.S. McDougall, M.E. Pemble and N. Sheppard,Surface Science, 1985. **164**(2-3): p. 425-436.
[67] R. Raval, S. Haq, G. Blyholder and D.A. King,Journal of Electron Spectroscopy and Related Phenomena, 1990. **54-55**: p. 629-638.
[68] R. Raval, S. Haq, M.A. Harrison, G. Blyholder and D.A. King,Chemical Physics Letters, 1990. **167**(5): p. 391-398.
[69] A. Locatelli, B. Brena, S. Lizzit, G. Comelli, G. Cautero, G. Paolucci and R. Rosei,Physical Review Letters, 1994. **73**(1): p. 90.
[70] K.C. Prince and V. Cháb,Journal of Electron Spectroscopy and Related Phenomena, 1990. **52**: p. 61-66.
[71] P. Pervan and M. Milun,Surface Science, 1992. **264**(1-2): p. 135-146.
[72] P. Steiner and S. Hüfner,Solid State Communications, 1981. **37**(1): p. 79-81.
[73] J. Gustafson, L. E. Walle, A. Borg, E. Lundgren, J. N. Andersen. 2009.
[74] C.J. Zhang and P. Hu,The Journal of Chemical Physics, 2001. **115**(15): p. 7182-7186.
[75] R. Jiang, W. Guo, M. Li, D. Fu and H. Shan,The Journal of Physical Chemistry C, 2009. **113**(10): p. 4188-4197.

[76] Q. Sun, Y. Wang, K. Fan and J. Deng,Surface Science, 2000. **459**(1-2): p. 213-222.
[77] B. Hammer, J. K. Nørskov,Adv. Catal., 2000. **45**: p. 71.
[78] T. Bligaard, J. K. Nørskov., *Chemical Bonding at Surfaces and Interfaces*, ed. L.G.M.P. A. Nilson, J.K. Nørskov. 2008: (Amsterdam, Elseveier, 2008).

Figure captions

Figure 1. Schematic drawings of the three different models (A, B, and C) for alloying of Ag into the Pd(110) used for the DFT calculations. The Pd atoms are shown in blue and Ag atoms in white.

Figure 2. C1s photoemission spectra after adsorption of a) 0.5 L methanol and b) 5.0 L methanol on Pd(110) at 100K, followed by heating to the indicated temperatures.

Figure 3. $Pd3d_{5/2}$ core level spectra after adsorption of a) 0.5 L methanol and b) 5.0 L on Pd(110) at 100K followed by heating to the indicated temperatures. The spectrum recorded for clean Pd(110) is included as the lower panel in both a) and b).

Figure 4. Valence band spectra measured after deposition of 0.5L methanol methanol on Pd(110) at 100K and after heating to the specified temperatures. The spectrum recorded for clean Pd(110) is included as the lower panel in both a) and b).

Figure 5. $Pd3d_{5/2}$ core level spectra of clean Pd(110) (lower panel), after deposition of > 0.6ML Ag at 500K and after adsorption of 2.5 L methanol (upper panel).

Figure 6. C1s photoemission spectra after adsorption of a) 0.5 L methanol and b) 5.0 L methanol >0.6 ML Ag/Pd(110) at 100K followed by heating to the indicated temperatures followed by a sequence of spectra from annealing at specified temperatures.

Figure 7. The adsorption geometry of methanol on the model B Ag/Pd(110) surface (see Fig. 1) in top view to the left and side view to the right. The methanol oxygen atom is indicated in red.

Figure 8. Density of states projected onto the 2p states of O (solid line) and the 4d states of Pd surface atoms (dashed line). The energies are given relative to the Fermi level.

Table captions

Table 1. Binding energies (BE) of the C1s core level contributions for a) 0.5L CH_3OH and b) 5.0 L CH_3OH adsorbed on Pd(110) at 100K and after heating to the indicated temperatures.

Table 2. Binding energies (BE) of the C1s core level contributions for 2.5 L CH_3OH adsorbed on >0.6ML Ag/Pd(110) at 100K and after heating to the indicated temperatures.

Table 3. Calculated adsorption energies in units of eV/molecule for methanol adsorption on PdAg(110) model alloys shown in Fig. 1 with Ag in the first (surface model A), second (B), or third (C) layer as well as on clean Pd(110) (D) and clean Ag(110) (E).

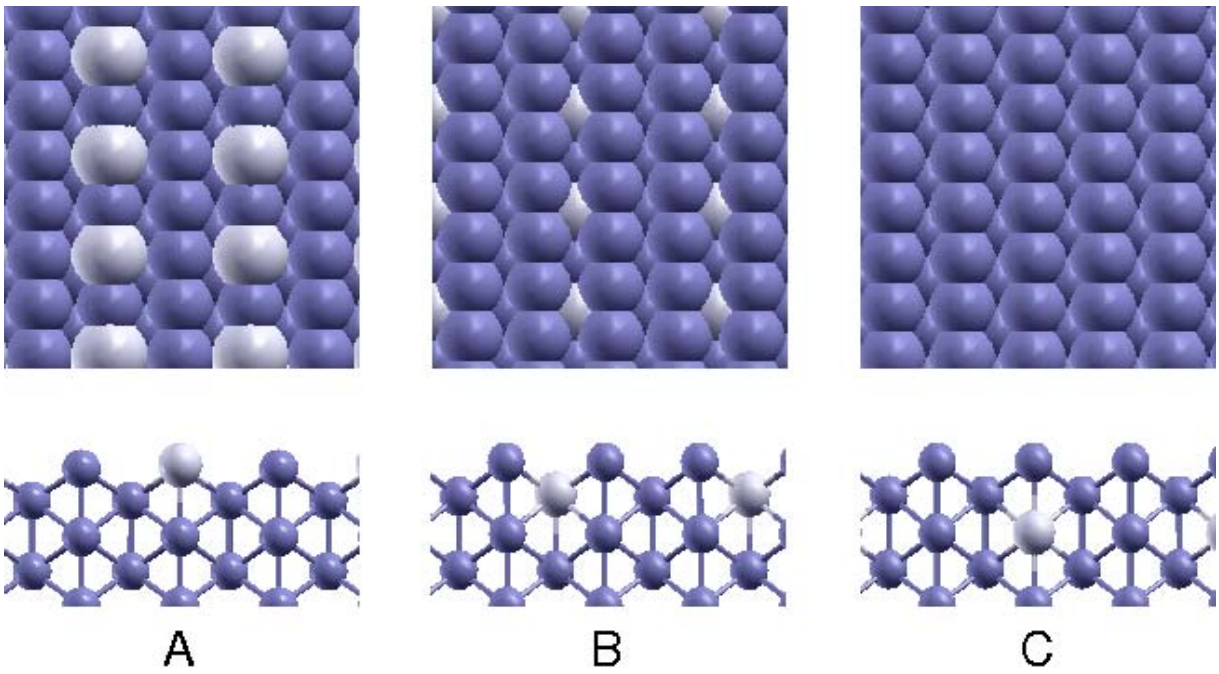

Figure 1

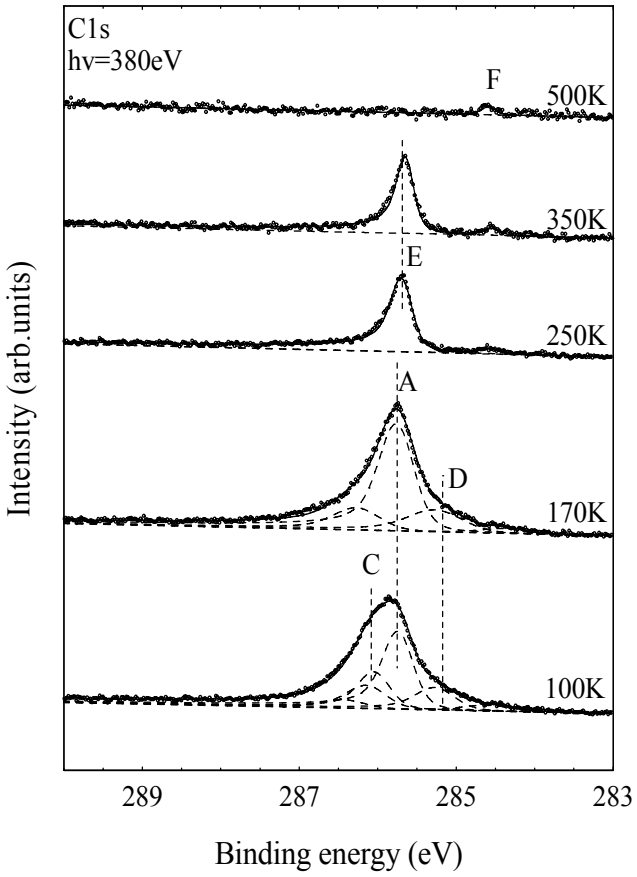
C1s
hv=380eV
F
500K
350K
E
250K
A
D
170K
C
100K
Intensity (arb.units)
289
287
285
283
Binding energy (eV)

Figure 2a

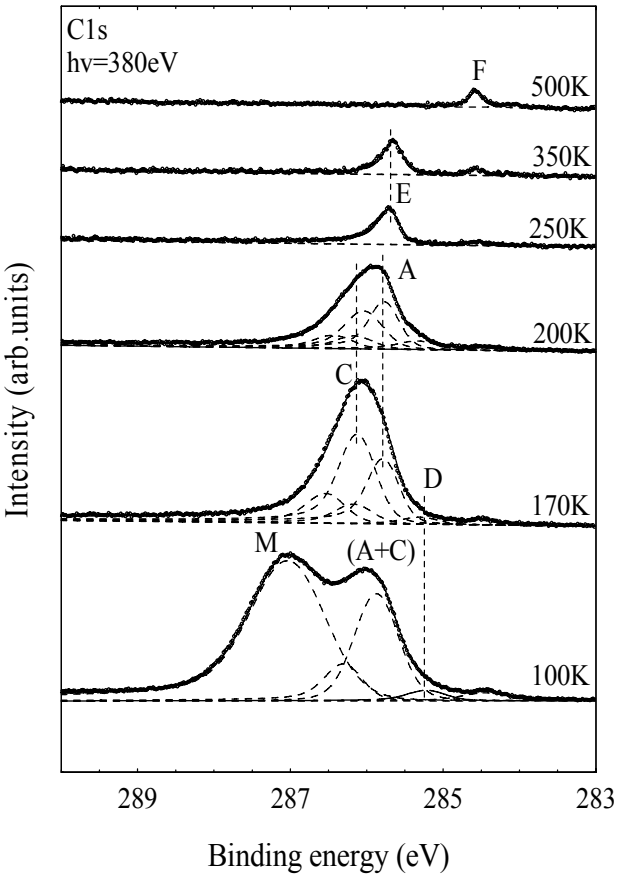
C1s
hv=380eV
F
500K
350K
E
250K
A
200K
C
D
170K
M
(A+C)
100K
Intensity (arb.units)
289
287
285
283
Binding energy (eV)

Figure 2b

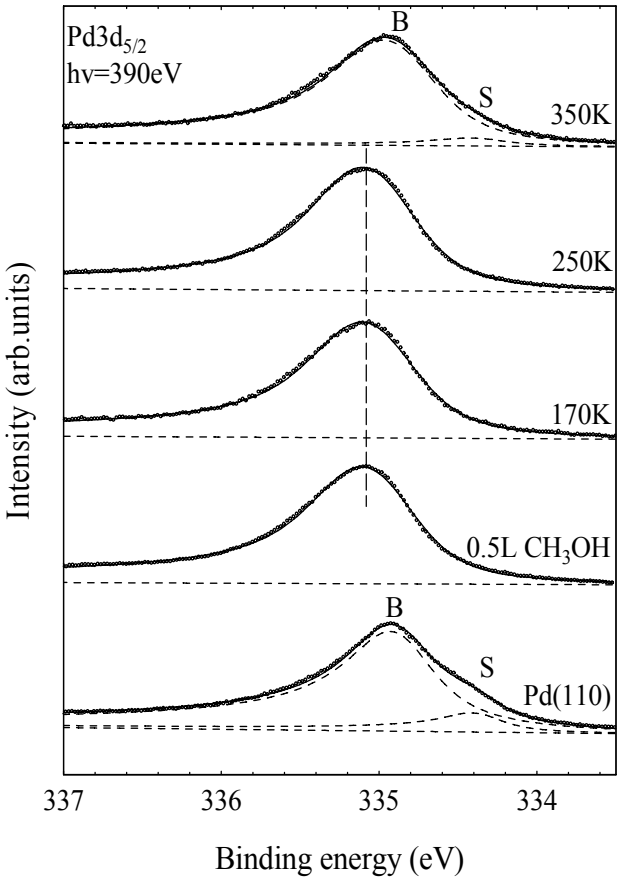
Pd3d5/2
hv=390eV
B
S
350K
250K
170K
0.5L CH3OH
B
S
Pd(110)
Intensity (arb.units)
337
336
335
334
Binding energy (eV)

Figure 3a

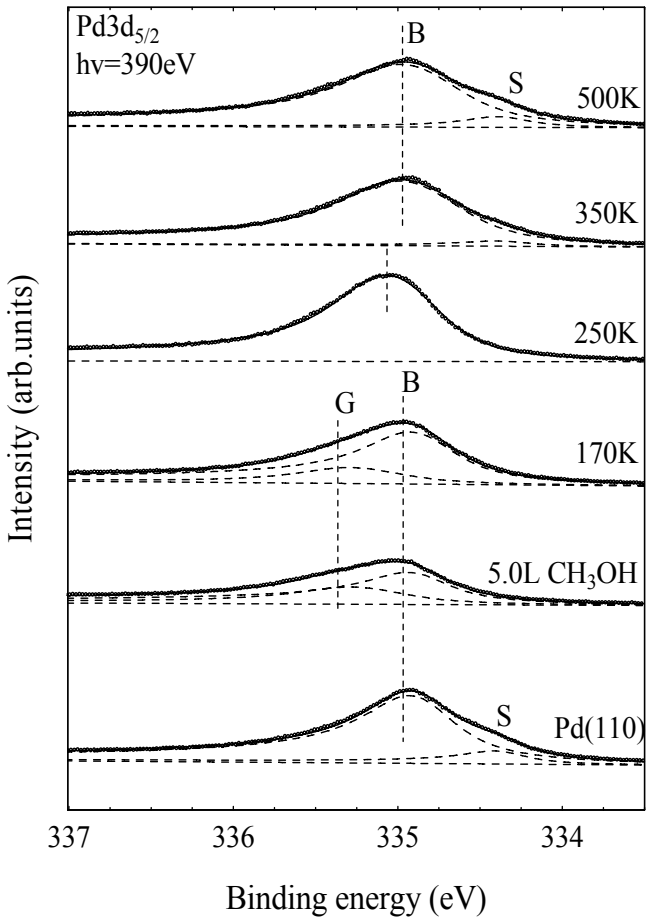
Pd3d5/2
hv=390eV
B
S
500K
350K
250K
G
B
170K
5.0L CH3OH
S
Pd(110)
Intensity (arb.units)
337
336
335
334
Binding energy (eV)

Figure 3b

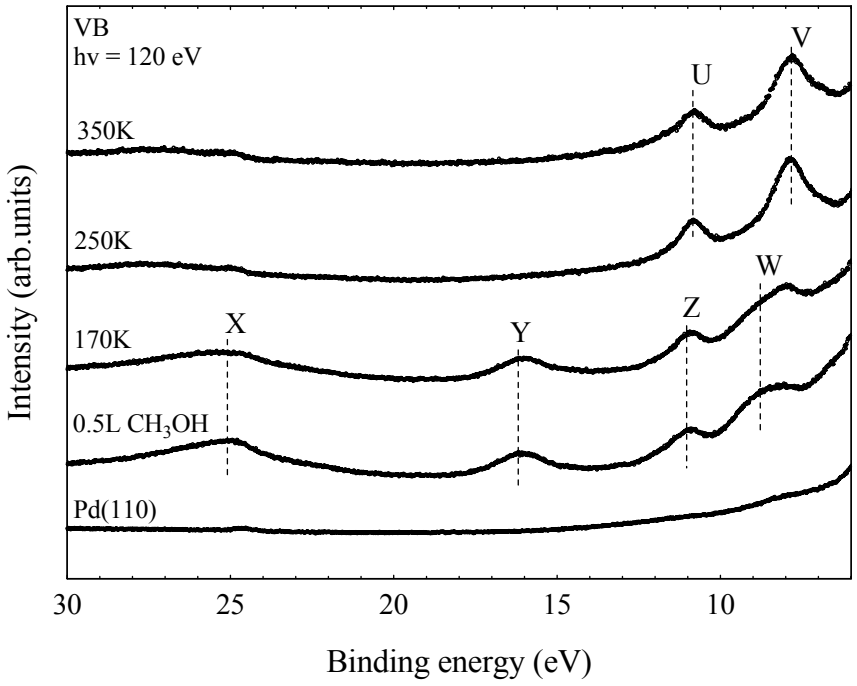
VB
hv = 120 eV
350K
250K
170K
0.5L CH3OH
Pd(110)
U
V
W
X
Y
Z
Intensity (arb.units)
30
25
20
15
10
Binding energy (eV)

Figure 4

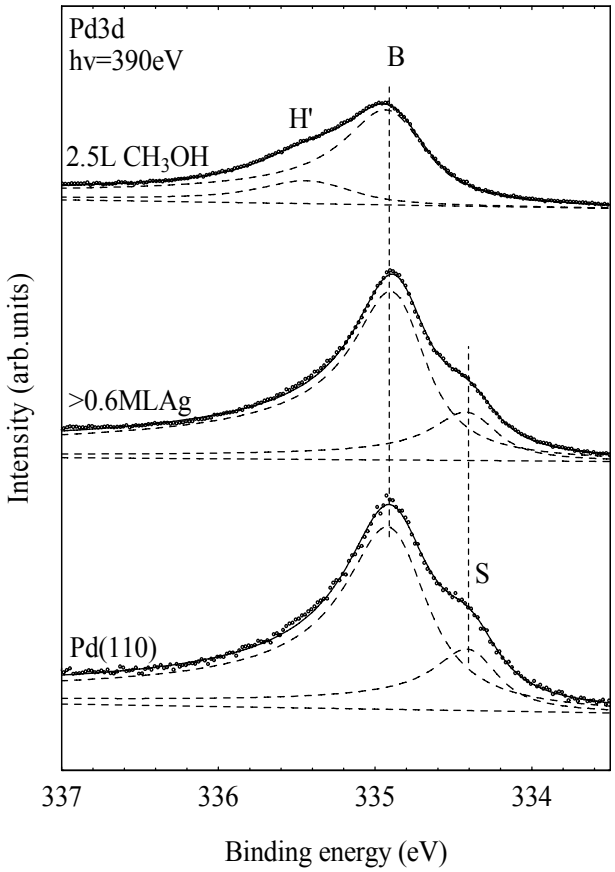
Pd3d
hv=390eV
B
H'
2.5L CH3OH
>0.6MLAg
S
Pd(110)
Intensity (arb.units)
337
336
335
334
Binding energy (eV)

Figure 5

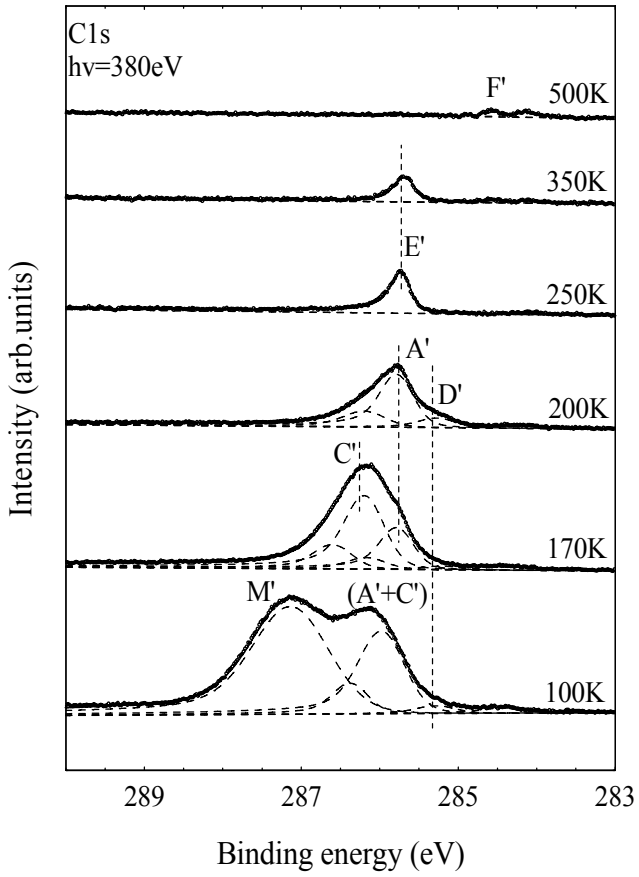
C1s
hv=380eV
F'
500K
350K
E'
250K
A'
D'
200K
C'
170K
M'
(A'+C')
100K
Intensity (arb.units)
289
287
285
283
Binding energy (eV)

Figure 6

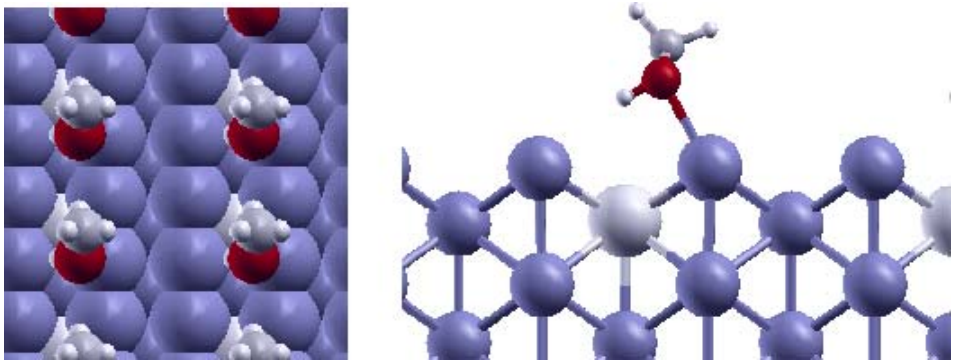

Figure 7

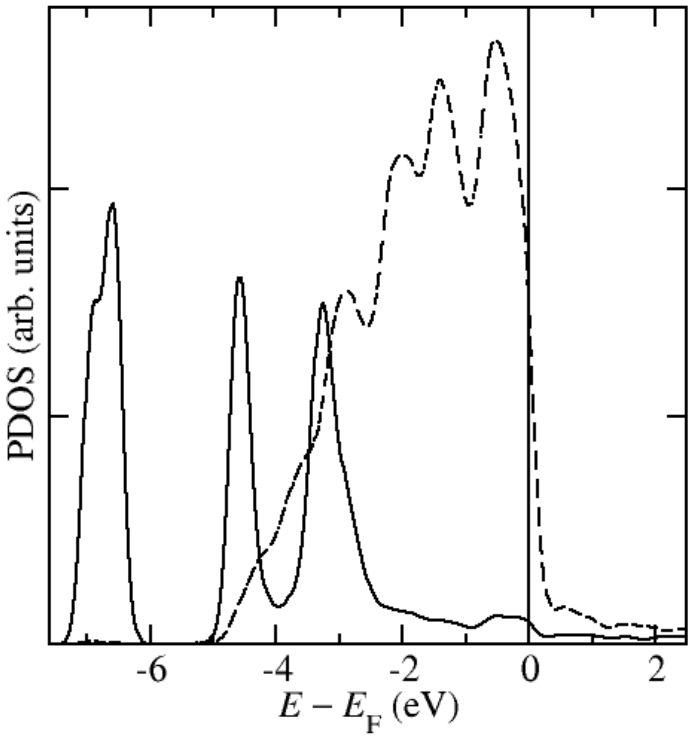

Figure 8

CH_3OH on Pd(110)	Temperature	A	C	D	E	F	M
0.5L	100K	285.72	286.03	285.25	-	284.55	-
	170K	285.72	-	285.25	-	284.55	-
	250K	-	-	-	285.68	284.56	-
	350K	-	-	-	285.63	284.54	-
	500K	-	-	-	-	284.58	-
5.0L	100K	285.88*	285.88*	285.20	-	284.42	286.98
	170K	285.76	286.10	285.27	-	284.45	-
	200K	285.75	286.01	285.29	-	284.41	-
	250K	-	-	-	285.68	284.56	-
	350K	-	-	-	285.64	284.55	-
	500K	-	-	-	-	284.56	-

* Contributions A and C were not fitted separately at this temperature for this methanol exposure.

Table 1.

CH_3OH on Ag/Pd(110)	Temperature	A’	C’	D’	E’	F’	M’
2.5L	100K	285.95*	285.95*	285.25	-	284.44	287.08
	170K	285.76	286.17	285.25	-	284.37	-
	200K	285.76	-	285.25	-	284.25	-
	250K	-	-	-	285.71	284.05	-
	350K	-	-	-	285.66	284.56 284.04	-
	500K	-	-	-	-	284.54 284.08	-

* Contributions A’ and C’ were not fitted separately at this temperature for this methanol exposure.

Table 2.

Surface model	Site	E_{ads} (eV/molecule)
A	Pd on top	0.33
A	Ag on top	0.28
B	Pd on top	0.34
C	Pd on top	0.34
D	Pd on top	0.34
E	Ag on top	0.14

Table 3.

Paper V

Adsorption and decomposition of methylamine on Pd(110) studied by high resolution photoelectron spectroscopy and DFT calculations

T.H. Andersen, A. Ramachandran, Ø. Borck, I.-H. Svenum, L.E. Walle and A. Borg

Manuscript in preparation

Adsorption and decomposition of methylamine on Pd(110) studied by high resolution photoelectron spectroscopy and DFT calculations

T. H. Andersen, A. Ramachandran, Ø. Borck, I.-H. Svenum, L. E. Walle, A. Borg*

Department of Physics, Norwegian University of Science and Technology, Høgskoleringen 5, NO-7491 Trondheim, Norway

Abstract

Methylamine adsorption on Pd(110) and decomposition upon heating to selected temperatures have been investigated by high resolution photoelectron spectroscopy and the resulting adsorption properties of the main resulting species determined by density functional theory. Methylamine is observed to adsorb molecularly at the Pd(110) surface at low temperatures (120 K). In the temperature range 300-350 K CN species are observed formed at the surface and methylamine desorbed. CN remains on the surface up to an annealing temperature of 800 K. The theoretical calculations predict a methylamine on-top adsorption site on Pd(110) with an adsorption energy of 0.40 eV. As seen for other systems methylamine is found to bind to the surface via a lone pair on the N atom. The CN molecule is lying down on surface with the C–N axis along the [001] direction above a second layer Pd atom. The adsorption structure found for CN is in agreement with quantitative structural determinations performed by another group. The binding energy shift between methylamine and cyanide in the C 1s and N 1s states are also calculated. These values are in good agreement with the experimental findings.

Key words: Synchrotron radiation photoelectron spectroscopy, methylamine, cyanide Pd(110), density functional theory

Corresponding author: Anne Borg, anne.borg@phys.ntnu.no

Introduction

The capture of industrial produced CO_2 has attracted a lot of attention lately, due to the threat of climate change from the increased levels of green house gases in the atmosphere [1]. The majority of the industrial CO_2 emission stems from power plants using fossil fuels such as coal and natural gases. The development of zero and near zero emission power plant technologies is becoming an important issue worldwide [2]. In this aspect amines are promising candidates due to their ability for capturing CO_2 [3]. Technology utilizing amines for CO_2 capture are already used in aircraft, submarine and spacecraft technologies [4]. In addition, amines find important applications in surface coatings, adhesion, corrosion inhibition and catalysis [5].

Methylamine (CH_3NH_2) is the simplest primary amine, well suited for addressing interaction of amine groups with metal surfaces. The adsorption of methylamine have been studied experimentally on several transition metal surfaces including Cr(100), Cr(111) [6], Ni(100) [7], Ni(111) [8, 9], Cu(110) [10], Ru(001) [11], Rh(111) [12], Pd(111) [13], W(100) [14], and Pt(100) [15] and Pt(111) [16, 17]. Methylamine adsorbs molecularly on these surfaces at low temperature. It is assumed to bind to metal surfaces through the nitrogen lone pair. A similar bonding mechanism is also reported for metal oxide surfaces [18]. Methylamine is found to be stable on some surfaces above room temperature before decomposing. On Cu(110), however, only desorption of molecular methylamine was observed, indicating that no other decomposition products were formed at this surface [10]. Decomposition of methylamine may occur through dehydrogenation producing CN at the surface, or via C–N bond scission, yielding hydrocarbons, H_2 and N_2 as the final desorption products. The former reaction pathway often results in desorption of H_2, HCN and C_2N_2. The production of gaseous HCN and C_2N_2 indicates that CN_{ads} have formed at the surface. At the (111) surfaces of Ni [8,9], Rh [12] and Pd [13] as well as on Pt(111) [16] dehydrogenation of methylamine to CN is reported to occur. CN remains intact at the surface in certain temperature intervals. Whereas, at Cr(100), Cr(111) [6], Ni(100), W(100) [14] and Pt(100) [15]C-N bond breaking has been found to dominate. A combination of both decomposition pathways were observed at Ru(001) [11]. Contradicting results have been reported for Pt(111), where one study observed mainly dehydrogenation to CN [16] while another observed both decomposition pathways [17].

Theoretical studies addressing the interaction of methylamine with metal surfaces are scarce. Methylamine adsorption has been studied on Ni(111) [19] and transition metal surfaces [20],

with a focus on the composition and decomposition reactions on these surfaces.

In the present study we investigate the interaction of methylamine with the Pd(110) surface and the decomposition behaviour, using high resolution photoemission spectroscopy (HR-PES) and density functional theory (DFT). We find that methylamine adsorbs molecularly at 120 K. Upon heating dehydrogenation is the only reaction involved in the decomposition of methylamine on Pd(110), where the production of adsorbed CN mainly occurs in the temperature regime 300 K to 350 K. DFT calculations are used to further address the interaction and bonding mechanism of methylamine and the decomposition product CN with the Pd(110) surface. In addition, calculated binding energy shifts in the C 1s and N 1s core levels due to methylamine and CN are compared to the experimental values.

Experimental

High-resolution photoelectron spectroscopy experiments were performed at beam line I311 of the MAX II synchrotron radiation source in Lund, Sweden. This beam line is equipped with a modified SX-700 monochromator and a large Scienta type hemispherical electron energy analyzer (SCIENTA SES200) [21]. The base pressure in the UHV system was $\leq 3x10^{-10}$ mbar.

The Pd(110) crystal was cleaned by cycles of sputtering, heating in oxygen and subsequent annealing. This procedure gave well-defined, clean surfaces as judged from LEED patterns and photoemission measurements of the C1s core level region. Methylamine (2.0, AGA) was used without further purification. As noted by Hwang et al. [12] we experienced how strongly CH_3NH_2 adsorbs on the UHV chamber walls and pumping down after exposure was time consuming. The actual exposures are therefore difficult to estimate and we used for this reason saturation coverage only. The Pd(110) was exposed to methylamine at 120 K. The reaction of methylamine was investigated as function of temperature by flashing the sample to higher temperatures.

All PES spectra were recorded at normal emission and with the sample kept at 120 K. The C1s core level spectra were recorded at photon energy 380 eV and the $Pd3d_{5/2}$ core level at 390 eV. The corresponding experimental resolution was about 110 meV. The N1s core level was measured using an photon energy of 500 eV, with an experimental resolution better than

150 meV. The binding energy was calibrated by recording the Fermi edge immediately after the core level regions.

The spectra were fitted with a Doniach-Šunjić lineshape [22] convoluted with a Gaussian distribution. In fitting of C1s and N1s spectra, the Lorentzian lifetime broadening was set to 100 ± 10meV. Moreover, the background was represented by a linear function with adjustable slope. The fitted binding energy values were allowed to vary ±10 meV. All spectra were normalized to the same intensity at the low BE side of the core-level signal except for the N1s spectra, where the BE interval was measured too short. For these spectra normalization was performed at the high BE side of the signal.

Computational

The DFT calculations reported here were performed using the DACAPO code [23]. The exchange and correlation effects are taken into account using the Perdew-Burke-Ernzerhof (PBE) version [24] of the generalised gradient approximation (GGA). The ionic cores and their interactions with the valence electrons were described by ultrasoft pseudopotentials [25]. To calculate core level shifts, pseudopotentials for core-exited atoms were constructed using the same parameters as those used for the corresponding ground state atom. The calculations were performed using a plan-wave basis with a kinetic energy cut off of 340 eV. Initial calculations to determine the equilibrium bulk structure of Pd using a 12x12x12 Monkhorst-Pack k-point sampling gave a value of 3.98 Å for the Pd bulk lattice constant. This is an overestimate of 2.3% compared to the experimental value, but compares well with previously reported theoretical values where the GGA approximation has been used [26].

The Pd(110) surface was represented by periodically repeated slabs constructed using the calculated bulk lattice constant. The slabs were separated by a 14 Å vacuum gap. The majority of the adsorbate-substrate calculations were performed using a (2x2) supercell and a five-layer slab, with a k-point sampling grid of 6x8x1. The minimum-energy adsorption geometries were determined by placing the adsorbate in the high-symmetry sites on the Pd(110) surface, and allowing the atoms of the adsorbate and three uppermost layers of the slab to relax freely until the residual forces on each atom were less than 0.02 eV/Å. An extensive set of different orientations of the adsorbate with respect to the surface were explored. The artificial electric field created by the asymmetry of the adsorption system

was compensated by a self-consistently determined dipole correction applied in the vacuum region [27, 28].

The reported adsorption energies per molecule were calculated from

$$E_{ads} = -(E_{SM} - E_S - E_M),$$

where E_{SM} is the total energy of the adsorbate-substrate system, E_S is the energy of a clean surface slab, and E_M is the energy of an isolated molecule. With this definition, a positive adsorption energy indicates stabilisation. The adsorption energies were obtained using the RPBE functional [29], as this has been shown to provide an improved description of the chemisorption energetics of molecules on transition metal surfaces.

Results and discussion

The C 1s and N 1s spectra measured after exposing the Pd(110) surface to methylamine at 120 K to saturation coverage and subsequent heating to selected temperatures are shown in Figs. 1 and 2, respectively. Binding energies of all observed spectral contributions are summarized in Table 1 for the C 1s spectra and Table 2 for the N 1s spectra. The unidentified contributions are labelled $C^x_{species}$ and $N^y_{species}$. Upon saturation coverage of methylamine at 120 K, the intensity of the $Pd3d_{5/2}$ signal (spectra not shown) decreases by only 27 % indicating that no thick layer of CH_3NH_2 was formed on Pd(110) by the adsorption at this temperature. In addition, the $Pd3d_{5/2}$ surface component disappeared and a broadening to the high binding energy side of the Pd bulk contribution was observed. Adsorption at 120 K results in one main contribution in the spectra for both the C 1s (285.97 eV) and N1s (399.39 eV) core levels, as seen in the lower panels of Figs. 1 and 2. These contributions are assigned to molecular methylamine adsorbed on the surface, and their binding energies agree well with previous values reported for molecularly adsorbed CH_3NH_2 on Pd(111) [13]. Two minor contributions, shifted 1.61 eV and 2.64 eV to lower binding energies relative to the main contribution, are observed in the C 1s spectrum indicating that a small fraction of the methylamine molecules decomposes upon adsorption at 120 K. These spectral features remain after heating up to 200 K, with a weak increase in the strength of the C 1s contribution at 284.36 eV. These small peaks disappeared upon heating to 400 K. The spectral range recorded for the N1s was increased after heating to 200 K. It cannot be excluded that the weak

contribution observed at 397.29 eV after annealing at this temperature already appeared upon the initial deposition of methylamine together with the small contributions in the C 1s spectrum. Nitrogen containing decomposition products of methylamine are expected to give additional peaks in the N 1s spectra [12, 13].

Upon heating to 300 K some molecular CH_3NH_2 desorbs from the surface judged by the reduced intensity in both the C 1s and N 1s spectra. Moreover, the C 1s main contribution has shifted ~0.35 eV to lower binding energies. At the same time, the N 1s signal, originally at 399.39 eV shifts ~0.17 eV to higher binding energies. The origin of these small changes in binding energies may either be formation of one or more surface intermediates formed by dissociation through removal of one hydrogen atom from the methylamine molecule or interaction of methylamine through lower adsorbate coverage and/or with other decomposition products formed on the surface. On Pd(111), a fraction of the methylamine molecules desorbed upon heating to 275 K [13]. No changes in the binding energies of the methylamine C 1s and N 1s components were found. In the case of methanol adsorption Ni(100) [30], NiAl(110) and Ni_3Al(111) [31] changes in the C1s binding energy have been observed with decreasing methanol coverage upon heating. The changes in binding energy of the methanol component upon heating were interpreted as being due to adsorbate-adsorbate interactions of methanol with the decomposition product H and/or methoxy. In this study, the full width at half maximum (FWHM) of the methylamine C 1s contribution observed at 120 K is reduced upon heating to 300 K, indicating loss of spectral weight which may be arising from the first vibrationally exited state of the C-H stretching mode. Note that the vibrational component is unresolved in the spectra and therefore not included. The FWHM of the methylamine N 1s contribution observed at 120 K is constant upon heating to 200 K, and reduced upon further heating to 300 K. Together with the shift in binding energy, the reduction of the FWHM suggests that methylamine undergoes dehydrogenation upon heating.

A significant change in both the C 1s and N 1s spectra upon heating to 300 K is a new contribution at lower binding energies relative to the signals from molecular CH_3NH_2 appearing in both the C 1s and N 1s spectra. In the C 1s spectra this contribution is shifted 1.85 eV related to the methylamine contribution found at 120 K while the corresponding shift in the N 1s spectrum is 2.36 eV. Successive heating to 350 K changes the surface adsorbates completely. Almost no molecular CH_3NH_2 or slightly decomposed CH_3NH_2 are left on the surface. Instead the contributions appearing after heating to 300 K have increased in intensity.

Formation of CN on Pd(110) upon dissociation of C_2N_2 has been reported to yield a C 1s spectral contribution at 284.20 eV and a N 1s binding energy at 397.15 eV [32]. The binding energies of the C 1s (at 284.12 eV) and N 1s (at 397.03 eV) contributions, originating from heating the methylamine covered Pd(110) surface to 300 K, agree well with the values found by Baraldi et al. [32], and are thus attributed to CN formation through decomposition of methylamine.

As can be seen from the spectra in Figs. 1 and 2 the decomposition of adsorbed CH_3NH_2 to CN on Pd(110) occurs mainly in the temperature range from 300 K to 350 K. In addition, the intensity of the $Pd3d_{5/2}$ signal has increased upon heating to 350 K, the intensity reduction relative to the clean surface was only about 4%. The $Pd3d_{5/2}$ surface contribution was still absent and the overall shape of the spectrum was not significantly changed. The C1s and N1s spectra in Figs. 1 and 2 do not change significantly upon further heating to 400 K and 500 K except for a shoulder being formed at the high binding energy side of the CN contribution in the C1s spectra. This shoulder could be due atomic carbon. Atomic carbon formed from methanol decomposition on Pd(110) was found at a slightly higher binding energy of 284.56 eV [33] compared to 284.38 eV found here. This shoulder disappears upon heating to 800 K The overall spectral intensity for both the carbon and the nitrogen signals is strongly reduced after annealing at this temperature.

The formation of CN from methylamine on Pd(110) is in line with previously reported results for Pd(111) [13], where CN was observed in the temperature range 300 K to 425 K. CN was found to desorb at 500 K while we in our experiments still see some CN after flashing to 800 K. On Pd (110), C_2N_2 was completely transformed into CN upon heating to 220 K [32]. CN remained on the Pd(110) surface after heating at temperatures up to 800 K, though at lower intensity for the highest annealing temperature. Using angle resolved UV photoemission (ARUPS) and temperature programmed desorption (TPD), CN species were found to be stable up to about 650 K on Pd(110), where they started recombining to C_2N_2 with a maximum desorption peak at about 800 K [34]. The reduced intensity we observe in the C 1s and N 1s spectra after heating to 800 K is consistent with these results. Also on Rh(111) methylamine decomposed to CN and was stable on the surface at temperatures up to about 700 K, where it also desorbed as C_2N_2 [12].

DFT were used to determine the preferred adsorption site of methylamine and cyanide (CN) on Pd(110). Methylamine has a lone pair electron located on the N atom. A molecular

adsorption of methylamine is therefore expected to be via the N atom. For this reason we limited our search for the optimum adsorption structure to configurations where the N atom is close to the surface. A series of geometry optimizations were performed from structures where the nitrogen where initially placed on top an outermost Pd layer atom, in the hollow site (on top a second layer Pd atom), and in the short and long bridge sites. From this set of calculations we found that methylamine adsorbs via its nitrogen atom in the on top site with an adsorption energy of 0.40 eV. Figure 3 illustrates the adsorption geometry. The N–Pd nearest neighbour distance in this site is 2.23 Å. The N–H bonds are essentially parallel to the surface plane, while the CN bond axis is tilted by 27° with respect to the surface normal. There are no significant changes in the molecular geometry upon adsorption. The bond lengths are unchanged, while the internal angles open up, but by no more than 2%. The adsorption induced changes in the surface geometry are also relatively small. The Pd atom underneath methylamine is pulled out by 0.05 Å, while the other Pd atoms keep their position relative to the clean surface geometry. The adsorption site preference and geometry for methylamine is very similar to what has been found in previous DFT studies of methylamine on other metal surfaces [19, 20].

To gain some understanding of the bonding mechanism we have calculated the electron density difference. This was obtained by subtracting the electron density of the clean surface and free molecule from the electron density of the adsorbate system. The two former electron densities were calculated using the geometry of the molecule and the surface as found for the adsorbate system. Figure 4 shows a contour plot of the electron density difference in a cross section containing the methylamine C and N atom and the Pd atom that methylamine binds to. Solid lines indicate a gain in electron density, while dashed lines indicate a loss of electron density. The local changes around the N atom and the Pd atom suggests that the lone pair, mainly composed of N 2p states, and Pd 4d are involved in the bonding of methylamine to the surface. There is a localised accumulation of electron density in the bonding region midway between the Pd atom and the N atom suggesting some covalent contribution to the binding. This is supported by the site preference found in our calculations that also indicate some localised character in the bonding mechanism.

CN forms an ordered c(2x2) overlayer on several fcc(110) surfaces [35, 36], including Pd(110) [34]. A general adsorption behaviour has been found for these systems where the CN

species is almost parallel to the surface plane above a second layer layer atom and with the molecular axis along the [001] azimuth [34-36]. The lowest energy adsorption structure found in our DFT calculations is in agreement with the one found experimentally [34]. CN is lying down on the surface with the C–N axis along the [001] direction. The C atom is closer to the surface than the N atom, so that C–N axis is tilted by 26° with respect to the surface plane, in excellent agreement with the experimental value of 25 ± 4° [35, 36]. As illustrated in Fig. 5, the C atom is three-fold coordinated to two outermost Pd layer atoms and one second layer Pd atom. The C-Pd nearest neighbour distance is 2.09 Å. N is two-fold coordinated to the outermost surface layer atoms at a N-Pd nearest neighbour distance of 2.22 Å, close to the corresponding value for adsorbed methylamine. For this geometry the adsorption energy was found to be 1.60 eV calculated relative to a free cyanogen molecule (C_2H_2). The adsorption geometry where CN is lying down, but aligned with the C–N axis along the [-110] direction had a smaller adsorption energy of 1.06 eV. The strongest adsorption energy we found for geometries with the C-N axis parallel to the surface normal was 0.62 eV, with CN adsorbed with the C atom located in the short bridge site. The calculations therefore favour a flat lying orientation of the CN molecule, and the surface structure found experimentally [34]. Fig. 6 show contour plots of three different cuts through the electron density difference. These plots show charge accumulations between the Pd atoms and the adjacent C and N atoms characteristic of local covalent bonds. In addition there is a clear gain of electron density in along the C-N bond axis indicating a charge transfer form the substrate to the molecule. We therefore interpret the bonding mechanism to be a covalent bond with some ionic component.

We have calculated binding energy shifts in the C 1s and N 1s core level for cyanide relative methylamine using the optimum adsorption structures. The geometry has not been relaxed for the core-exited adsorbate system because of the vertical nature of the photoemission process. The calculations predicted a shift of 2.0 eV in the C 1s core level, whereas the shift was 2.7 eV in the N 1s core level. These values are in fair agreement with the experimental results of 1.85 eV and 2.36 eV for the C 1s and N 1s core levels, respectively.

Conclusions

Methylamine adsorbs molecularly on Pd(110) at 120 K. DFT calculations predict that methylamine binds to the surface with the N atom situated in a Pd on top site. An analysis of the electron density difference suggests that methylamine binds to the surface via the N lone pair. Upon heating to 300 K cyanide starts forming, and at 350 K almost all methylamine has transformed into cyanide. CN remains at the Pd(110) surface upon heating to 800 K, however, from 500 K to 800 K desorption starts taking place. As determined by DFT calculations CN adsorbs preferentially lying down on surface with the C–N axis along the [001] direction above a second layer Pd atom. The C atom is closer to the surface than the N atom, resulting in a tilt of the C-N axis by 26° with respect to the surface plane. Electron density difference plots of CN on the surface indicate a covalent bonding mechanism with an ionic contribution.

Acknowledgments

This work was supported by the Research Council of Norway, through project no. 158516/S10, NANOMAT (T. H. Andersen and A. Ramachandran) and project no 148869/V30 (I.-H. Svenum). This work was also supported by the European Community - Research Infrastructure Action under the FP6 "Structuring the European Research Area" Programme (through the Integrated Infrastructure Initiative "Integrating Activity on Synchrotron and Free Electron Laser Science"). Computing time was granted through the Norwegian Metacenter for Computer Science (NOTUR). The support of the MAX-lab staff is gratefully acknowledged.

References

[1] R. Idem, Tontiwachwuthikul, P.,Ind. Eng. Chem. Res., 2006. **45**: p. 2413.
[2] *IPCC Special Report on Carbon dioxide Capture and Storage*. 2005.
[3] A. B. Rao, Rubin, Edward S.,Environmental Science & Technology, 2002. **36**(20): p. 4467-4475.
[4] T. F. S. Satyapal, J. Trela, J. Strange,Energy Fuels, 2001. **15**: p. 250.
[5] Lawrence S.A., *Synthesis, Properties and Applications, Cambridege University Press, Cambridge*. 2004.
[6] A. G. Baca, M. A. Schulz and D. A. Shirley,The Journal of Chemical Physics, 1985. **83**(11): p. 6001-6008.
[7] C.-C. Chang, C. Khong and R. Saiki. in *39th National Symosium of the American Vacuum Society*. 1993. Chicago, Illinois (USA): AVS.
[8] I. Chorkendorff, J. J. N. Russell and J. J. T. Yates,The Journal of Chemical Physics, 1987. **86**(8): p. 4692-4700.
[9] D. E. Gardin and G. A. Somorjai,The Journal of Physical Chemistry, 1992. **96**(23): p. 9424-9431.
[10] F. Maseri, A. Peremans, J. Darville and J. M. Gilles,Journal of Electron Spectroscopy and Related Phenomena, 1990. **54-55**: p. 1059-1064.
[11] D. F. Johnson, Y. Wang, J. E. Parmeter, M. M. Hills and W. H. Weinberg,Journal of the American Chemical Society, 1992. **114**(11): p. 4279-4290.
[12] S. Y. Hwang, A. C. F. Kong and L. D. Schmidt,The Journal of Physical Chemistry, 1989. **93**(26): p. 8327-8333.
[13] J. J. Chen and N. Winograd,Surface Science, 1995. **326**(3): p. 285-300.
[14] K. A. Pearlstine and C. M. Friend,Journal of the American Chemical Society, 1986. **108**(19): p. 5842-5847.
[15] P. A. Thomas and R. I. Masel,Journal of Vacuum Science & Technology A: Vacuum, Surfaces, and Films, 1987. **5**(4): p. 1106-1108.
[16] S. Y. Hwang, E. G. Seebauer and L. D. Schmidt,Surface Science, 1987. **188**(1-2): p. 219-234.
[17] M. E. Bridge and J. Somers,Vacuum, 1988. **38**(4-5): p. 317-320.
[18] O. Borck, P. Hyldgaard and E. Schroder,Physical Review B (Condensed Matter and Materials Physics), 2007. **75**(3): p. 035403-7.
[19] C. Oliva, C. van den Berg, J. W. Niemantsverdriet and D. Curulla-Ferré,Journal of Catalysis, 2007. **245**(2): p. 436-445.
[20] J. Li, R.-F. Li and G.-C. Wang,The Journal of Physical Chemistry B, 2006. **110**(29): p. 14300-14303.
[21] R. Nyholm, J. N. Andersen, U. Johansson, B. N. Jensen and I. Lindau,Nuclear Instruments and Methods in Physics Research Section A: Accelerators, Spectrometers, Detectors and Associated Equipment, 2001. **467-468**(Part 1): p. 520-524.
[22] S. Doniach and M. Sunjic,Journal of Physics C: Solid State Physics, 1970. **3**(2): p. 285-291.
[23] The DACAPO code can be downloaded at http://www.fysik.dtu.dk/campos.
[24] J. P. Perdew, K. Burke and M. Ernzerhof,Physical Review Letters, 1996. **77**(18): p. 3865.
[25] D. Vanderbilt,Physical Review B, 1990. **41**(11): p. 7892.
[26] S. S. Alexandre, E. Anglada, J. M. Soler and F. Yndurain,Physical Review B (Condensed Matter and Materials Physics), 2006. **74**(5): p. 054405-7.
[27] J. Neugebauer and M. Scheffler,Physical Review B, 1992. **46**(24): p. 16067.
[28] L. Bengtsson,Physical Review B, 1999. **59**(19): p. 12301.

[29] B. Hammer, L. B. Hansen and J. K. Nørskov,Phys. Rev. B, 1999. **59**: p. 7413.
[30] R. Neubauer, C. M. Whelan, R. Denecke and H. P. Steinrück,Surface Science, 2002. **507-510**: p. 832-837.
[31] I.-H Svenum, Ø.Borck, A. Borg,Surface Science, Submitted., 2009.
[32] A. Baraldi, Lizzit, S. Ramsey, M. G. Netzer, F. P.,Surface Science, 1998. **416**(1-2): p. 214-225.
[33] A Ramachandran, T.H. Andersen, Ø. Borck, I.-H. Svenum, L.E. Walle, A. Borg.,Manuscript in preparation., 2009.
[34] M. G. Ramsey, G. Rosina, F. P. Netzer, H. B. Saalfeld and D. R. Lloyd,Surface Science, 1989. **218**(2-3): p. 317-330.
[35] M. J. Knight, J. Robinson and D. P. Woodruff,Surface Science, 2005. **580**(1-3): p. 145-152.
[36] F. Bondino, A. Baraldi, H. Over, G. Comelli, P. Lacovig, S. Lizzit, G. Paolucci and R. Rosei,Physical Review B, 2001. **64**(8): p. 085422.

Figure captions

Figure 1. C 1s photoemission spectra from Pd(110) after adsorbing a saturation coverage of methylamine at 120 K and heating to the indicated temperatures. The spectra are measured with a photon energy of 380 eV. The vertical dashed lines indicate the number of contributions to each spectrum.

Figure 2. N 1s photoemission spectra from Pd(110) after adsorbing a saturation coverage of methylamine at 120 K and heating to the indicated temperatures. The spectra are measured with a photon energy of 500 eV. The vertical dashed lines indicate the number of contributions to each spectrum.

Figure 3. a) Top view and b) side view illustrations of methylamine adsorbed in the on top site on the Pd(110) surface.

Figure 4. Electron density difference contour plot for methylamine on Pd(110) in a plane through the C and N atoms of methylamine and the bonding Pd atom. Solid lines indicate gain in electron density while dashed lines indicate loss. The contours are drawn at densities $\pm 0.005 \times 2^k$ e/Å^3 for k = 0,1...,6.

Figure 5. a) Top view and b) side view illustration of CN adsorbed on Pd(110) where the C–N axis is aligned along the [001] direction above a second layer Pd atom.

Figure 6. Electron density difference contour plot for methylamine on Pd(110) in planes through a) the C and N atoms of CN and the second layer Pd atom below the C atom, b) the C of CN and two Pd surface atoms and c) the N atom of CN and two Pd surface atoms. Solid lines indicate gain in electron density while dashed lines indicate loss. The contours are drawn at densities $\pm 0.005 \times 2^k$ e/Å^3 for k = 0,1...,6.

Table captions

Table 1. Adsorbate C 1s core level binding energies found from Pd(110).

Table 2. Adsorbate N 1s core level binding energies found from Pd(110).

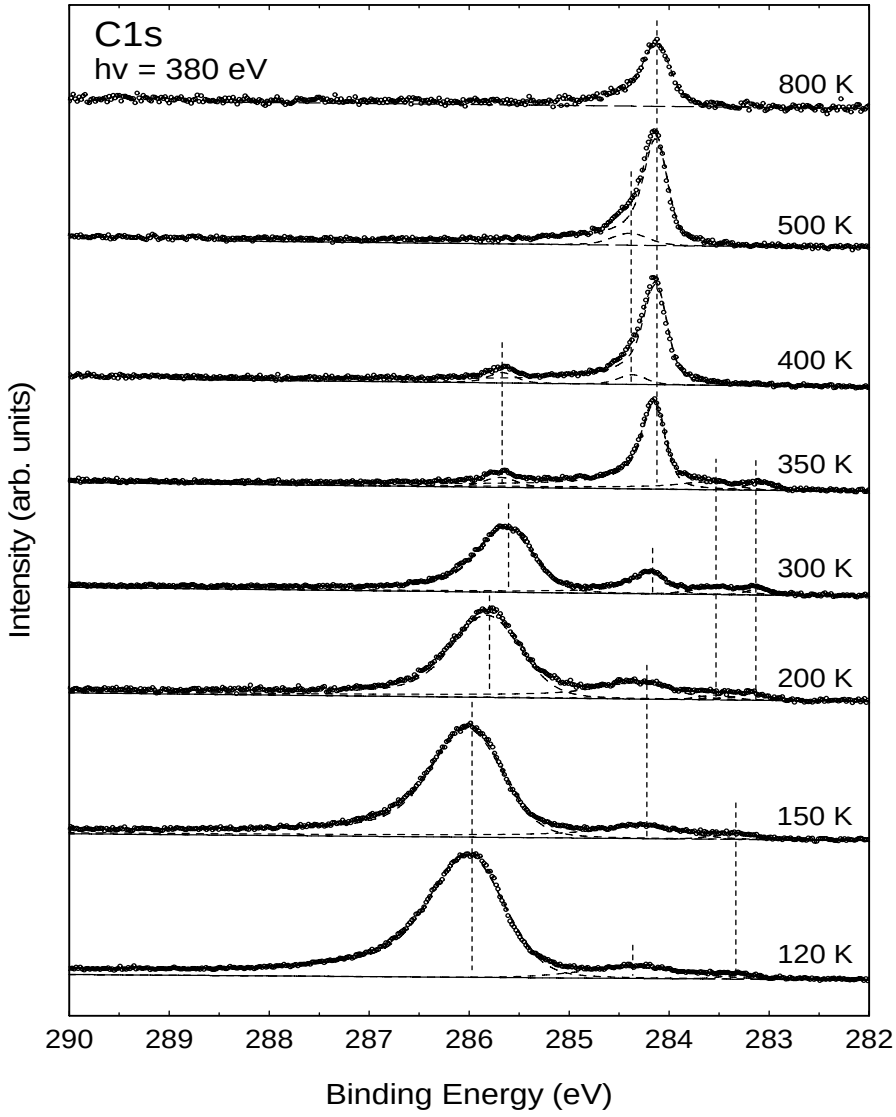
C1s
hv = 380 eV
800 K
500 K
400 K
350 K
300 K
200 K
150 K
120 K
Intensity (arb. units)
290
289
288
287
286
285
284
283
282
Binding Energy (eV)

Figure 1

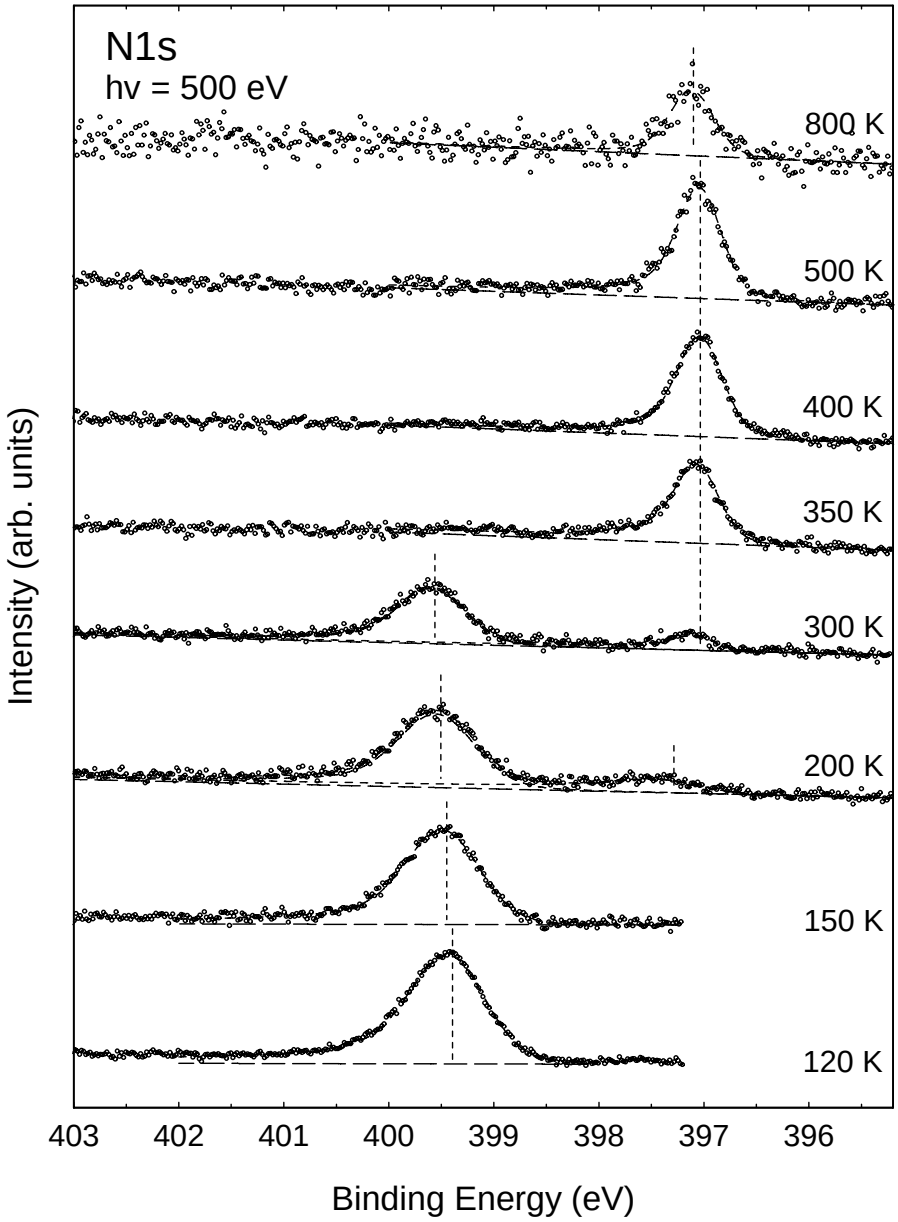
N1s
hv = 500 eV
800 K
500 K
400 K
350 K
300 K
200 K
150 K
120 K
Intensity (arb. units)
403
402
401
400
399
398
397
396
Binding Energy (eV)

Figure 2

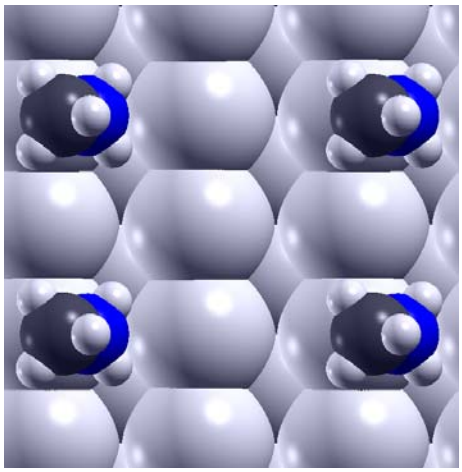

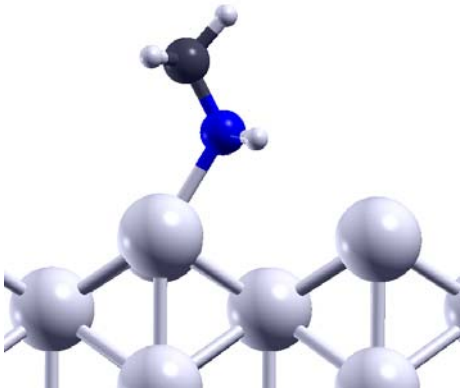

Figure 3 (a) and (b)

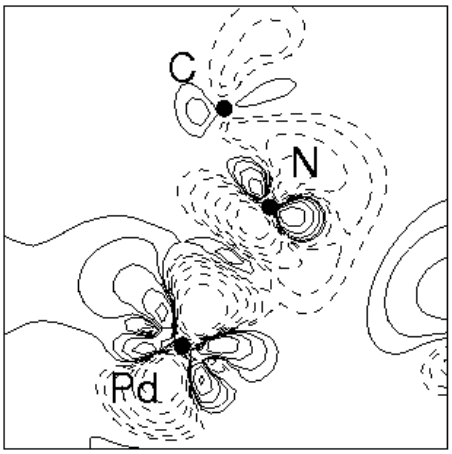

Figure 4

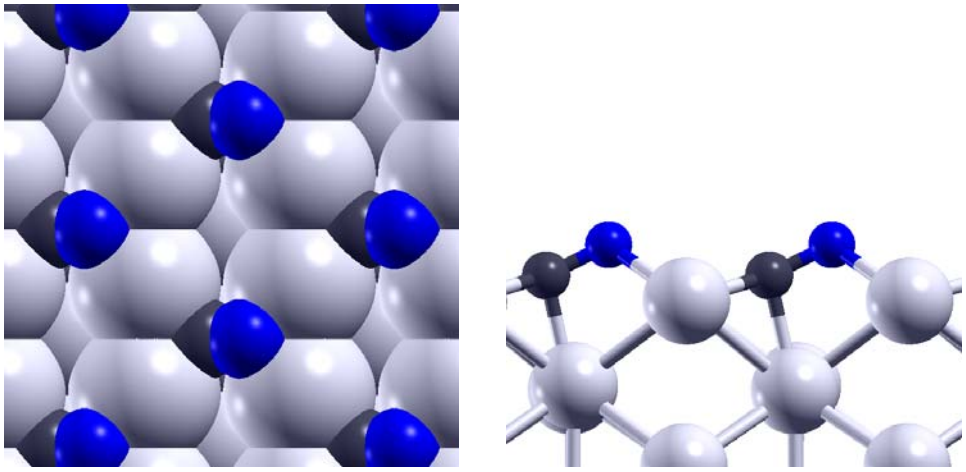

Figure 5 (a) and (b)

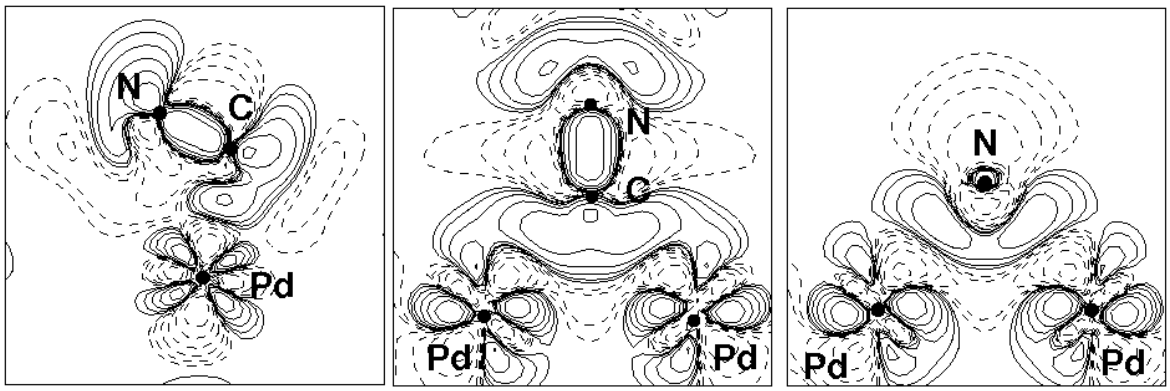

Figure 6 (a), (b) and (c)

Temperature (K)	CH_3NH_2	$C^1_{species}$	$C^2_{species}$	$C^3_{species}$	CN	carbide
120	285.97	284.36	283.33			
150	285.97	284.22	283.33			
200	285.80	284.22	283.13	283.53		
300	285.61		283.13	283.53	284.17	
350	285.67		283.13	283.53	284.12	
400	285.67				284.12	284.38
500					284.12	284.38
800					284.12	

Table 1.

Temperature (K)	CH_3NH_2	$N_{species}$	CN
120	399.39		
150	399.45		
200	399.51	397.29	
300	399.56		397.03
350			397.03
400			397.03
500			397.03
800			397.10

Table 2.